University of Alberta

Heat Transfer Analysis of Microwelding Using Tuned Electron Beam

by

Satya Sai Gajapathi

A thesis submitted to the Faculty of Graduate Studies and Research
in partial fulfillment of the requirements for the degree of

Master of Science

Department of Mechanical Engineering

Fall 2011
Edmonton, Alberta

To My Grandma

Abstract

Assembling small scale components is a challenge faced especially by the micro-electronics and medical industry that are dealing with miniaturized components. The current laser and electron beam technologies cannot be used for welding below few hundreds of micrometers because the high heat intensity resulting from reduced beam diameters causes excessive surface ablation. The current research investigates volumetric heating using tuned electron beams as a key to successfully employ high intensity heat sources for welding at micron and possibly nano scales. A numerical model has been developed using state-of-art commercial finite element software to predict the temperature distribution near the moving volumetric heat source for given welding conditions. It is observed that process Peclet number of 100 and beam penetration twice that of the required weld depth are the optimal conditions for carrying out microwelding with least supply of heat input to the substrate and negligible surface ablation.

Acknowledgements

I would first like to thank both my supervisors, Prof. Sushanta K. Mitra and Prof. Patricio F. Mendez for their immense guidance, encouragement, and support during the course of this work. The confidence shown in me by Prof. Mitra and the flexibility provided for independent thinking was exceptional. I am sincerely grateful to Prof. Mendez for being such a huge source of motivation, above everything else. Not many graduate students will have the privilege to be helped by their supervisor until midnight. I consider myself fortunate to have him as my supervisor.

The funding for this work by Natural Sciences and Engineering Research Council of Canada (NSERC) is gratefully acknowledged.

Had it not been the timely suggestions by Prof. Carlos F. Lange, of the Department of Mechanical Engineering, regarding the validation of my numerical model, my thesis would not have looked the same.

I am very grateful to Prof. Gerald A. Knorovksy, of the Sandia National Laboratories, for sharing his insights about microwelding with me during the AWS 2010 meeting. I cannot be thankful enough to Prof. John W. Elmer, of the Lawrence Livermore National Laboratory, for believing in my work and undertaking the huge responsibility to run my experiments at his facility.

I have found the best colleagues in the group members of the Micro and Nano scale Transport Laboratory (MNTL) and Canadian Center for Welding and Joining (CCWJ) especially Prashant Waghmare, Naga Siva Gunda, Kevin Scott, and Stuart Guest. I will always cherish the fun moments shared with them.

When I look back in time, the last two years were the most fast paced in my life. Also, I have educated myself by the greatest amount, both personally and professionally, in these two years. The steep learning vs time curve had not been possible

without the excellent atmosphere created by the combination of many factors such as my wonderful roommate Reeshav Chatterjee, friends at National Institute for Nanotechnology (NINT) especially Dr. Arnab Atta, Lalit Pant, and Debjyoti Sen, faculty in mechanical and materials engineering departments, and the facilities provided to me by the University.

My mother has been the greatest source of inspiration to me all my life. No one else can be as happy as my Mama, when I graduate.

Contents

[1]This chapter is published in the Proceedings of 7th International Conference on Heat Transfer, Fluid Mechanics and Thermodynamics, 2010, Antalya, Turkey

[2]This chapter is accepted for publication as an article in International Journal of Heat and Mass Transfer

[3]This chapter has been submitted for publishing as an article in Science and Technology for Welding and Joining

List of Figures

List of Tables

Chapter 1

Introduction and Literature Review

For the electronics industry to continue obeying Moore's law (which states that the number of transistors that fit into an integrated circuit will double every year until 2020), it is required that the components be successfully integrated at increasingly smaller scales. In addition to the difficulties involved in handling the parts that deludes normal visual perception, the important challenge is to ensure the parts are reliably welded. The current welding technology is not as mature in the micro and nano scales as it is at the macro scale. The dual-problem associated with welding at smaller scales is excessive evaporation due to either high heat intensity requirements (at shorter scan times) or excessive thermal damage of the component/surroundings due to high heat input (at longer scan times). The present research proposes a new welding technology to join materials at micron/submicron scale with minimal heat input and negligible evaporation at reduced manufacturing time. The hypothesis is supported by carrying out heat transfer analysis numerically.

1.1 Background

With the rapid advancement in the micro and nano technology, the scales of the materials to be joined are shrinking down to micro and nano levels. There are many challenges involved in joining such small parts; for example, controlling the amount of heat supplied and carefully focusing at precise positions. High power density beams, which can produce focused spot sizes and provide highly concentrated heating, are considered especially suitable for the purpose of microwelding [1]. The two most popularly used high power density heat sources for microwelding are the laser and the electron beams.

Laser heat source has distinct advantages as compared to the previously used welding heat sources for joining at small scales. Laser beams are capable of precise positioning, realizing small beam diameters (few tens of micrometers), and providing short weld cycle times. Hence, concentrated heating is possible which results in superior weld quality [2]. Because of its clean and non-contact process, laser microwelding technology is used in critical applications of assembling medical implantable devices such as pacemakers and implantable cardiac defibrillator (ICD's) [3]. It is also largely applied for spot welding of thermocouples, hermetic closure of small detonators, electrical interconnects of transistors etc. [2].

Inspite of the wide scale acceptance of laser microwelding technology, its potential for future applications, as the material size to be welded further diminishes, is questionable. The limitations of diffraction set by laser's wavelength and lens aberrations sets a minimum spot diameter beyond which it cannot be focussed [2]. Thus, laser beams cannot be used for welding materials smaller than its minimum beam diameter. The other major setback of using laser beam at reduced beam diameters is its critically high heat intensity levels. Such high heat intensity causes ejection of materials (drilling) as opposed to melting because of the combination of factors such as surface ablation, Marangoni force due to surface tension gradient, and recoil pressure, all due to elevated surface temperatures [4].

Many important properties of welding processes can be inferred from the intensity of their heat source [5, 6]; Fig. 1.1 depicts common welding processes ranked this way. Conventionally, heat sources stronger than 10^{12} W m^{-2} are considered unsuitable for welding; however, welding in this range would be especially beneficial at the micron and submicron scale because of the small area involved and the short residence times. There is a large potential impact in the understanding of this region to overcome its drawbacks. This project studies the feasibility of welding in this regime by using volumetric heat sources instead of the conventional surface heat sources such as lasers, and proposes for the first time a set of criteria that could result in acceptable microwelds.

Of all heat sources used in welding, only electron beams have the property of volumetric heating of metals. This is possible because the interaction volume of electrons under the surface is of the order of microns, ideally suited for microwelding.

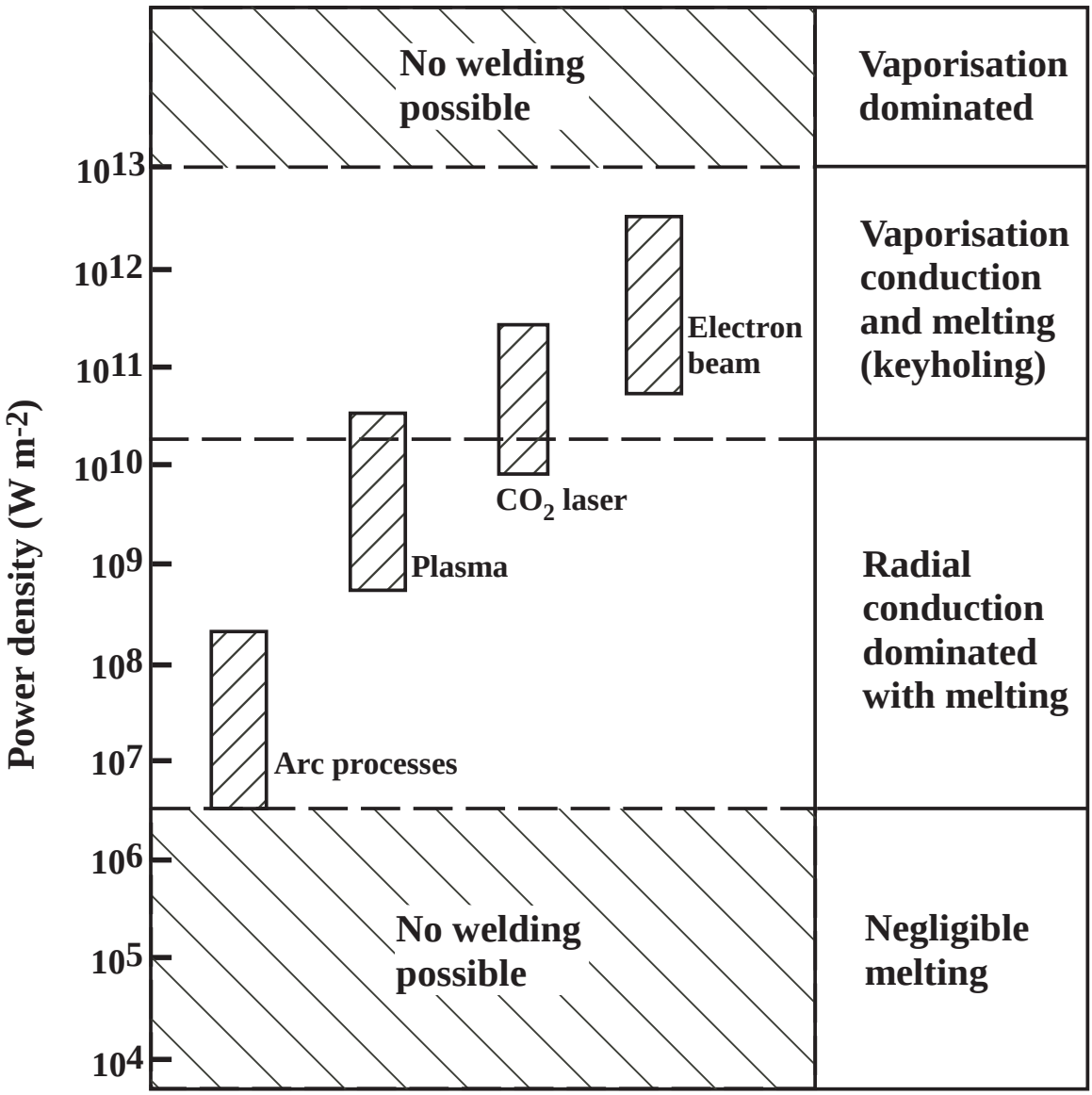

Figure 1.1 – Power density for various welding processes [5]

1.1.1 Advent of Micro Electron Beam Welding Technology

The invention of electron beam is often commented as "a solution looking for a problem". The ability of an electron beam to melt components was accidentally noticed when the thin foils were damaged under a transmission electron microscope [7]. The use of electron beam technology for welding macro scale objects became popular since then. Only recently did the researchers explore the huge potential of electron beams to weld at smaller scales.

Electron beams provide extremely high power density and is able to focus down to nanoscale spot sizes. Accurate dosing of the energy input during electron beam welding (EBW) is possible as there are no mechanical moving components and the beam can be deflected at high speeds using magnetic coils [8]. The electron beam operation takes place in an high vacuum chamber that provides the cleanest environment for welding. In addition to all the above features, the in-situ visual inspection capability during the operation makes the electron beam best suitable to carry out microwelding [2].

The other most important advantage with the electron beams is that they penetrate into the solid and hence behave as volumetric heat source [9, 10]. The rate of surface ablation is expected to significantly decrease for volumetric heat sources as compared to the surface heat sources such as laser beams. The current state of the art in microwelding using both laser and electron beams and their future prospects are summarized in [2, 8, 11].

The electron beam that best suits the purpose of microwelding should have small spot sizes and sufficient power to produce melting depth in the order of microns. The conventional macro electron beam welder has high current ($\sim$ 25mA) and large beam diameter ($\sim$ 1mm), where as, the typical scanning electron microscope (SEM) used for imaging has small current ($\sim$ few nA) and extremely focussed spot size ($\sim$ 1nm) [1]. The equipment necessary for Micro Electron Beam Welding (μEBW) requires a combination of the power of macro-scale electron beam welding and the resolution of a SEM. Such equipment needs to be created for specific projects, typically by modifying a SEM through defocusing the beam and increasing its current [7, 12–20].

A schematic of the equipment typically used for μEBW is shown in Fig. 1.2 and all its important features are identified. The electrons are generated in the hot cathode

(more than 1000 K) due to thermionic emission. The binding potential or the work function of the cathode material has to be over come by providing thermal energy for emission to occur. The large voltage difference between the cathode and the anode accelerates the electrons. The Wehnelt cylinder is used to generate an electric field (slightly negative voltage with respect to the cathode) for focusing the electron beam. The high resolution required for microwelding is provided by the centering coils along with the electromagnetic focussing coils as seen in the same figure. However, decreasing the beam diameter also results in reduced beam current. The beam current can be increased by removing the additional lens aperture typically used in an SEM [9]. The scan and view system provides the live view of the welding as the electron beam scans over the work piece.

The important breakthroughs made in the μEBW still do not elevate the technology for industrial applications. Inspite of some success in specific microwelding experiments in the research laboratories, the technology suffers major setback in terms of repeatability and unpredictability. The coupled behavior of numerous parameters such as beam voltage, scanning speed, material properties, beam current, and beam diameter contributes to the lack of complete understanding of the process and hence encourages further research. The important questions to be asked at the current stage are: Have the microwelding parameters in use been optimized? How to produce welds successfully at high heat flux conditions when the material size further decreases (microwelding experiments have not yet been reported beyond few tens of micrometers)?

1.2 Current Hypothesis

Electron beams can be used to weld at extremely small scale and at high intensity levels by utilizing its volume heating capabilities. In case of volume heating, the incoming energy is absorbed in few microns of material depth instead of irradiating just the top surface (as seen in laser beams). Hence, the top surface is exposed to permissible heat intensity levels in case of electron beam heating even though the beam heat intensity is much higher. As the beam is further focussed while welding at nanoscales, the critical beam heat flux conditions can be attenuated by increasing the beam penetration into the solid.

The proposed electron volume heating of the solid is plausible only when the beam residence time, which is the effective time that the beam spends over a spot

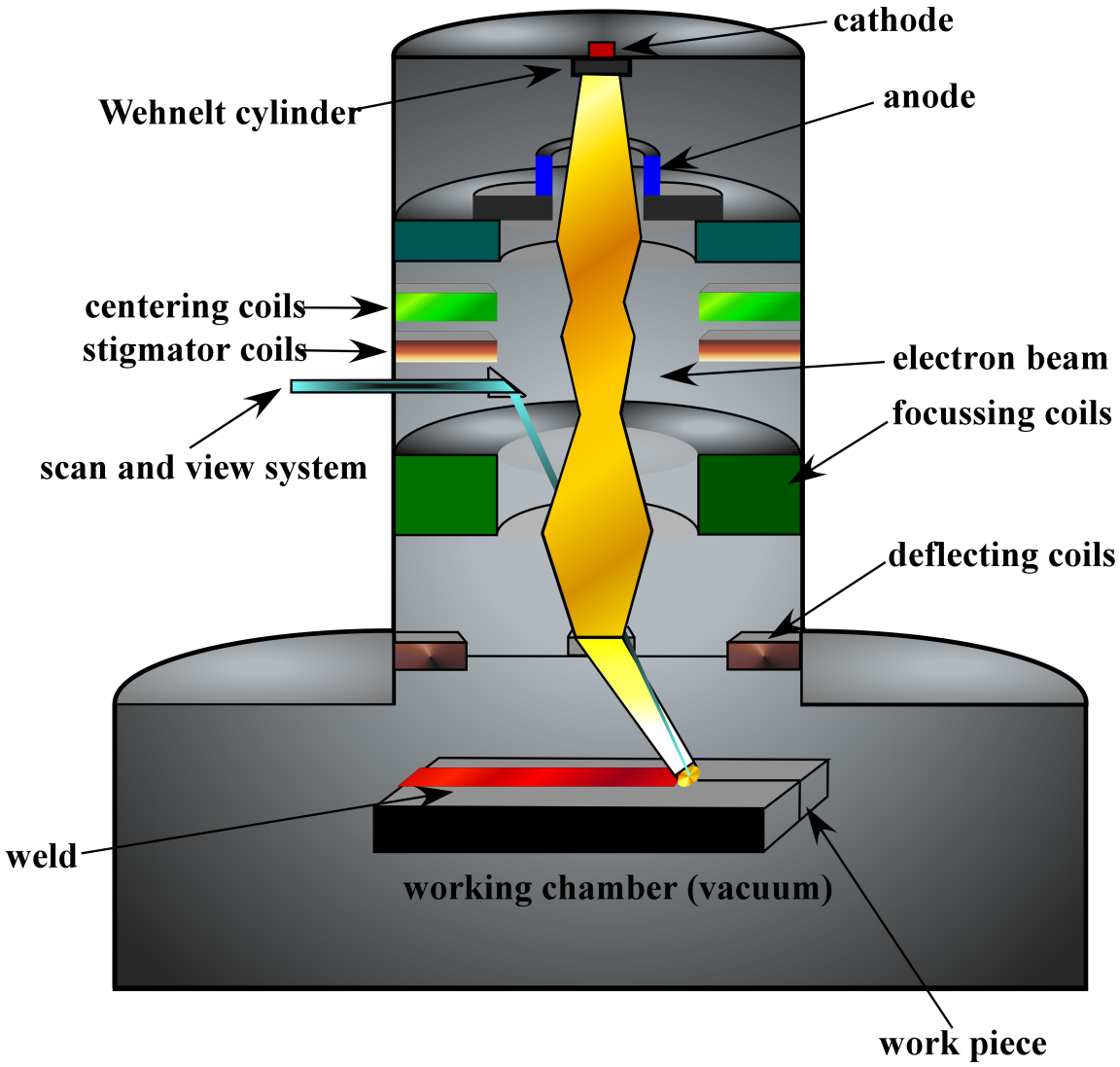

Figure 1.2 – Schematic of a modified SEM used for microwelding

while scanning, is smaller than the thermal diffusion time. At smaller beam residence times, the beam reaches into the desired depth of the material before thermal diffusion can dissipate away the heat. The affected volume in the material is melted rapidly resulting in a minimum amount of heat lost into the surrounding components through diffusion. Also, unnecessary heating of the material beyond the weld region and hence the thermal damage caused to the material is minimized. To obtain such small beam residence times, faster beam traveling speeds while welding has to be selected.

1.3 Objectives

A quantitative description of the current hypothesis requires answering two questions: How to decide the beam penetration depth for a given case? How small should the beam residence time be as compared to the thermal diffusion time?

The parameters that affect the beam penetration and the thermal diffusion time are beam voltage, beam traveling speed, beam diameter, density, specific heat, thermal conductivity, atomic number, and atomic mass of the material. There are two design parameters of the process that accounts for the effect of all the above mentioned parameters on the process, namely, Peclet number, which is the measure of the amount of heat diffusion occurring during the process, and the relative beam penetration depth, which is the depth of beam penetration with respect to the weld depth. The major objectives of the current project were as follows:

1. To find the optimized Peclet number which is indicative of the thermal diffusion time
2. To find the optimum beam penetration depth required for producing a given weld depth

Heat transfer analysis of the μEBW has been carried out numerically using finite element based COMSOL Multiphysics^{TM} to determine the optimal parameters. The feasibility of the process is evaluated based on the requirements of lower surface temperature, lower heat input, and high controllability. The phase transformations such as melting and evaporation are incorporated and realistic boundary conditions are used so that the numerical models closely represents the practical situation. Proof-of-concept experiments are proposed guided by the numerical model of μEBW.

1.4 Thesis Outline

The remaining five chapters of this thesis are directed by the following outline:

Chapter 2 deals with developing a mathematical model of μEBW and solving it analytically for the asymptotic case of no conduction. The asymptotic model provides direct relationships between the input and output weld parameters and allows to predict the maximum possible values of temperature, weld depth, and weld width of the process beforehand.

Chapter 3 explains the development of a numerical model of μEBW to predict the three dimensional temperature distribution in the solid near the heat source. The

electron beam is represented here as a simplistic exponential decay heat source. The asymptotic solution developed in Chapter 2 helps to validate the numerical model.

Chapter 4 describes the formulation of a three dimensional distributed heat source model that closely represents electron beam heating in the solid. The new heat source model is implemented in the numerical model of μEBW developed in Chapter 3 and the optimal criteria of microwelding are determined.

Chapter 5 illustrates the incorporation of phase transformation phenomena such as melting and evaporation into the numerical model of μEBW. The numerical model is then used to suggest conditions for proof-of-concept experiments.

Chapter 6 summarizes the important conclusions from this project and lays down the considerations for future work.

Chapter 2

Analytical Method To Study The Temperature Distribution Of a Moving Heat Source Electron Beam Microwelding[1]

Recently, the use of electron beam for micro-welding has become one of the primary research areas. Electron beam can behave as a volumetric heat source and is capable of traveling very fast and focusing at very small spot sizes. This proves ideal for welding at small scales as thermal stresses and losses due to ablation are controlled in the material. The choice of beam parameters remains a challenge as it depends on many factors like characteristics of the material and nature of application. An understanding of the beam-substrate interactions and hence the temperature distribution in the material due to this, can lead to wide spread applications of this technique. An analytical method based on the theory of heat transfer is proposed in the present work to yield the temperature distributions in the material during electron beam micro-welding. Plots identifying the maximum temperature and region of melting, obtained as results of the study, can help to optimize beam parameters for a process. The material properties of stainless steel are used to plot the temperature distribution in the material during micro-welding. The formulation is also extended to make use of electron beam for nano-welding, extrapolating the macro-level properties. For the case of nano-welding, the weld characteristics like the maximum temperature, weld depth and width are obtained for the specified values of the beam parameters, using the material properties of silicon.

[1]This chapter is published in the Proceedings of 7th International Conference on Heat Transfer, Fluid Mechanics and Thermodynamics, 2010, Antalya, Turkey

2.1 Introduction

The ever-decreasing size of the electronic components, eg. microchips, pose a growing requirement of miniaturized features with high edge acuity and negligible thermal damage zone. Micro-welding is a key fabrication process utilized in the manufacture of miniature devices, including implantable medical devices and MEMS. Welding at micro-scale brings in new challenges in the form of surface ablation, capillary effects, etc. Also, the characteristics of the welds produced are very sensitive to the nature of application. The joining points have frequently a functional task, e.g., electrical conductivity or the sealing of the component. Hence, welding at micro-scales is restricted to the use of highly localized heat sources. Laser beams and electron beams, owing to their capability of focussing at small spot sizes and hence very high power density, are suitable for such purposes. While laser welding at micro scale is largely being used in industries, the use of electron beam technology is still in the laboratory stage.

The properties like realization of small spot size, inertia free manipulation, concentrated volumetric energy input and applicability to metals, insulators and semiconductors makes the use of electron beam welding technique very promising for micro systems compared to use of laser beam. However, electron beam welding machines from the macro range cannot be used in the micro scales because of their large beam spots and lack of motion control. With the growing necessity of microprocessing technology, scanning electron microscope (SEM), which otherwise is used for surface measurement or characterization, is modified to produce a high-density localized electron beam suitable for microjoining [7, 19]. Smolka *et al.* [18] studied the characteristics of the SEM as micro-welding machine. Knorovsky *et al.* [10] evaluated the effects of various factors related to heat transfer and energy absorption on the parameter selection of a SEM for micro-welding operations. A review of difficulties and prospects in using a SEM for micro-welding for various kinds of materials are reported by Reisgen *et al.* [20]. The parameters of electron beam for micro-welding of steel wires are reported experimentally by Reisgen *et al.* [16].

Other than the difficulties in controlling SEM parameters, the success of the electron beam technology in microwelding is limited because of a lack of thorough understanding of the heat transfer taking place at this scale. The challenge is to model the rapidly scanning electron beam as a heat source. Monte Carlo simulations have been carried out to characterize the electron beam as volumetric heat source [10, 21]. The

size of the beam interaction volume is studied to be a function of accelerating voltage and the material properties like atomic weight and atomic number [22, 23]. Hwang *et al.* [12] developed a semi-empirical method to model the heat source. Basing on this, bead-on-plate experiments for a stainless steel are carried out for different combinations of beam parameters such as beam current and beam velocity.

An efficient way to predict the beam parameters for a micro-welding operation would be to carry out heat transfer analysis and optimize the variables by studying the temperature distributions, which hasn't been carried out at these scales to the best of author's knowledge. In the present study, an analytical method is proposed to study the temperature distributions in the material due to the energy transfer from the beam. The model considers electron beam as moving volumetric heat source. The parameters of the beam are required to be fixed in such a way that only a small region is melted around the heat source and negligible amount of evaporation is taking place. The beam parameters like voltage input, probe current, beam diameter, and beam velocity are required to predict the temperature distribution in the material. Beam voltage is fixed based on the depth of the weld required [22, 23]. The beam diameter is fixed according to the scale of welding required. Heat input (power/velocity) is selected in such a way that the required temperature distribution is obtained with less thermal stress zone. Present study is based on the general energy conservation principle that applies to all materials at all scales. The heat source model proposed by Brown *et al.* [24] is used to represent the electron beam.

2.2 Analysis

Electron beam is studied as heat source which generates heat in a concentrated volume near the surface. This causes an increase in enthalpy in the regions near the hot spots. The Fourier heat conduction equation including the source term is required to be solved in the material to obtain temperature distribution.

$$k\left(\frac{\partial^2 T}{\partial^2 x}+\frac{\partial^2 T}{\partial^2 y}+\frac{\partial^2 T}{\partial^2 z}\right)+q=\rho c_p\frac{dT}{dt} \tag{2.1}$$

where, k, ρ, c_p are the thermal conductivity, density and specific heat capacity of the material and the heat source term q represents the electron beam volumetric heat source.

For welding at micro scales, the heat source needs to move very fast over the surface. This is to avoid concentration of heat at any single point, which otherwise can

increase thermal stress in the material or increased loss of volume due to evaporation. The Peclet number (Pe), that is a measure of the amount of heat diffusion occurring during a process, is high for such fast moving heat sources where heat diffusion is minimal. Thus, heat dissipation due to conduction can be neglected for high Pe, taking into account the small time scales [24]. Hence, the Fourier heat conduction equation is reduced to heating rate equation, as:

$$q = \rho c_p \frac{dT}{dt} \tag{2.2}$$

Equation (2.2) is solved over a semi-infinite solid. A 3-D block around the heat source at a given point of time is represented in Fig. 1. The region of sharp temperature gradients is however restricted to a small region around the heat source, depending on the heat input and beam diameter. Heat loss due to radiation and evaporation from the top boundary is purposefully neglected in this study so that a distribution of maximum temperature at any point is obtained. It is the knowledge of maximum temperature which is predominant while selecting the beam parameters as it helps to control the process.

The variables are non-dimensionalized as follows:

$$x^* = \frac{x}{x_e} \tag{2.3}$$

The characteristic length x_e along the depth is defined as the effective electron penetration depth and the formula to obtain it is provided by Brown *et al.*[24], for a given accelerating voltage and properties of the material. The coordinates along the beam motion and perpendicular to it can be normalized by characteristic length scales w and l which will be defined later.

$$y^* = \frac{y}{w} \qquad z^* = \frac{z}{l} \tag{2.4}$$

In the stationary coordinate frame as the source is moving along $z-$direction, it position can be defined as a function of time as:

$$z = vt \tag{2.5}$$

By using Eq. (2.4), the time can be written as:

$$t = \frac{l}{v} z^* \tag{2.6}$$

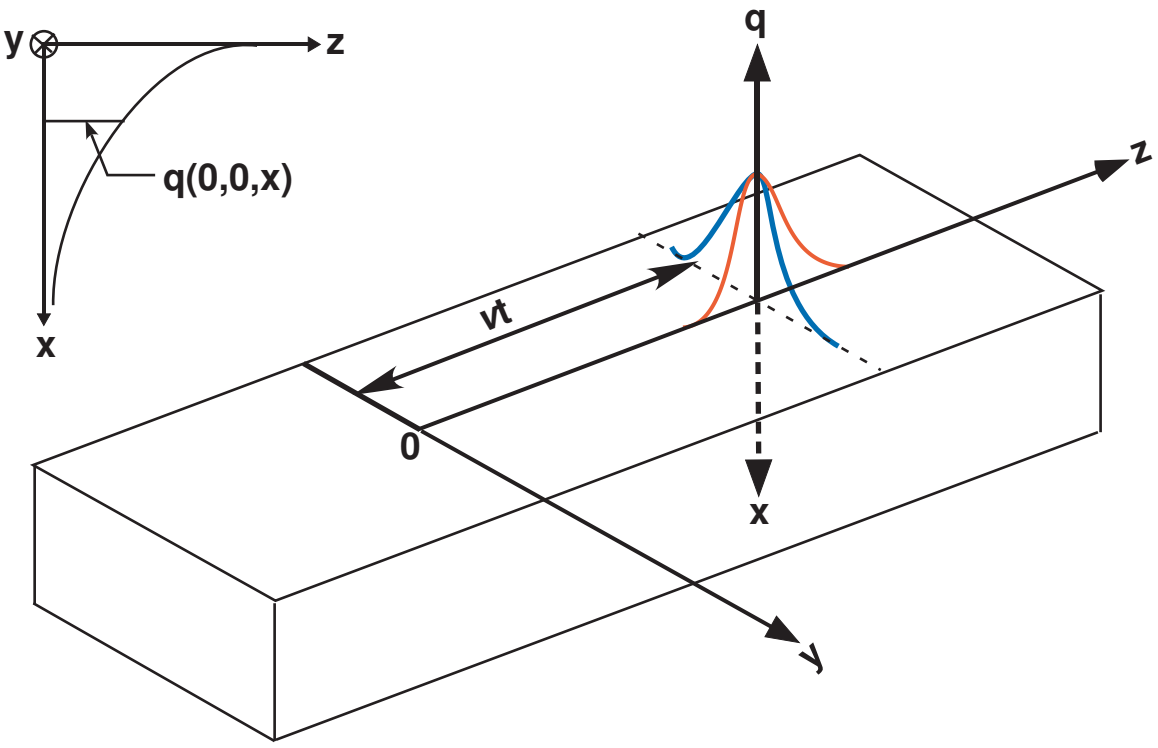

Figure 2.1 – Model of a semi-infinite solid showing the moving heat source and the coordinate axes ($0 < x < \infty, -\infty < y < \infty, -\infty < z < \infty$)

The normalized time variable is defined as, $t^* = z^*$,

$$t = \frac{l}{v} t^* \tag{2.7}$$

The temperature and the heat source term used in the heating rate equation can be written in the normalized form as:

$$T(x, y, z) = T_0 + \Delta T_{max} T^*(x^*, y^*, z^*(t^*)) \tag{2.8}$$

$$q(x, y, z(t)) = q_{max} q^*(x^*, y^*, z^*(t^*)) \tag{2.9}$$

where, T_{max} is the asymptotic maximum temperature of the process and q_{max} is the normalizing variable and represents the maximum value of power absorbed in the material.

Now, non-dimensional form of Eq. (2.2) can be written as:

$$\rho c_p \frac{\Delta T_{max}}{l/v} \frac{dT^*}{dz^*} = q_{max} q^* \tag{2.10}$$

In an electron beam welding process, the power of the beam is converted in to thermal energy as the electrons collide with the material. The energy conservation principle

provides the relationship between the volumetric heat input and the power of the beam.

$$\int_{\infty}^{-\infty}\int_{\infty}^{-\infty}\int_{\infty}^{0} qdxdydz = VI = W \tag{2.11}$$

where, V and I are the beam voltage and current, and W represents the total beam power. Equation (2.11) can also be written in normalized form as follows:

$$q_{max}x_e wl\int_{\infty}^{-\infty}\int_{\infty}^{-\infty}\int_{\infty}^{0} q^*dx^*dy^*dz^* = W \tag{2.12}$$

All the power of the beam is not converted into heat. There is loss of power during this process due to back scattered electrons, x-rays, etc. Usually there is an efficiency factor involved to calculate the actual power from the theoretical power input. The efficiency factor is considered unity in the present study.

2.3 Heat Source Modeling

The shape of the volumetric heat source is assumed to be a round Gaussian distribution with an exponential decay penetration, as proposed by Brown *et al.* [24].

$$q(x,y,z) = q_{max}e^{\left(-\frac{y^2+z^2}{2\sigma^2}\right)}e^{\left(-\frac{x}{x_e}\right)} \tag{2.13}$$

where, σ is the standard deviation of the beam function. It is related to the full width half maximum (FWHM) of the beam by the relation FWHM=2.335σ. The FWHM is considered as the electron beam diameter in the present study. In Eq. 2.4, considering l and w equal to the standard deviation of the Gaussian function and using Eq. 2.3, Eq. (2.13) can be written in the non-dimensional form as:

$$q^*(x^*,y^*,z^*) = e^{\left(-\frac{y^{*2}+z^{*2}}{2}\right)}e^{-x^*} \tag{2.14}$$

2.4 Solution

The heat source term can now be integrated all over the domain to find the maximum volumetric heat input using Eq. (2.12) as:

$$q_{max}x_e wl\int_{\infty}^{-\infty}\int_{\infty}^{-\infty}\int_{\infty}^{0} e^{\left(-\frac{y^{*2}+z^{*2}}{2}\right)}e^{-x^*}dx^*dy^*dz^* = W \tag{2.15}$$

where,

$$\int_{\infty}^{-\infty}\int_{\infty}^{-\infty}\int_{\infty}^{0} e^{\left(-\frac{y^{*2}+z^{*2}}{2}\right)}e^{-x^*}dx^*dy^*dz^* = 2\pi \tag{2.16}$$

Using Eqs. (2.15) and (2.16), the maximum value of the beam power absorbed can be determined as follows:

$$q_{max} = \frac{W}{2\pi x_e \sigma^2} \tag{2.17}$$

The maximum temperature is expected to be obtained on the surface and along the path of the heat source ($x = 0$ and $y = 0$). This can be calculated by substituting Eq. (2.14) in Eq. (2.10) and by integrating over the entire time range, as:

$$\rho c_p \Delta T_{max} \frac{v}{\sigma} \int_1^0 dT^* = q_{max} \int_\infty^{-\infty} e^{\left(-\frac{z^{*2}}{2}\right)} dz^* \tag{2.18}$$

On solving,

$$\rho c_p \Delta T_{max} \frac{v}{\sigma} = \sqrt{2\pi} q_{max} \tag{2.19}$$

Substituting Eq. (2.17) in Eq. (2.18), the expression for maximum temperature attained during microwelding is obtained as shown below:

$$T_{max} - T_0 = \frac{W}{\sqrt{2\pi} v x_e \sigma} \tag{2.20}$$

2.4.1 Calculation of Final Temperature Distribution Along y-direction on x=0 Plane

Using Eqs. (2.14) and (2.10) to integrate over the entire time range, the final temperature distribution due to the power input in the $x = 0$ plane is obtained as:

$$\rho c_p \Delta T_{max} \frac{v}{\sigma} \int_{T^*}^0 dT^* = q_{max} e^{\left(-\frac{y^{*2}}{2}\right)} \int_\infty^{-\infty} e^{\left(-\frac{z^{*2}}{2}\right)} dt^* \tag{2.21}$$

On solving Eqs. (2.8) and (2.19), the temperature variation along the normal direction to the beam is obtained as:

$$T = T_0 + \Delta T_{max} e^{\left(-\frac{y^{*2}}{2}\right)} \tag{2.22}$$

The heat flux (q_s) distribution along y-axis on the x=0 plane is calculated by substituting $x = 0$ in Eq. (2.13) and integrating along the $z-$axis, as:

$$q_s = q_{max} e^{\left(-\frac{y^2}{2\sigma^2}\right)} \int_\infty^{-\infty} e^{\left(-\frac{z^2}{2\sigma^2}\right)} dz \tag{2.23}$$

On solving, the heat flux distribution can be obtained as:

$$q_s = \sqrt{2\pi}\sigma q_{max} e^{\left(-\frac{y^2}{2\sigma^2}\right)} \tag{2.24}$$

2.4.2 Calculation of Melting Isotherm in $x-y$ Plane

The weld depth (x_m) and weld width ($2y_m$) of the weld are approximated by calculating the region in the $x-y$ plane bounded by the melting temperature isotherm. The temperature has been fixed as the melting point of the material and the locus of points having melting temperature is calculated by integrating Eq. (2.10) over the entire range of time, as:

$$\rho c_p \Delta T_{max} \frac{v}{\sigma} \int_{T_m{}^*}^{0} dT^* = q_{max} e^{\left(-\frac{{y_m}^{*2}}{2}\right)} e^{-x_m{}^*} \int_{\infty}^{-\infty} e^{\left(-\frac{t^{*2}}{2}\right)} dt^* \tag{2.25}$$

In Eq. (2.25), x_m and y_m are the melting depth and melting width for any given point along the path of the moving heat source. They are calculated based on the final temperature attained as the source moves all along the semi-infinite solid. Also, z^* has been substituted as t^* in Eq. (2.25) as they are analogous.

On solving, the x_m and y_m as a function of temperature can be obtained as:

$$\frac{x_m}{x_e} + \frac{{y_m}^2}{2\sigma^2} = \ln \frac{\Delta T_{max}}{\Delta T_m} \tag{2.26}$$

2.4.3 Calculation of Melting Isotherm in $y-z$ Plane

Melting isotherms can also be found in the $y-z$ plane by substituting x^* =0, $y^* = {y_m}^*$ and $z^* = z_m*$ in Eq. (2.25) and integrating over the entire range of z^*, as:

$$\rho c_p \Delta T_{max} \frac{v}{\sigma} \int_{T_m{}^*}^{0} dT^* = q_{max} e^{\left(-\frac{{y_m}^{*2}}{2}\right)} \int_{z_m{}^*}^{-\infty} e^{\left(-\frac{{z_m}^{*2}}{2}\right)} dz^* \tag{2.27}$$

Solving using Eqs. (2.8) and 2.19,

$$\frac{\sqrt{2\pi}\Delta T_m}{\Delta T_{max}} = e^{\left(-\frac{{y_m}^2}{2\sigma^2}\right)} \int_{z_m{}^*}^{-\infty} e^{\left(-\frac{{z_m}^{*2}}{2}\right)} dz^* \tag{2.28}$$

The value of ΔT_{max} can be found using Eq. (2.20). Equation (2.28) can be used to plot the melting isotherm in the $y-z$ plane.

2.4.4 Calculation of Temperature Distribution Along $z-$direction

The temperature variation at a point on the path of the moving heat source can be calculated as the heat source moves over it. This is analogous to calculating the temperature along $z-$axis at fixed point of time. On $z-$axis, Eq. (2.18) can be written as:

$$\rho c_p \Delta T_{max} \frac{v}{\sigma} \int_{{T_{max}}^*}^{0} dT^* = q_{max} \int_{t^*}^{-\infty} e^{\left(-\frac{t^{*2}}{2}\right)} dt^* \tag{2.29}$$

For final temperature along $z-$axis, Eq. (2.29) can be solved by substituting Eqs. (2.8) and (2.19):

$$T = T_0 + \frac{\Delta T_{max}}{\sqrt{2\pi}} \int_{t^*}^{-\infty} e^{\left(-\frac{t^{*2}}{2}\right)} dt^* \tag{2.30}$$

The heat flux as a function of time (q_t) can be calculated over a point on the path of the heat source ($z-$axis) by substituted $x = 0$ and integrating all over the $y-$axis in Eq. (2.13) as:

$$q_t = \sqrt{2\pi} q_{max} e^{\left(-\frac{(vt)^2}{2\sigma^2}\right)} \tag{2.31}$$

2.5 Results and Discussion

The analytical expression obtained for temperature and heat flux depends on the properties of the material used and beam parameters. Also, selection of beam parameters for welding depends on the material properties. The density of the material decides the electron penetration depth based on the accelerating voltage. The properties of the stainless steel and silicon, relevant to the welding operation using electron beam, are shown in Table 2.1.

Table 2.1 – Properties of stainless steel and silicon used in the calculations

Properties	Steel (microwelding)	Silicon (nanowelding)
Thermal conductivity (k)	33	163
Density (ρ)	7912	2330
Specific heat capacity (c_p)	468	703
Melting temperature (T_m)	1400	1414
Initial temperature (T_0)	25	25
Atomic mass (A)	56	28
Atomic number (Z)	26	14

The four pre-dominant characteristics of an electron beam used in welding at small scales, namely, accelerating voltage, probe current, beam diameter, and beam velocity are specified in Table 2.2. The beam voltage depends on the amount of penetration required i.e., the weld depth. Generally, a penetration depth of the same order of beam diameter or smaller is preferred. The beam diameter is selected according to the scale of the material to be joined. The maximum temperature has been approximated for several cases of heat input (power/velocity) and the results are illustrated for the most optimized set of beam parameters. It has to be observed that the maximum temperature obtained for a set of beam parameters shouldn't exceed the melting

temperature by a large limit.

Table 2.2 – Beam parameters used

Beam parameters	Steel (microwelding)	Silicon (nanowelding)
V	50 kV	3 kV
I	200 μA	10 nA
FWHM	12 μm	100 nm
v	25 m s^{-1}	0.7 m s^{-1}

Beam power is the product of the accelerating voltage and the probe current. The formulae provided by Brown*et al.* [24] is used to calculate the effective electron penetration depth (x_e) using the accelerating voltage, atomic number and mass of the material. The effective penetration depth should be of the order of the maximum melting depth in the material as it is heated purely by electrons (and not heat diffusion). Table 2.3 presents the intermediate parameters calculated to estimate the final temperature distribution.

Table 2.3 – Intermediate parameters

	Steel (microwelding)	Silicon (nanowelding)
W	10 W	30 μW
x_e	2.99 μm	86.4 nm
α	8.9×10^{-6} m^2 s^{-1}	9.95×10^{-5} m^2 s^{-1}

In Fig. 2.2, temperature variation along $y-$axis (perpendicular to the direction of heat source motion) is plotted for any given point on the $z-$axis (on the path of the heat source) using Eq. (2.22). Heat flux distribution along the same line is found out using Eq. (2.24) and shown in the plot. The temperature and the heat flux have their peaks at $y = 0$ i.e, along the centreline of the surface. The temperature gradients become negligible for lengths of about 20 μm away from the center line along $y-$axis.

Figure 2.3 shows the melting temperature isotherm, using Eq. (2.26). The region of melting as the heat source over a point is shown. The position of the beam is represented by plotting the heat flux distribution along $y-$axis using Eq. (2.24). The maximum depth of melting (x_m) is obtained right under the beam. The points of

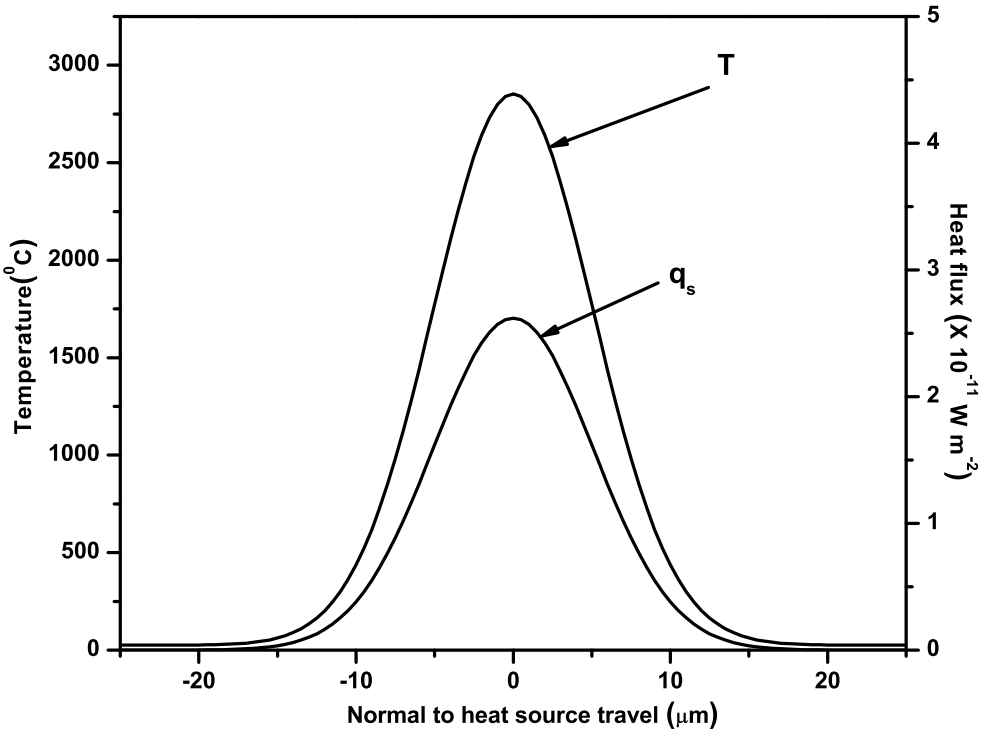

Figure 2.2 – Variation of temperature and heat flux along y-axis for any given point on the z-axis on the steel surface

intersection of the melting temperature isotherm on $y-$axis represent the maximum width of the weld.

Figure 2.4 shows the melting temperature isotherm as seen on the top surface ($y-z$ plane) using Eq. (2.28). The heat source is located at the origin. Sharp gradient in the slope of the melting isotherm near the origin is due to the high velocity of the heat source. Away from the origin, the curves rise normal to the horizontal axis. The intercept represents the weld width. The melting isotherm extends a small length scale below the origin. This represents the melting region ahead of the heat source. The outer circle represents the spot size and the position of the beam. The diameter of the circle is the FWHM value of the Gaussian function chosen to represent the electron beam.

$$y^2 + z^2 = \left(\frac{d^2}{4}\right) \tag{2.32}$$

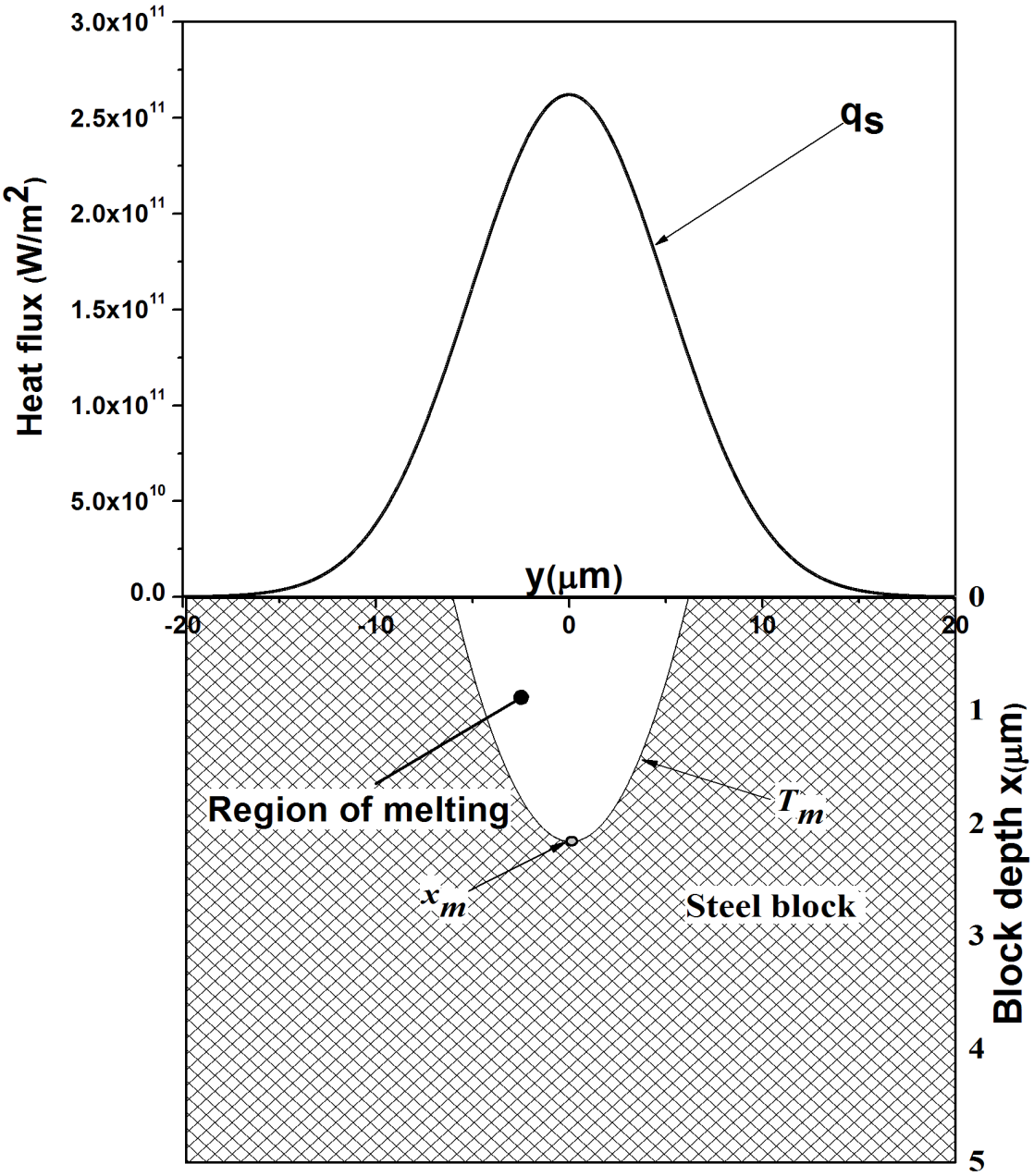

Figure 2.3 – Isotherm of melting temperature in the $x-y$ plane. Heat flux distribution along y-axis is also shown

Figure 2.5 shows the variation of temperature with time over any given point along the path of the heat source. The temperature of the point begins to increase as the heat source arrives at a closer proximity. Time zero signifies that the beam is over head of the chosen point. It is noticed that the melting temperature (1400

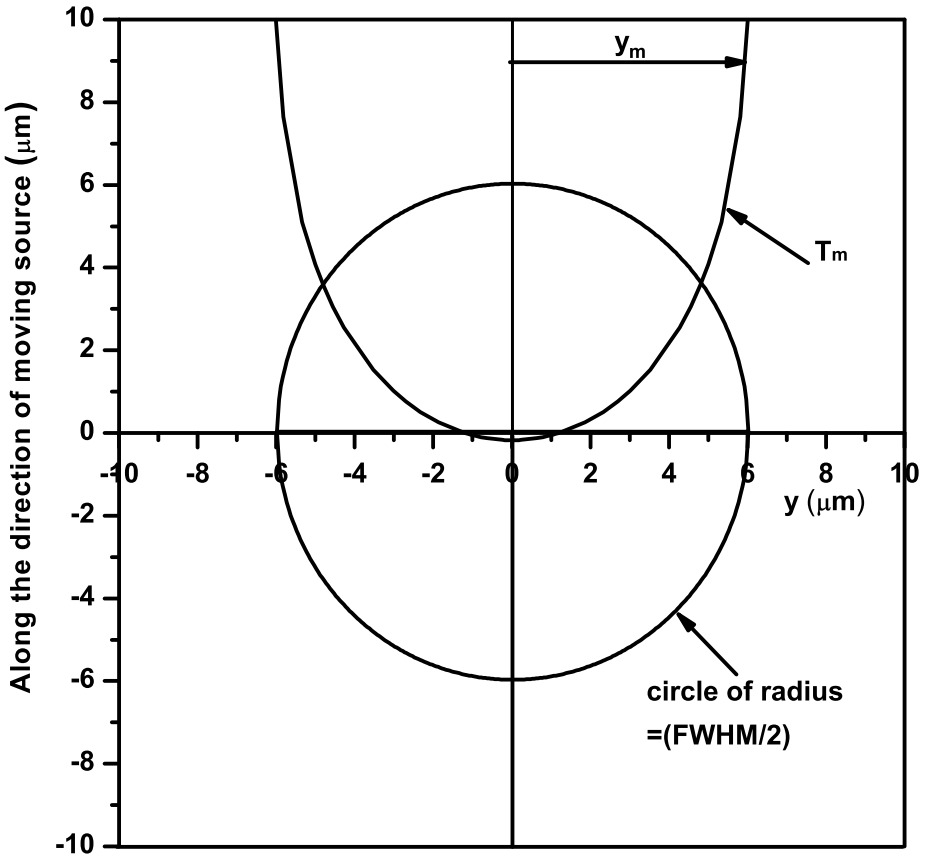

Figure 2.4 – Isotherm of melting temperature in the $y-z$ plane of the steel surface

^{0}C) is attained before the heat source arrives on the point. This small time advance corresponds to the melting length below origin in Fig. 2.4. Also, it is found that the maximum temperature at the point is attained after the heat source has moved a small distance beyond it.

The maximum temperature obtained during the micro-welding process for the specified set of beam parameters is 2853 ^{0}C as suggested by the peak value of temperature plot in Figs. 2.2 and 2.3. The farthest point of melting temperature along $x-$axis and $y-$axis in Fig. 2.3 represents the weld depth and weld width, respectively.

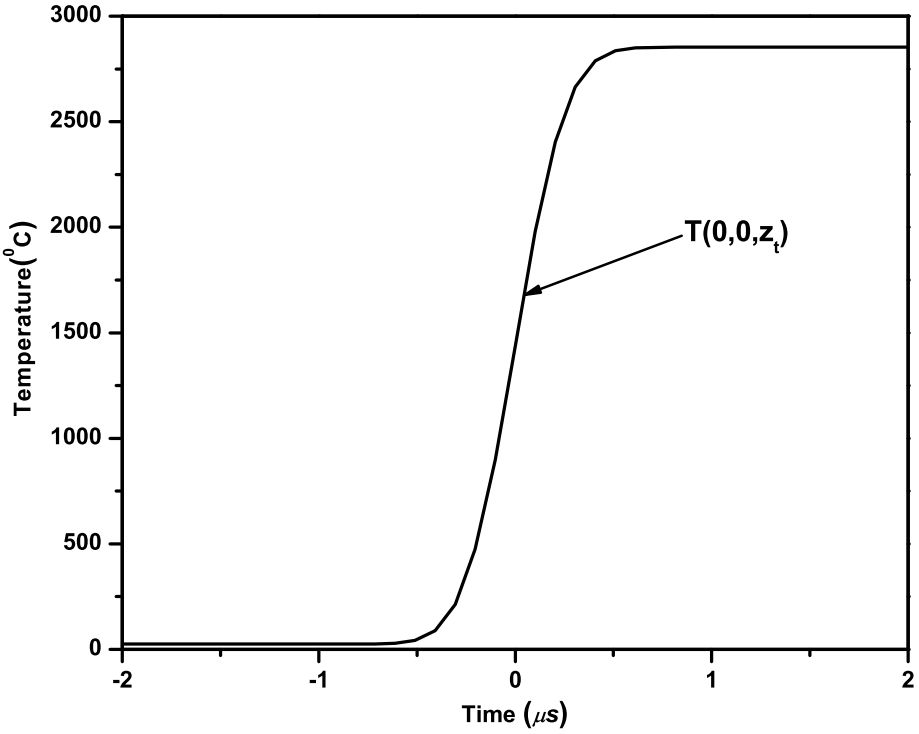

Figure 2.5 – Variation of temperature at a point on the steel surface along the path of the moving heat source

The weld width can also be compared by measuring the distance along $y-$axis of the melting isotherm in Fig. 2.4 far away from the origin. The values of these parameters as obtained from the plots are shown in Table 2.4 for micro-welding of steel.

This technique can further be extended to weld materials whose characteristic dimensions are in nanometers (nm). The weld characteristics of nanowelding for silicon are obtained from Eqs. (2.20) and (2.26) and the corresponding parameters are provided in Table 2.4.

2.6 Conclusion

Electron beam has been studied as volumetric heat source that can be used efficiently for welding at lower scales. A mathematical model has been developed to find the temperature distributions during welding operation using such a beam. A detailed

Table 2.4 – Weld characteristics

	Steel (microwelding)	Silicon (nanowelding)
T_{max}	2853 ^{0}C	2891 ^{0}C
x_m	2.16 μm	62 nm
y_m	6.2 μm	50.9 nm

procedure has been outlined to interpret the results, in the form of maximum temperature on the surface and melting region, which guides the selection of beam parameters.

Use of high powered electron beam source moving on the surface of the substrate at very high velocity is identified as the most efficient way to achieve welding at low scales. It is also observed that for very short scales of distance and time, the temperature away from the heat source reaches the steady state. The possibility of using such a beam for nano-welding is also demonstrated.

Chapter 3

Controlling Heat Transfer in Micro Electron Beam Welding Using Volumetric Heating[1]

The small spot sizes and short residence times involved in microwelding ideally demands the use of extremely high power density heat sources, which is beyond the feasible range in welding. The present work explores the use of volumetric heating as a key to enable microwelding at such enhanced heat intensity levels. In this work, the electron beam is represented as a volumetric heat source and a numerical model is developed to obtain the temperature field for a moving heat source. The model has been validated against analytical solutions for various asymptotic cases. The asymptotic cases include the heat distribution by conduction at distances far away from the beam and the temperature field due to negligible conduction under the beam. The effect of weld speed and beam interaction volume are evaluated to propose the optimum conditions of microwelding. Optimality is based on limited heat flow into the material, high controllability, and tolerable maximum temperature of the process. For the choice of AISI 304 material as an example, the optimum welding conditions required to produce a 2.5 μm weld depth are determined in the non-dimensional form of Peclet number 100 and relative beam penetration in the range of 0.8-1.2.

3.1 Introduction

The use of electron beam technology for microwelding came into existence less than a decade ago and has received much attention since then. Micro Electron Beam Welding (μEBW) experiments were first reported by Smolka *et al.* [18] in 2004. Many success-

[1]This chapter is accepted for publication as an article in International Journal of Heat and Mass Transfer

Table 3.1 – Parameters of μEBW experiments presented in the literature. The values with * symbol were not reported explicitly, for which an estimated value has been used. The Pe is defined here as, Pe=$\frac{Ud}{\alpha}$

	Beam Parameters				Maximum **Pe**	Maximum z_e/z_m
	V	I	d	U		
Hwang *et al.*[12]	30 kV	10 μA	20 μm*	10-20 μm s^{-1}	**∼0.0001**	**∼0.1**
Knorovsky *et al.*[7]	30 kV	25 μA	0.2 μm	2.3 m s^{-1}	**∼0.02**	**∼0.04**
Baertle *et al.*[13]	30-50 kV	10 mA	40-60 μm	10 mm s^{-1}*	**∼0.15**	**-**
Bohm *et al.*[14]	50 kV	1-2 mA	50 μm	1-100 mm s^{-1}	**∼1.26**	**∼0.03**
Tanasie *et al.*[15]	50 kV	2 mA	150 μm	10 mm s^{-1}	**∼0.4**	**∼0.06**
Reisgen *et al.*[16]	30 kV	100 μA	12-20 μm	25-110 μm s^{-1}	**∼0.0006**	**∼0.04**
Ogawa *et al.*[17]	30 kV	0.1-150 μA	20 μm*	6-1500 μm s^{-1}	**∼0.008**	**∼0.06**
Present work	50 kV	310 μA	10 μm	39.5 m s^{-1}	**100**	**0.8-1.2**

ful experiments have been carried out so far and can be found in [7, 12–17, 19, 20]. The deciding welding parameters (acceleration voltage (V), probe/beam current (I), beam diameter (d), and weld speed (U)) used in the above cited experiments can be found in Table 3.1. The knowledge of the material properties and the dimensions of the microweld can help to deduce important inferences about the suitability of the processes. A crucial indicator of the applicability of μEBW is the Peclet number (Pe), which is a measure of the relative amount of heat diffusion during the process. A high Pe process implies small beam residence times or minimal heat diffusion into the body and hence causing less thermal damage to it. The other significant indicator of heat control in μEBW is the amount of electron penetration (z_e) with respect to the melting depth (z_m). The Pe and z_e/z_m for different μEBW experiments reported in the literature are listed in Table 3.1 along with the optimized parameters obtained using the numerical model in the current study, shown as the highlighted row in the same table. Huge differences between the values of Pe and relative beam penetration used in the reported experiments and their corresponding optimized values indicate that neither the high power density characteristics of the beam nor its volume heating capability is put to best use; hence, the current use of μEBW technology is far from its true potential.

The purpose of this chapter is to explore the paradigm of volumetric heating to enable welding in a regime conventionally thought impossible. The model developed to explore this concept aims to be a minimal representation of the essential physical processes, and involves some mathematical simplifications. Acknowledging the complexity of the real welding process, this model is a first step towards the development

of a new technology, and the conclusions derived from this analysis are not expected to change qualitatively with future comprehensive simulations and experiments. The temperature profiles as a result of welding is simulated in the present work by solving the heat conduction equation in a semi-infinite domain; where, the mathematical model of volumetric heat source as proposed by Brown *et al.* [24] and Sanders and Mendez [25] is substituted for the heat generation term. The numerical solution has been validated for two asymptotic cases of temperature distribution in the far field and under the beam following the guidelines in [26, 27]. Furthermore, the effects of Pe and beam penetration is investigated to suggest the most suitable conditions for a required size of the weld.

3.2 Mathematical Model

3.2.1 Description of the process

Electrons are generated and tuned in the beam column such that they are adequately focussed and have the required power to weld in micro scale. A tungsten filament is charged to emit the electrons in a vacuum through thermionic emission. The acceleration voltage increases the kinetic energy of the electrons before they strike the material surface; the amount of penetration of the electrons into the body is also dependent on the acceleration voltage of the beam. The high velocity electrons generates heat in the material as a result of the inelastic collisions in the lattice [2]. As a result, the region affected by the beam is melted. When the beam moves along the weld line, the molten pool eventually solidifies to form a weld. Modeling such a process to obtain the temperature field in the material requires representing the electron beam volumetric heat generation and dealing with the moving heat source.

3.2.2 Development of the heat source model

The theory of moving heat sources is widely reviewed since it was first developed by Rosenthal [28], who considered only one dimensional heat sources. Later, Eagar and Tsai [29] developed the two-dimensional Gaussian distributed heat source model which closely represents different practical welding heat sources. The analytical solution for two dimensional moving heat sources and its application in modeling various welding processes can be found in [30–32]. The two dimensional heat source model did not account for the heat penetration effect, characteristic of many welding processes, thus, leading to the development of three dimensional double ellipsoidal heat source

model by Goldak *et al.* [33]. However, this three dimensional heat source model is semi-empirical and it becomes impractical to apply such a model in μEBW study. Also, the heat source models of lasers considering exponential decay penetration into the medium [34, 35] is unlike the electron beam where penetration depends on the acceleration voltage and material properties. The best predictions of the electron energy distribution as they penetrate inside the material is provided by Monte Carlo simulations [21]. Kanaya and Okayama have developed a closed-form expression which determines the trend of the electron penetration energy-loss [22]. Both these studies show that the peak of the electron energy deposition curve lies underneath the surface of the material. In this work, however, an exponential decay function with a coefficient having dependence on both acceleration voltage and material properties, proposed by Brown *et al.* [24], is used as an approximation to represent the electron energy decay in the material; this way, the surface temperatures obtained are upper bound estimates. The formulation of the heat source model is illustrated in Section 3.2.3.

3.2.3 Problem formulation

In the present model, an electron beam travels along $x-$axis at speed U over a semi-infinite solid (semi-infinite along the depth, $z-$axis), as shown in Fig. 3.1. The work-piece can be considered as an infinite solid when its size is much larger compared to the size of the heat source; the boundaries of the computational domain are selected far off from the heat source allowing to impose the boundary conditions for a semi-infinite solid, as illustrated in Section 3.3. The electron beam is treated as a volumetric heat source; the surface energy distribution is represented by a Gaussian function and an exponential decay function represents the energy distribution along the depth, as depicted in Fig. 3.1. The full width half maximum (FWHM) of the Gaussian function is considered as the beam diameter (d). The heat equation is solved in the subdomain to obtain the temperature distribution.

Melting is an important phenomena in any welding problem. An additional amount of power from the heat source is consumed in the material to overcome the latent heat of melting. Also, there is a discontinuity of the thermophysical properties at the solid-liquid interface in the material. Apart from that, the melting process in such a study of μEBW has limited influence in deciding the optimized Pe or the beam penetration. Hence, the effect of melting has not been included here as it would increase the solution complexity without providing significant information about the

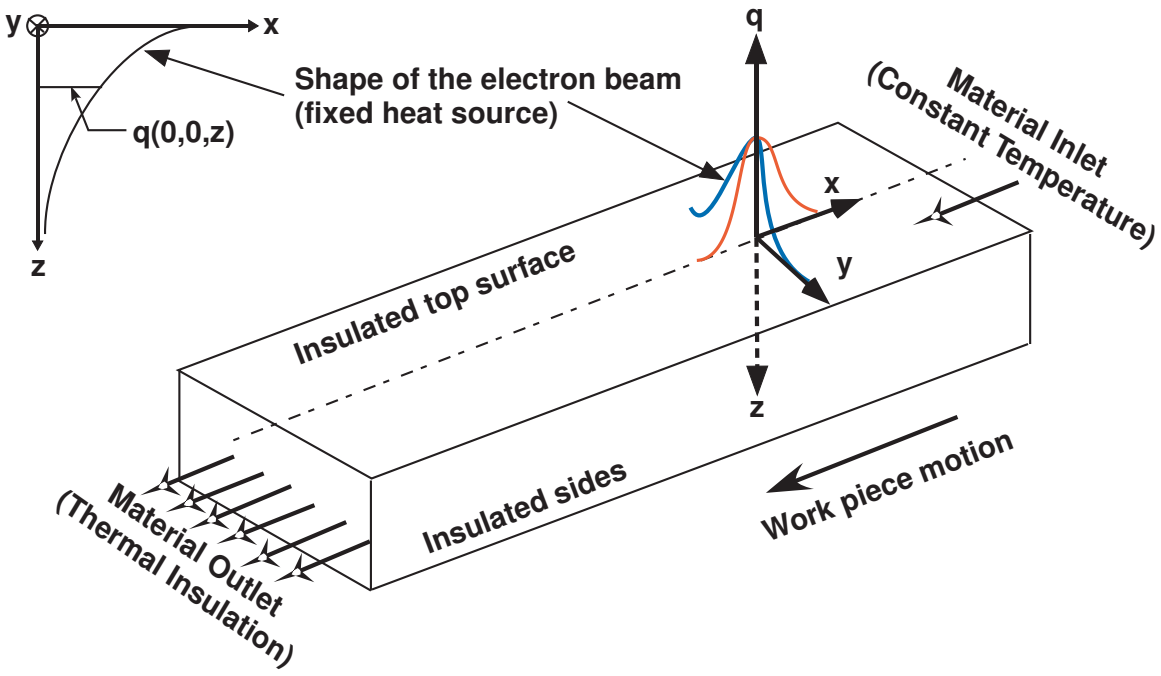

Figure 3.1 – Schematic representation of the computational domain, boundary conditions and shape of the heat source. The coordinate system is attached to the beam.

process. Similarly, heat loss due to evaporation and the effects of variation of thermophysical properties with the temperature, although significant, are outside the focus of the present study.

Governing equations

Fourier heat conduction equation is used to describe the heat transport in the solid of constant properties. A steady temperature field can be obtained by attaching the coordinate system to the moving heat source; which means, the material appears to be entering and leaving the computational domain at a velocity equal to U but along the negative x-axis, as shown in Fig. 3.1. The governing equation can be written as:

$$\frac{d}{\mathrm{Pe}}\left(\frac{\partial^2 T}{\partial^2 x}+\frac{\partial^2 T}{\partial^2 y}+\frac{\partial^2 T}{\partial^2 z}\right)+\frac{q}{\rho c_p U}+\frac{dT}{dx}=0 \tag{3.1}$$

where, q is the heat source, ρ and c_p are the constant density and heat capacity of the material. The coefficient of first term in Eq. (3.1) has the Pe in its denominator. For a high Pe process, this heat diffusion term becomes negligible. The second term in Eq. (3.1) represents heat generation, and the right hand side of the same equation represents the advection term resulting from attaching the coordinate system to the

moving heat source.

A round Gaussian distribution on the material surface and an exponential decay function along the penetration is used to represent the heat source [24], which can be written as:

$$q = q_{max} \exp\left(-\frac{x^2 + y^2}{2\sigma^2}\right) \exp\left(-\frac{z}{z_e}\right) \tag{3.2}$$

where, q_{max} is the maximum absorbed power per unit volume in the material, σ is defined as the standard deviation of the Gaussian function (=FWHM/2.355) and z_e represents the maximum electron penetration depth. The two unknown variables required to describe the heat source are q_{max} and z_e.

The maximum aborted power per unit volume in the material (q_{max}) can be calculated by applying the energy conservation principle between the input beam power and the heat absorbed in the material, which can be represented mathematically as:

$$\int_{x=-\infty}^{\infty} \int_{y=-\infty}^{\infty} \int_{z=0}^{\infty} q dx dy dz = \eta V I = \eta W \tag{3.3}$$

where, W is the total beam power, I is the beam current, and η is the efficiency parameter to account for the energy loss due to the backscattered electrons. In this work, η is represented as unity by considering the energy loss due to backscattering as negligible. The expression for heat source in Eq. (3.2) is substituted in Eq. (3.3). To solve the integration, following choice of the normalized space variables are made.

$$x^* = x/\sigma; \quad y^* = y/\sigma; \quad z^* = z/z_e \tag{3.4}$$

The heat balance equation can now be written using the normalized variables as:

$$q_{max} z_e \sigma^2 \int_{-\infty}^{\infty} \int_{-\infty}^{\infty} \int_{0}^{\infty} \exp\left(-\frac{x^{*2} + y^{*2}}{2}\right) \exp(-z^*) dx^* dy^* dz^* = W \tag{3.5}$$

With the knowledge of the following equality,

$$\int_{-\infty}^{\infty} \int_{-\infty}^{\infty} \int_{0}^{\infty} \exp\left(-\frac{x^{*2} + y^{*2}}{2}\right) \exp(-z^*) dx^* dy^* dz^* = 2\pi \tag{3.6}$$

the expression for q_{max} is derived as:

$$q_{max} = \frac{W}{2\pi z_e \sigma^2} \tag{3.7}$$

The maximum electron penetration depth (z_e) depends on the Kanaya-Okayama electron penetration range (R) [22], which is defined as:

$$R = 2.76 \times 10^{-5} \frac{AV^{1.67}}{\rho Z^{0.889}} \tag{3.8}$$

where, V is the acceleration voltage of the beam and is substituted in kV, and A and Z are the atomic weight and the atomic number of the substrate, respectively. The electron penetration range (R) represents the depth of the material within which 90% of the total beam energy is absorbed [24] and can be written as:

$$\frac{\int_0^R \exp\left(-\frac{z}{z_e}\right) dz}{\int_0^\infty \exp\left(-\frac{z}{z_e}\right) dz} = 0.9 \tag{3.9}$$

which leads to an expression for z_e as,

$$z_e = \frac{R}{2.3} \tag{3.10}$$

3.3 Numerical Analysis

The governing Eq. (3.1), where the heat source term is described using Eqs. (3.2) and (3.7), is solved numerically using a Finite Element based software COMSOL Multiphysics^{TM}. The GMRES (Generalized Minimal Residual) method is employed to solve the system of linear equations where "algebraic multigrid" method is used as a preconditioner. Such a technique is ideally suited for solving elliptic partial differential equations, as the given case. Also, the GMRES technique is very effective in handling large amount of data during the computation as it is based on iterative method. The GMRES method is especially suitable when highly dense grid in a three dimensional domain is required, as the present case, where memory handling is an issue. Further, the constraint handling by the solver is based on the "elimination" method and the relative tolerance is specified as 10^{-6}.

The constant material properties of stainless steel (AISI 304) as shown in Table 3.2 are used as an example in this study.

Meshing the geometry in moving heat source problems is a challenging task. In case of volume distributed heat sources, large number of mesh elements should be allocated to resolve the effect of series of instant point heat sources which form the volume. Nearby the heat source, the grid density depends on the Pe of the process;

Table 3.2 – Properties for AISI 304 at 27^0C [36]

Properties	Values	Units
k	14.9	[W m^{-1} K^{-1}]
ρ	7900	[kg m^{-3}]
c_p	477	[J kg^{-1} K^{-1}]
T_m	1400	[^{0}C]
T_0	27	[^{0}C]

where, higher Pe processes result in steep temperature gradients and hence require larger number of grid elements. Since various weld speeds and shapes of the heat source are studied in the present work, specific meshes has been generated in each case and grid independent study has been carried out until stable solution is achieved. The following three steps are followed in general to create the mesh:

1. A point at the center of the heat source is chosen.
2. Maximum element size is specified locally as 0.01 times the beam diameter and element growth rate as 1.5.
3. Mesh is refined using the default refinement options of COMSOL Multiphysics^{TM} until a grid independent solution is obtained

In Table 3.3, the summary of the grid independent study for a trial case, where welding speed is specified by Pe=1000 and shape of the beam is defined by 10μm beam diameter and 50kV electron penetration. The maximum temperature of the solution is compared with that obtained prior to the grid refinement and percentage deviation is found for each case. It is observed that the improvement in solution is not significant between first and second refinement and hence the mesh with 44,456 tetrahedral elements is considered appropriate for the given case. The three-dimensional brick shaped subdomain after meshing is shown in Fig. 3.2.

The selection of the domain size is based on the preference of obtaining the temperature field accurately near the heat source; for which, the smallest possible subdomain meshed with large number of grid elements is ideally suited. The width of the block along $y-$axis and the depth of the block along $z-$axis, in which there is no beam movement, are decided such that the temperature gradient is negligible at the boundaries in the representative cases. Hence, both faces of the rectangular block along y direction and the bottom face of the block along z direction are imposed insulation

Table 3.3 – Grid dependency of temperature calculations: Domain size = 80 μm × 40 μm × 20 μm, Pe=100 and V=50 kV

Refinement (i)	Number of tetrahedral elements	Deviation % $\frac{T_{i,max}-T_{i-1,max}}{T_{i,max}-T_0} \times 100$
0	15557	-
1	44456	2.6
2	95694	0.9

boundary condition as shown in Fig. 3.1. To decide the length of the work piece in the numerical model, many simulations with different lengths were carried out with coarse meshes. The minimum length for which the temperature field in the region close to the heat source is almost unaffected is found out; the minimum length ahead of the heat source is found to be six times the beam diameter for insulation boundary condition being applied at that boundary. Similarly, behind the heat source the work piece flows in at room temperature; the boundary, if selected very close to the heat source, will result in faulty solution. The preliminary numerical studies showed that the minimum length behind the heat source should be two times the beam diameter.

Although there cannot be any convection heat losses as the process operates in a vacuum chamber, heat loss due to radiation is expected to occur at the top boundary. Considering an emissivity of 0.3 [36] on the surface and maximum surface temperature of about 3200 ^{0}C in the present model, the maximum radiation heat flux is found to be in the order of 10^6 W m^{-2}. On the other hand, the maximum incident heat flux from the electron beam as obtained from the numerical solution is in the order of 10^{14} W m^{-2}; it is to be noted here that the heat intensity value possible in the numerical model falls in the no welding zone according to Fig. 1.1. The contribution of radiation heat loss is insignificant against the high intensity incident beam and hence the top surface can be represented as insulated.

3.4 Validation of the Numerical Solution

The numerical solution can be validated by comparing the temperature field against the exact solutions of the asymptotic cases. At distances far from the heat source, the well-known Rosenthal's point heat source solution [28] can be used for the comparison. In the Rosenthal solution, the temperature at the center of the point heat source becomes infinitely high; so, to understand the behavior of the temperature field near

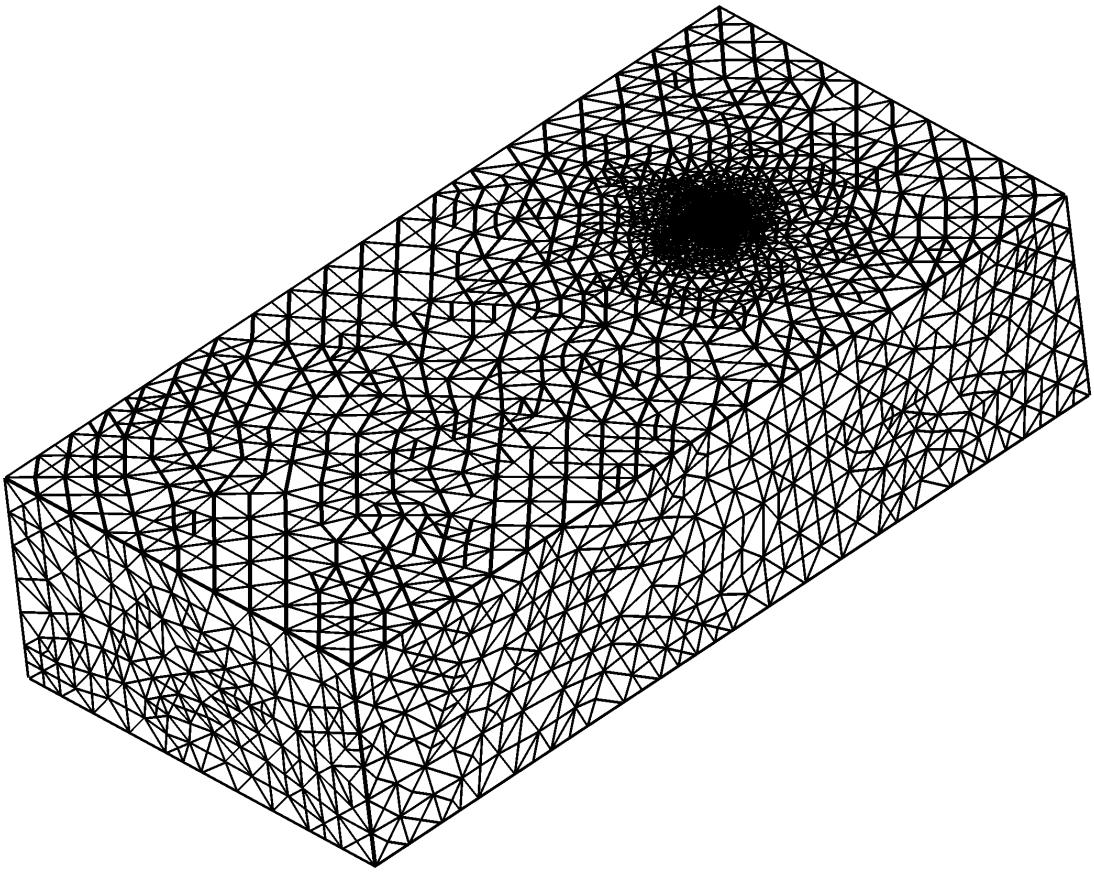

Figure 3.2 – Mesh showing the non-uniform distribution of tetrahedral elements in the three-dimensional computational domain.

the volumetric heat source, an analytical solution has been developed based on the available literature [24, 27].

3.4.1 Far-field temperature

The point heat source solution considers heat conduction in a solid of constant thermal properties (Table 3.2) and no surface heat loses; the entire beam power is applied at a point on the surface moving at a constant velocity. The analytical expression for three dimensional temperature field in case of a point heat source, as provided by Rosenthal [28] is:

$$T - T_0 = \frac{W}{2\pi kr} \exp\left(\frac{-Ux}{2\alpha}\right) \exp\left(\frac{-Ur}{2\alpha}\right) \tag{3.11}$$

where, r represents the distance from the heat source.

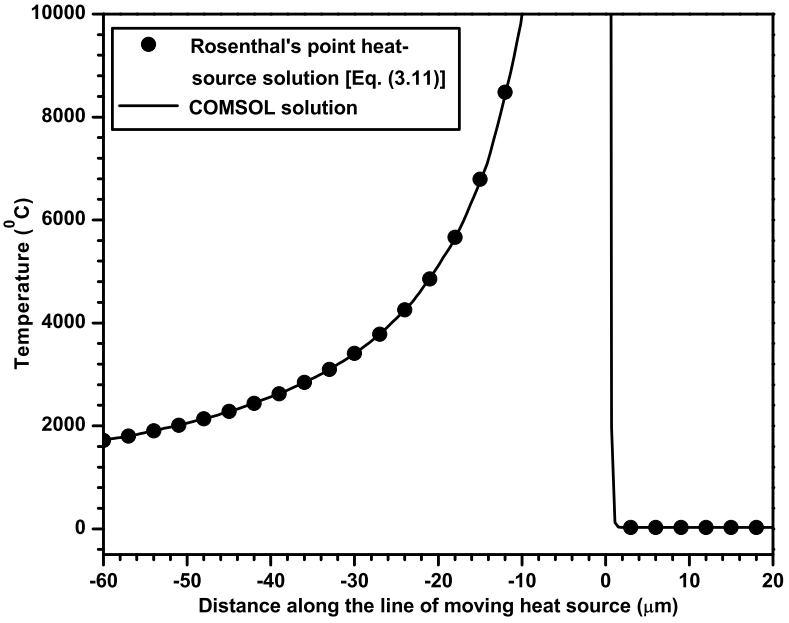

Figure 3.3 – Comparison of Rosenthal's point heat source solution and the numerical results for temperature variation along the center line (W=9.5 W, k=14.9 W m^{-1} K^{-1}, U=25 m s^{-1}, d=0.2 μm, and z_e=0.1 μm).

The case of point heat source is solved numerically by reducing the scale of the volumetric heat source described in Eq. (3.1). A beam diameter of 0.2 μm and a maximum electron penetration depth of 0.1 μm is chosen to carry out the numerical simulations. The maximum power absorbed per unit volume (q_{max}) is modified according to the choice of σ and z_e using Eq. (3.7). Adaptive meshing technique, which introduces additional mesh elements while solving based on the excess temperature gradients in the domain, is applied in addition to the meshing procedures described in the Section 3; the final mesh consisted of 257,457 tetrahedral elements.

The temperature variation on the surface along the line of the moving heat source ($x-$axis) is compared between the numerical and the Rosenthal's solution in Fig. 3.3; where, the solid circles represent the analytical solution obtained using Eq. (4.17). This graph illustrates the heating of the material as it approaches the beam and the sub-sequent cooling due to the heat diffusion. An excellent agreement of the temperature prediction between the numerical model and the analytical solution for the point heat source is observed in the far-field.

3.4.2 Temperature profile under the beam

A good way to validate the numerical solution near the heat source is to solve for the simplest form of the heat equation without the heat diffusion terms and compare it to the analytical solution, which can be derived without much difficulty. In the present work, an analytical solution has been developed considering no conduction term in Eq. (3.1), to provide the temperature field in the material. In the numerical solution, the thermal conductivity, which is the coefficient of the diffusion term in the heat equation, is decreased gradually until the temperature field in the solution ceases to vary in consecutive simulations. The temperature field thus obtained with negligible heat diffusion is said to have reached the asymptotic maximum. It is observed that the asymptotic maximum value of temperature in the numerical solution is attained for an artificial thermal conductivity of k=10^{-3} W m^{-1} K^{-1} that corresponds to Pe=9.4×10^5.

The governing equation for this case is an ordinary first order differential equation, which can be written as:

$$\rho c_p U \frac{dT}{dx} = q \tag{3.12}$$

Equation (3.12) can be written in the non-dimensional form using the normalized variables provided in Eq. (3.4), and the following normalization for temperature:

$$T(x, y, z,) = T_0 + \Delta T_{max} T^*(x^*, y^*, z^*) \tag{3.13}$$

where, $\Delta T_{max} = T_{max} - T_0$ and T^* is the normalized temperature. The heat source term is substituted using Eq. (3.2) to form the non-dimensional governing equation,

$$\rho c_p \Delta T_{max} \frac{U}{\sigma} \frac{dT^*}{dx^*} = q_{max} \exp\left(-\frac{x^{*2} + y^{*2}}{2}\right) \exp\left(-z^*\right) \tag{3.14}$$

In case of negligible conduction, the temperature at any point in the substrate rises to its maximum value by absorbing the beam energy during the entire span of beam motion. The limits of the integration to be applied in Eq. (3.14) to obtain the maximum possible temperature at a location, specified by the y and z coordinates, in the domain are: T^*=0 when x^* is -∞ and T^*=1 when x^* is +∞. It is important to note here that the value of the maximum temperature at a given point in the substrate depends on its position; where, the temperature is expected to decrease with the increase in distance from the heat source. To calculate the maximum temperature

of the process in the present model of μEBW, a point is selected on the top surface along the line of heat source ($y^* = 0$ and $z^* = 0$).

$$\rho c_p \Delta T_{max} \frac{U}{\sigma} \int_0^1 dT^* = q_{max} \int_{-\infty}^{\infty} \exp\left(-\frac{x^{*2}}{2}\right) dx^* \tag{3.15}$$

On solving,

$$\Delta T_{max} = \frac{\sqrt{2\pi} q_{max} \sigma}{\rho c_p U} \tag{3.16}$$

where, q_{max} can be substituted using Eq. (3.7), and the final expression for maximum temperature of the process is derived as:

$$T_{max} = T_0 + \frac{W}{\sqrt{2\pi} \rho c_p U z_e \sigma} \tag{3.17}$$

The variation of surface temperature along the center line can be obtained as a function of x by integrating Eq. (3.14) as:

$$\rho c_p \Delta T_{max} \frac{U}{\sigma} \int_0^{T^*} dT^* = q_{max} \int_{-\infty}^{x^*} \exp\left(-\frac{x^{*2}}{2}\right) dx^* \tag{3.18}$$

On solving and substituting q_{max} using Eq. (3.16), one can obtain the centerline temperature as:

$$T = T_0 + \frac{\Delta T_{max}}{2} \left[1 + \text{erf}\left(\frac{x^*}{\sqrt{2}}\right)\right] \tag{3.19}$$

The temperature field obtained from the numerical solution for an artificially low thermal conductivity of k=10^{-3} W m^{-1} K^{-1} is compared to the analytical solution in Eq. (4.18), along the line of the moving heat source on the surface of the material. The normalized variable, x^*, in Eqn. (4.18) has been converted into the space variable, x, using Eq. (3.4). The material is initially at room temperature, as seen at the right end of the $x-$axis in Fig. 3.4; it heats up gradually as it approaches the heat source. The temperature finally reaches its maximum value, and does not cool down as negligible heat diffusion has been considered. An excellent match between the numerical and the analytical solution is observed.

Furthermore, the weld penetration (or the maximum melting depth) and maximum weld width can be estimated using the same analytical solution as above. The maximum melting depth can be obtained beneath the centerline of the heat source

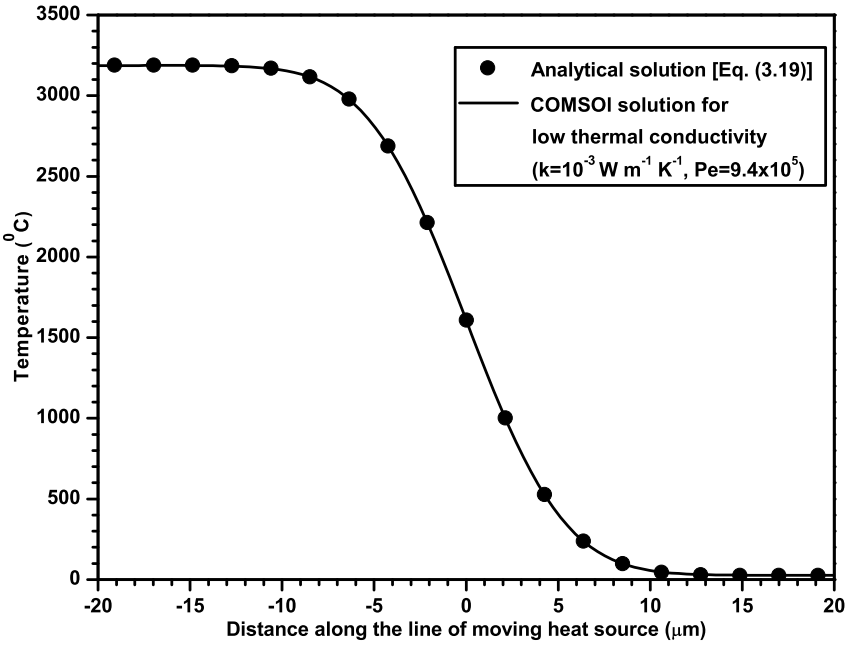

Figure 3.4 – Comparison of analytical and numerical results for temperature variation along the centerline considering negligible conduction.

and at the location of maximum surface temperature, for the present model of μEBW. The lowest position of the melting region is represented as z_m, which would rise to the maximum value of melting point by absorbing the beam energy during the entire span of the beam motion. The integration can now be carried out similar to Eq. (3.15) but for $y^* = 0$ and $z^* = z_m/z_e = z_m^*$. Also, the upper limit of the temperature rise is melting point in this case, which is represented by T_m^* in the normalized form.

$$\rho c_p \Delta T_{max} \frac{U}{\sigma} \int_0^{T_m^*} dT^* = q_{max} \exp(-z_m^*) \int_{-\infty}^{\infty} \exp\left(-\frac{x^{*2}}{2}\right) dx^* \tag{3.20}$$

such that, $\Delta T_{max} T_m^* = \Delta T_m$. Substituting q_{max} using Eq. (3.16), the expression for maximum melting depth (or weld penetration) is obtained as:

$$z_m = z_e \ln\left(\frac{\Delta T_{max}}{\Delta T_m}\right) \tag{3.21}$$

Now, the maximum weld width can be obtained similarly by choosing a point y_m on the top surface which rises to the maximum value of melting point. Equation

(3.14) is written for $z^* = 0$ and $y^* = y_m/\sigma = y_m^*$ as:

$$\rho c_p \Delta T_{max} \frac{U}{\sigma} \int_0^{T_m^*} dT^* = q_{max} \exp\left(-\frac{{y_m^*}^2}{2}\right) \int_{-\infty}^{\infty} \exp\left(-\frac{x^{*2}}{2}\right) dx^* \tag{3.22}$$

$$\rho c_p \Delta T_m \frac{U}{\sigma} = \sqrt{2\pi} q_{max} \exp\left(-\frac{{y_m^*}^2}{2}\right) \tag{3.23}$$

Equation (3.16) is used to substitute q_{max} and the final expression for maximum weld width is obtained as:

$$y_m = \sigma \sqrt{2 \ln\left(\frac{\Delta T_{max}}{\Delta T_m}\right)} \tag{3.24}$$

In addition to validating the numerical model, the simplified expressions of the analytical solution serves to estimate the maximum range of the welding parameters beforehand. The analytical solution can also be used directly or with suitable correction factors, without the need of numerical solution, for the cases of μEBW considering very fast moving heat sources; Such processes have high Pe and where conduction ceases to play a significant role.

3.5 Parametric Study

The μEBW is governed by four key process parameters: the beam voltage controls the depth of electron penetration in the material; the beam current controls the total number of electrons striking on the material and is a measure of the total energy input; the beam diameter is decided based on the feature size and the required weld dimensions; the beam velocity determines the spot residence time and hence the energy dose provided. For a given size of the weld, the suitability of the choice of aforementioned parameters is decided based on the amount of heat flow outside the weld bead, controllability, and the maximum temperature of the process. In this study, the impact of the input parameters on the feasibility of microwelding is investigated by independently examining the effect of the Pe and the penetration of electrons (related to the acceleration voltage).

3.5.1 Effect of Pe

The effect of Pe on μEBW is studied by considering a weld on 304 stainless steel with a fixed beam diameter of 10 μm and an acceleration voltage of 50 kV. The maximum electron penetration depth (z_e) for this voltage and material is 3 μm. The Pe of the

process is varied by changing the beam travel speed. It is desired to produce the same amount of melting along the depth for different Pe processes so that the heat flow under the beam can be compared. A fixed maximum melting depth of 2.5 μm is chosen for the present study. The different amounts of heat required to produce the same maximum melting depth for variable Pe processes is met by varying the beam current.

In Fig. 3.5, the variation of temperature along the depth, at the point of maximum surface temperature, is plotted for Pe=1, 100, and 10000. The position of maximum surface temperature along $x-$axis is represented non-dimensionally as x^* in the same figure. The peak of the temperature distribution curve has an off-set beyond the center of the Gaussian heat source as the Pe increases. This is because the rate at which energy is deposited in the direction of beam motion is higher compared to the rate of heat diffusion as Pe increases. In Fig. 3.5, point P corresponds to the melting temperature at the specified maximum melting depth of 2.5 μm.

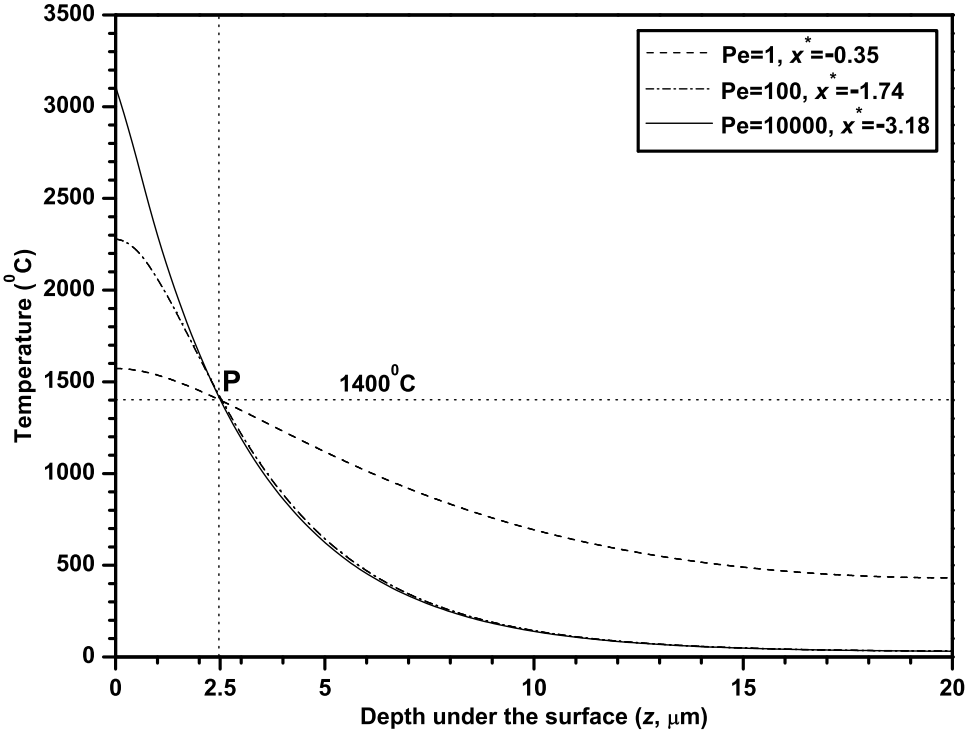

Figure 3.5 – Effect of Pe on the variation of maximum temperature along the depth.

Excess heat

Figure 3.5 shows the variation of maximum temperature along the depth of the material. For high Pe process (Pe=100 and Pe=10000), the material at about 15 μm

beneath the surface is not significantly affected by the presence of the heat source on the top. However, the process with Pe=1 produces a more even temperature distribution in the material; the outer edge of the domain in the numerical model, which is twice the beam diameter far from the heat source, is heated up to 400 ^{0}C. It is important to note that the temperature prediction at the outer boundary is also influenced by the choice of insulation boundary condition. The Pe of the process, which governs the amount of heat diffusion in the material, dictates the trend of these temperature distribution curves. It is observed that having a μEBW of lower Pe results in a larger amount of thermal energy flowing into the depth of the material.

Lower Pe processes also produces higher heat flow along the width of the material (or into the adjacent components). Figure 3.6 shows the variation of surface temperature along the width of the rectangular block for different Pe processes; this temperature distribution is obtained at the longitudinal location of maximum temperature on the surface, given by the values of x^* in the same plot. The peak of the temperature distribution curve for each case of Pe correspond to that shown in Fig. 3.5 and represent the maximum temperature of the process. The width of the weld is obtained by measuring the length of intersection of the temperature distribution curves and a line corresponding to the melting temperature, as depicted in Fig. 3.6. The weld width becomes narrower with smaller Peclet numbers. Although narrower welds can be considered advantageous for microwelding, lower Peclet numbers are not a viable option taking into account the amount of thermal damage caused to the material during the process.

Heat input is another way to study the amount of heat transmitted outside the weld bead. It is typically defined as [37]:

$$\text{HI} = \frac{\eta V I}{U} \quad [J/m] \tag{3.25}$$

The effect of Pe on the heat input of the process is shown in Fig. 3.7. The heat input decreases with the increase in Pe of the process and finally reaches it asymptotic minimum. The high requirements of heat input at lower Pe is because of the excessive amount of heat loss into the larger volume of the material through thermal diffusion. At higher Pe, the role of conduction becomes insignificant and the heat input settles down to its minimum asymptotic value.

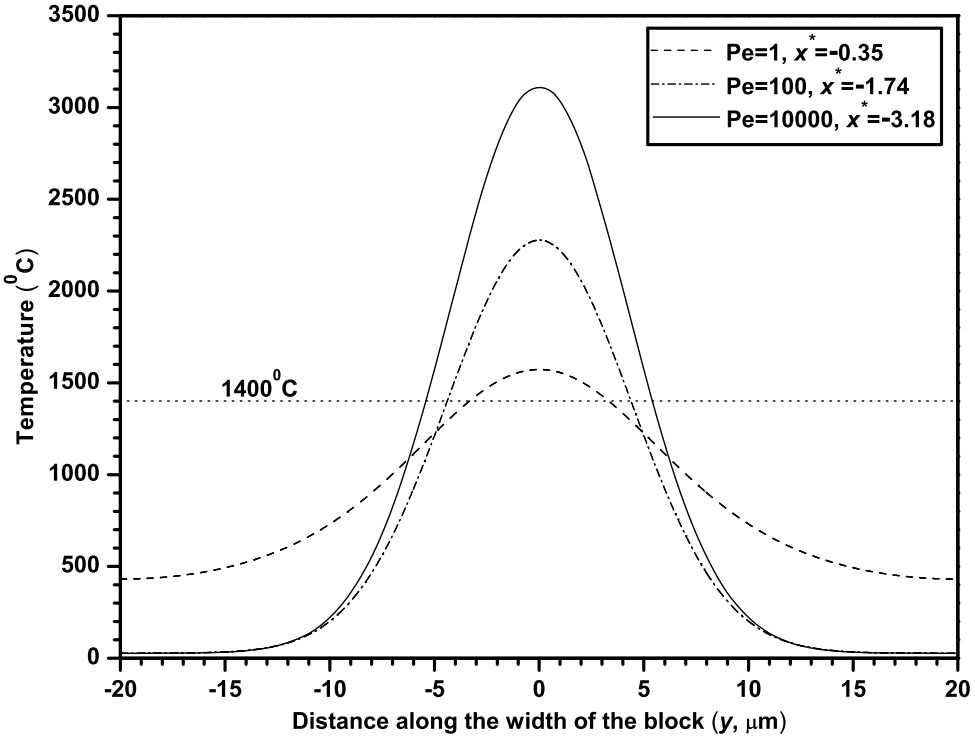

Figure 3.6 – Effect of Pe on the variation of maximum temperature along the width.

Controllability

Important aspects of the controllability of microwelding can be explored by examining the change in the weld penetration with respect to the temperature gradient. The gradient of temperature distribution curve is obtained at the maximum melting depth denoted by point P in Fig. 3.5 for different Pe processes. In Fig. 3.8, the slope has been represented along $y-$axis in the inverse form to signify the change of maximum melting depth per unit temperature gradient. At high values of Pe, the sensitivity of maximum melting depth with temperature gradient is constant with a dimensionless value of approximately 1. For Peclet numbers below 100, however, the sensitivity increases rapidly, suggesting an increasingly unstable process. For illustration purpose, consider the cases of Pe=1 and Pe=100 from Fig. 3.8; where, the case of Pe=1 shows an increase of the sensitivity by a factor of 5. Hence, it can be deduced that the maximum melting depth increases five times for a given temperature gradient between the cases of Pe=1 and Pe=100. The sensitivity level in the low Pe microwelding is extremely high which suggests that a slight variation in the experimental conditions and thus the temperature distribution, can cause significant variation in the weld penetration. On the other hand, high Pe process provides the

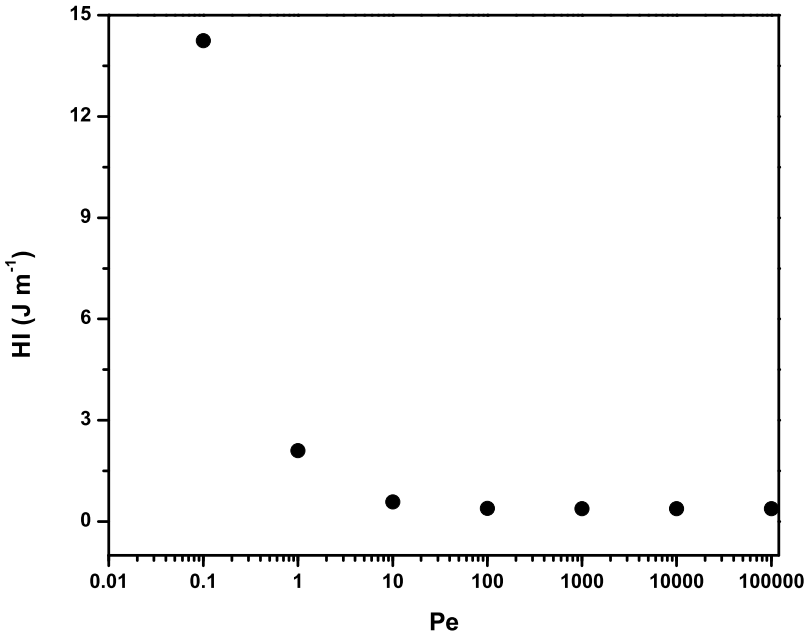

Figure 3.7 – Variation of non-dimensional heat input of the process with the Pe.

maximum controllability during microwelding.

Maximum temperature

The effect of Pe on the maximum temperature of the process is shown in Fig. 3.9. The maximum temperature of the numerical solution is non-dimensionalized with respect to the maximum temperature of the analytical solution in Eq. (3.17); the values shown in Fig. 3.9 corresponds to the peak temperatures in Figs. 3.5 and 3.6. The maximum temperature of the process increases with the increase in Pe until it reaches the asymptotic regime of unity at around Pe=10000. This is in agreement with the theory that less thermal diffusion at higher Pe causes heating of a localized region of the body to higher temperatures. Having a lower maximum temperature of the process at smaller Pe can be considered advantageous for microwelding as it decreases the amount of surface ablation. However, there are other disadvantages associated with low Pe process, as discussed previously, which has to be considered prior to making a choice.

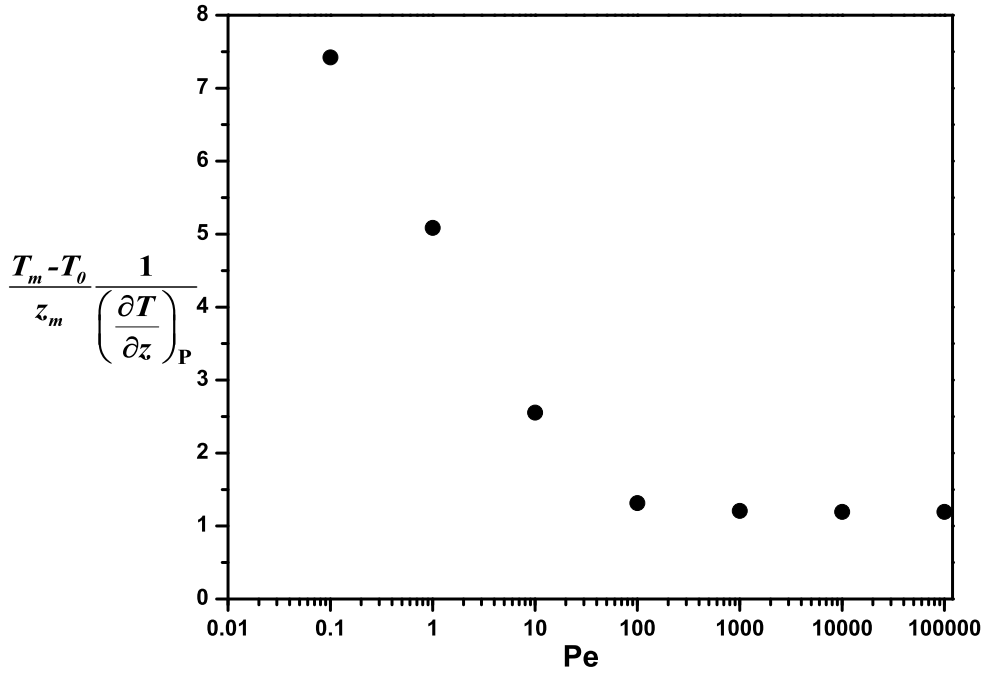

Figure 3.8 – The gradient of the maximum melting depth with respect to temperature at point P in Fig. 3.5 is plotted in non-dimensional form against Pe of the process.

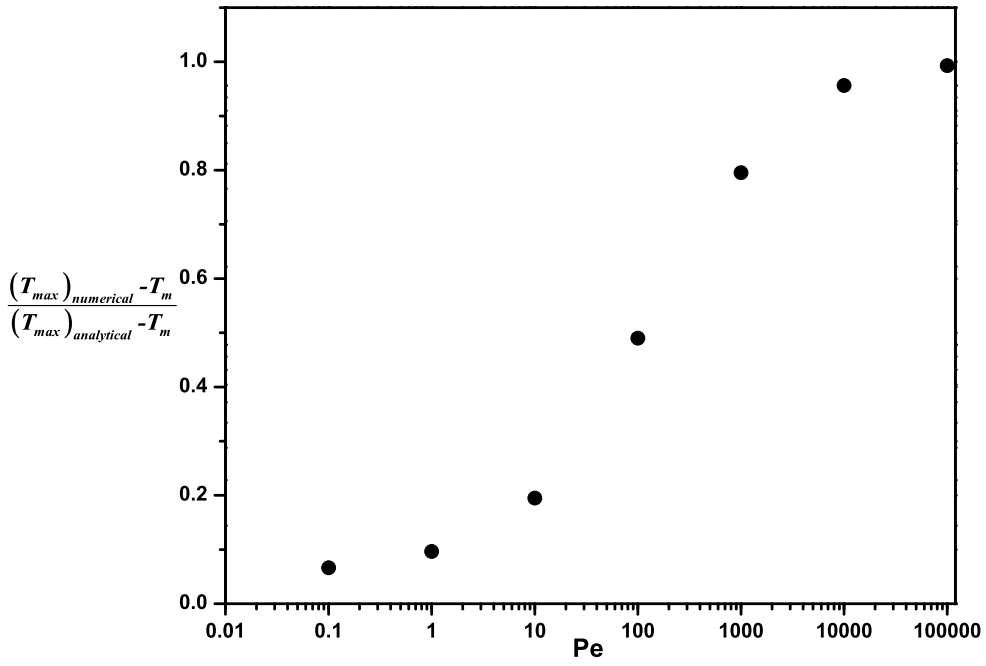

Figure 3.9 – Variation of non-dimensional maximum temperature of the process with Pe.

3.5.2 Effect of acceleration voltage

The greatest advantage of the electron beam for microwelding over lasers or small arcs is that it can be used to generate heat volumetrically. This volume heating nature is described by the amount of penetration of the electrons in the material which in turn is controlled by the acceleration voltage of the beam. This section focusses on finding the optimal value of the maximum electron penetration depth for a required amount of melting.

Five cases of different maximum electron penetration to maximum melting depth ratio are considered: 0.12, 0.4, 1, 4, and 8. The effect of the beam penetration on excess heat, controllability, and maximum temperature of the process is investigated. A constant Pe of 100 is chosen for all the processes such that heat conduction is negligible. It is desired to produce a maximum melting depth of 2.5 μm for different cases of beam penetrations. The acceleration voltage of the beam is decided by the magnitude of maximum electron penetration depth required in each case; the heat requirement to obtain specified maximum melting depth is met by varying the beam current.

Excess heat

The variation of temperature along the depth at the longitudinal location of maximum surface temperature (x^*) is plotted in Fig. 3.10 for different non-dimensional maximum electron penetration depth. The maximum melting depth of 2.5 μm, which is represented by P' in the same figure, is obtained below the point of maximum surface temperature. The temperature distribution curves decrease in steepness for increasing non-dimensional maximum electron depth. For the cases of z_e/z_m=0.4 and 1, the temperature of the body at about 15 μm beneath the surface is not affected by the presence of the heat source. With the further increase in the electron penetration (e.g. z_e/z_m=4), the temperature distribution curve becomes more even in the sub-domain. This is because the excess energy is transported into the material depth due to the direct action of electrons.

The heat input is also compared between processes with different electron penetrations. In Fig. 3.11, the variation of the heat input is plotted against z_e/z_m. A spline best fit curve is used to join the discreet points. For the minimum heat input of the process, the optimal electron penetration variable is expected to be in the range of 0.8-1.2 times the maximum melting depth. The heat input is higher for

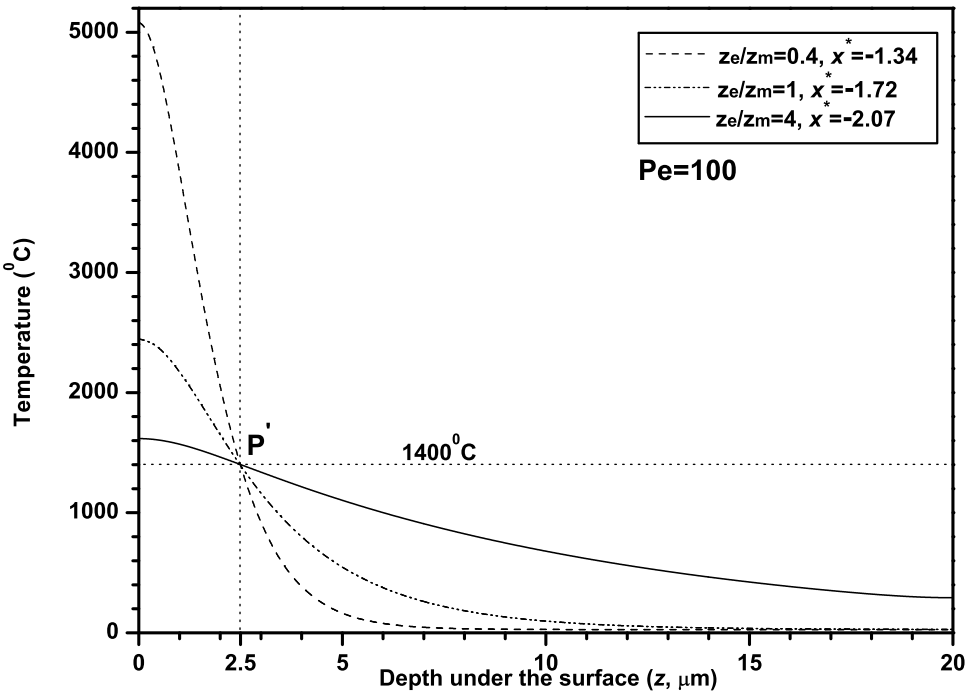

Figure 3.10 – The effect of electron penetration on the variation of maximum temperature along the depth.

the cases of under-penetration or excess-penetration for different reasons. In case of under-penetration, higher heat input is required to reach the melting depth through diffusion, while, for excess electron penetration, higher voltages and hence high beam power is required.

Controllability

The effect of variable electron penetration is investigated on the controllability of μEBW. The gradient of temperature with respect to the depth is obtained at point P$'$ in Fig. 3.10, and the non-dimensional form is represented inversely along y-axis, as shown in Fig. 3.12. The sensitivity of the weld penetration with respect to the temperature gradient increases with the increase in non-dimensional maximum electron penetration depth. The large factors of sensitivity when the maximum electron penetration is higher than the maximum melting depth (z_e/z_m >1), suggests increasingly unstable process; on the other hand, the smaller penetration values (z_e/z_m <1) suggests better controllability. However, there are other important considerations related to excess heat input and maximum temperature involved in deciding the best electron penetration for a given maximum melting depth.

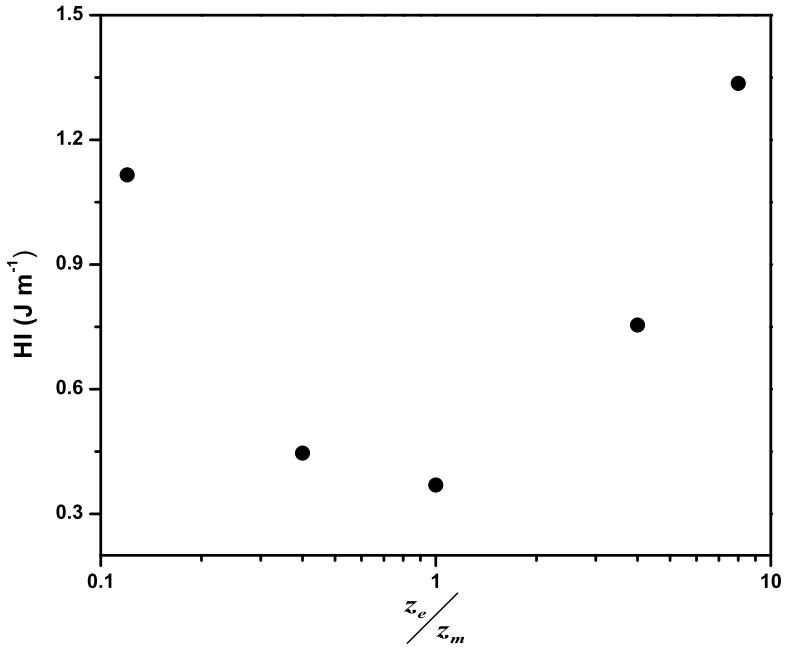

Figure 3.11 – Variation of non-dimensional heat input of the process with the non-dimensional maximum electron penetration depth.

Maximum temperature

The maximum temperature of the process is compared for different electron penetrations, all of which producing the same melting depth. The non-dimensionalized maximum temperature is plotted against the non-dimensional maximum electron penetration depth in Fig. 3.13. When the maximum electron penetration is about one-tenth of the maximum melting depth, the maximum temperature of the process is observed to be about ten times the maximum temperature of the asymptotic limit of high Pe. This is because the heat of melting is transported from the surface into the depth through conduction with large gradients, resulting in very high temperatures at the surface. The maximum temperature of the process gradually falls and then follows the melting temperature line asymptotically, as the maximum electron penetration depth is increased. In this case, the enthalpy at the melting depth is obtained by the direct interaction with the electrons and hence the temperatures at the surface and the melting depth are comparable.

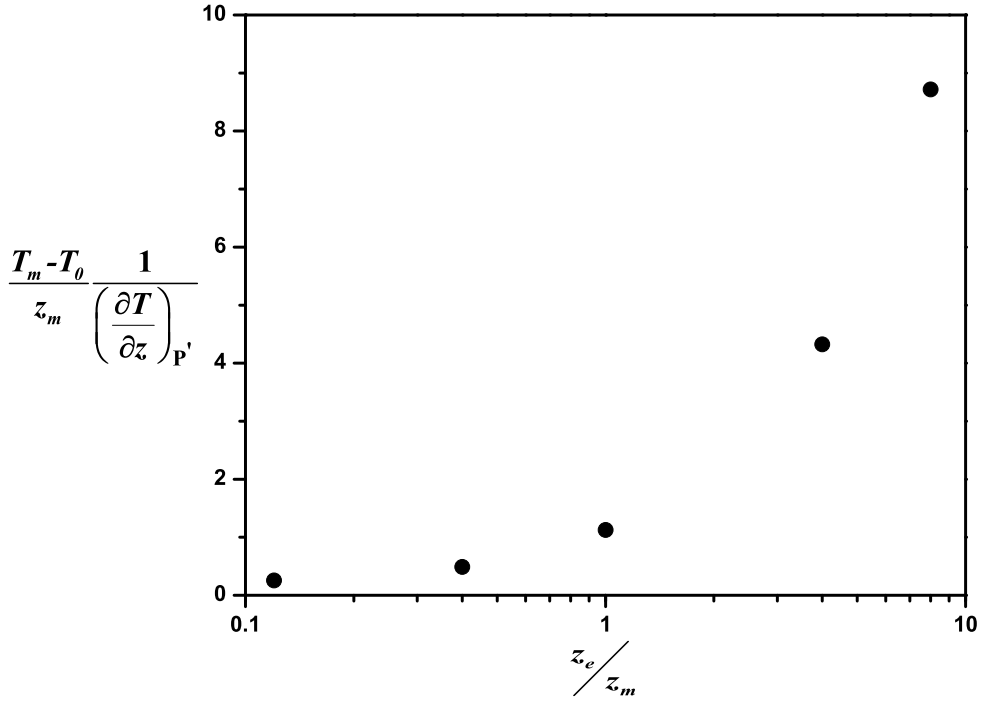

Figure 3.12 – The non-dimensional gradient of the maximum melting depth with respect to temperature at point P′ in Fig. 3.10 is plotted against the non-dimensional maximum electron penetration depth.

3.6 Discussion

This study leads to the selection of optimized weld speed and electron beam penetration (acceleration voltage) to form a weld of given size in a material of known properties; where, the excess heat input, controllability, and maximum temperature of the process serves as a criteria to decide the feasibility of μEBW. The heat intensity values corresponding to processes with Pe=100 and higher and having beam penetration in the range of 0.8-1.2 times the melting depth, as obtained from the numerical solution, varies in between 10^{12} to 10^{14} W m^{-2}; these high heat intensity values fall in the no welding zone as seen in Fig. 1.1. The adiabatic volumetric interaction of the electrons with the region of melting enables the use of such high heat densities, previously considered unsuitable for welding because of excessive ablation [5, 6]. The possibility of exploring beyond the critical heat intensity limit to use it to advantage for welding micron and submicron scale is proposed for the first time in this research and established by the heat transfer analysis.

The simplification made in representing the heat distribution of an electron beam

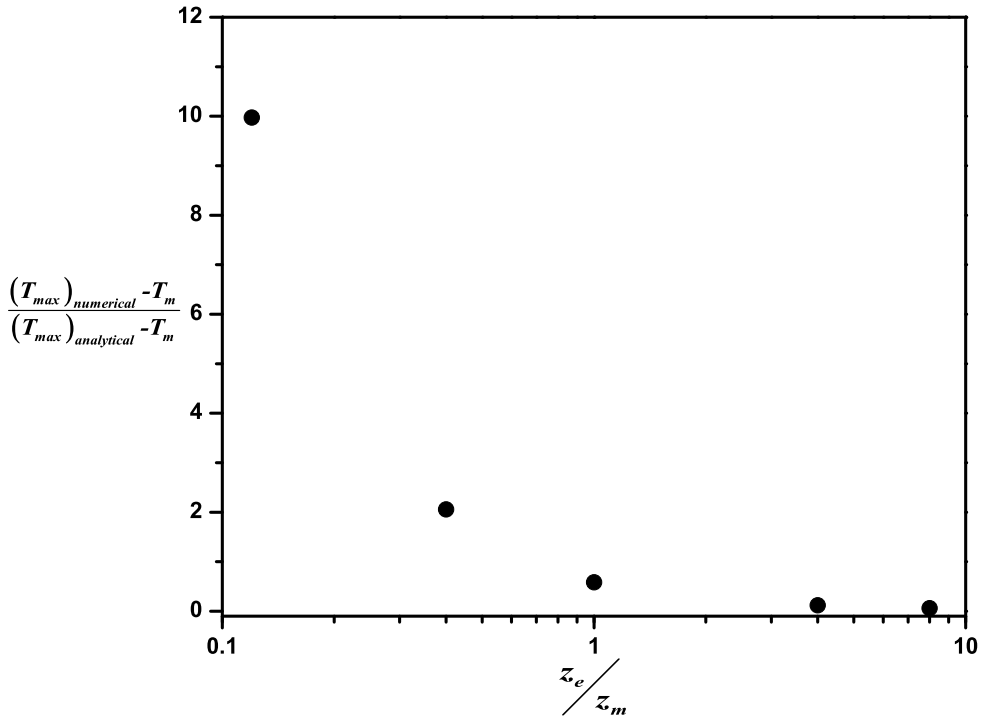

Figure 3.13 – Variation of non-dimensional maximum temperature of the process with the non-dimensional maximum electron penetration depth.

along the penetration might change the optimal values of the proposed parameters, without affecting the viability of the study. The actual shape of the electron energy decay curve along the depth resembles an offset Gaussian, with the peak of the energy dissipation residing slightly beneath the surface. Hence, the maximum temperature of the process is expected to be underneath the surface and this would result in decreased rate of ablation due to the lower surface temperatures, as compared to the current analysis.

The present study does not take into account the back-scattering phenomenon of the electrons, which affects the heating efficiency. A typical 10keV electron beam, when impinged on a copper substrate, is expected to loose 30% of its energy in back-scattering [22]. The efficiency parameter in this study (η) can be suitably modified, which would result in higher values of beam current to perform a similar microwelding operation.

Phase transformations involving latent heat such as evaporation and melting, are likely to influence the optimal values of the parameters of the present study. Higher

beam currents compared to the current predictions would be required to account for the the aforesaid processes. The temperature distribution curves in the solid and liquid phases are also expected to slightly vary from what is predicted now.

The optimal value of the maximum electron penetration depth is found to be of the same order of the melting depth because of the choice of a negligible conduction process (Pe=100). Any choice of Pe above 100 would not affect the result as the conduction does not improve and the energy is carried to the melting depth by the electron penetration only. But for a choice of lower Pe process, where heat diffusion starts to play a major role in transferring the thermal energy, the optimal electron penetration is expected to be different than the required melting depth.

The length scale chosen to define Pe in this study is the beam diameter, based on which the optimum Pe is found to be 100. Such a consideration is valid when the length scale of beam diameter is of the same order of magnitude as the beam depth. The optimum Pe is expected to increase when the beam diameter is chosen much larger than the weld depth.

3.7 Conclusions

The theoretical results presented here indicate that a volumetric heat source could enable fusion welding in a region of parameters considered impossible until now because of intrinsic limitations of traditional (surface) heat sources. This region of parameters considered impossible, however, is centrally relevant to the practical implementation of joining at the micron scale. Electron beams are ideally suited for this task due to their inherent micron-scale penetration under the surface of the target material.

The heat transfer study presented here reaches in to a previously less explored area of volumetric moving heat sources. A numerical model has been developed to solve three dimensional heat conduction equation involving moving volumetric heat sources. The model has been validated by comparisons with the analytical solutions to asymptotic cases far and near the heat source. The temperature field due to conduction is matched with the Rosenthals point heat source solution far from the beam. Under the beam, the temperature distribution agrees well with the analytical solution obtained ignoring conduction.

The numerical solution is used to obtain an optimized set of beam parameters

in the non-dimensional form, such as Pe and relative beam penetration, for a given material and weld size. The current analysis, considering the properties of AISI 304 steel, indicates that a Pe of 100 and a maximum electron penetration in the range 0.8 to 1.2 of the maximum melting depth are optimal to maintain a desirable balance of maximum temperature, controllability, and heat input into the component.

Model outputs suggest that at Peclet numbers larger than 100, the process requirements (e.g. beam velocity) increases without meaningful gains in controllability, excess heat or maximum temperature. At Peclet numbers below 100, the maximum temperature of the process lowers; however, the process quickly loses controllability and there is excessive heat lost into the substrate surrounding the weld. At electron penetrations below $0.8z_m$, the process starts to resemble a traditional surface heating process such as laser welding consistent with potentially excessive surface ablation. At electron penetrations above $1.2z_m$, the process results in excessive direct heating beyond the depth of the weld, possibly damaging the surroundings of the device being welded, and worsening the controllability of the process.

Chapter 4

Behavior of Kanaya-Okayama Heat Source in Micro Electron Beam Welding[1]

A three dimensional distributed heat source model is developed to represent an electron beam as a heat source based on the electron penetration theory proposed by Kanaya and Okayama [*Kanaya and Okayama, J. Phys. D: Appl. Phys.,* ***5(1)****, 1972*]. The fraction of electron energy absorbed in the substrate is calculated theoretically for the fist time to provide the heating efficiency of the electron beam. Further, the heat source model is applied in the numerical analysis of micro electron beam welding and the results are compared with those of the exponential decay heat source model used previously. The optimum Peclet number of the process to be 100 and the beam penetration to be twice that of the maximum melting depth as obtained using the Kanaya-Okayama heat source model are similar to the previous findings using the exponential decay heat source model. However, the predictions of the temperature field in the solid as a result of microwelding are relatively lower in case of Kanaya-Okayama heat source model because of the differences in the distribution of heat into the condensed matter. The lower weld surface temperatures in microwelding using the electron beam suggest less ablation as opposed to the use of laser beams.

4.1 Introduction

Micro Electron Beam Welding (μEBW) is a relatively new welding technology that uses heating from an electron beam to weld micron scale sections. Recent endeavors have been to numerically simulate the μEBW process [10, 12, 38] where the prime

[1]This chapter has been submitted for publishing as an article in Science and Technology for Welding and Joining

challenge is developing a suitable electron beam heat source geometry. This work, for the first time, formulates a theoretical model to represent the volumetric heat distribution of the electron beam, based on the electron penetration theory of Kanaya and Okayama [22].

Because the electrons penetrate the free surface of the material for a depth of a few microns, there is a radical difference between micro and macro electron beam welding. In μEBW, the electron penetration and the weld penetration are comparable [38]; so the incident beam is best approximated as a volumetric heat source. On the other hand, the effect of electron penetration is insignificant in conduction mode macro welding due to the large size of the weld as compared to the beam penetration. Three dimensional heat source models, however, are essential to analyze the keyhole mode macro welding where the heat penetration occurs as a result of high intensity heat source.

The three dimensional electron beam heat source models used for macro scale in the past are either empirical or semi-empirical. Goldak *et al.* [33] first developed a three dimensional double ellipsoidal heat source model, which was widely used in the analysis of conduction mode electron beam welding [39–41]. Later, the conical heat source model developed by Wu *et al.* [42] became popular in modeling of deep penetration electron beam welds. However, such models are not explicitly defined and depends on the feedback data from ad-hoc experiments, in the form of size and position of the ellipsoids and/or cones.

The heat source models used in studying μEBW until now are still in their early stages. Hwang and Na [12] modeled the energy input from the beam as heat generation in a specific volume of square cross section inside the solid. Similarly, Knorovsky *et al.* [10] considered heat generation in a cylindrical region of given radius and height inside a material within which the beam power is equally distributed. Both the studies did not account for variation of electron energy across the cross section of the beam or along its penetration. Recently, Gajapathi *et al.* [38] used an electron beam heat source model that considers exponential decay of electron energy along the depth of the material. The previous models do not account for a very important factor of electron beams: the maximum rate of energy deposition occurs below the free surface.

The behavior of electrons-solid interactions are best predicted using Monte Carlo simulations [43]. The variation of absorbed electron energy along the depth, as ob-

tained from the simulations, can be used to model the trend of electron energy decay using a polynomial best fit. Such an approach has been applied in several studies [44, 45]; however, using the technique requires to run new simulations each time the material properties and/or the configuration of the beam are changed. An analytical formula describing the electron decay trend, proposed by Schiller *et al.* [46], is reported to compare reasonably well with the Monte Carlo results for specific cases [44]. The formula has been widely applied in the heat source modeling of electron beam [47, 48]. However, the analytical model is very simplistic in nature and does not account for the influence of material atomic number (Z) or atomic mass (A) on the electron-solid interactions. None of the approaches discussed provides a general analytical expression indicating the influence of beam voltage (V), density (ρ), atomic mass, and atomic number of the material on the trend of electron energy decay.

In the present work, the Kanaya and Okayama electron penetration theory [22] is used to represent the electron energy deposition along the depth of the solid. The Kanaya-Okayama model is preferred over the previously discussed models because it accounts for the predominant physics of electron-solid interactions. Also, it provides a closed form expression which is reported to have a good agreement with the experimental results [22]. Using the Kanaya-Okayama theory, this study proposes for the first time an analytical method to determine the heating efficiency of the electron beam. Further, numerical simulations of μEBW are carried out using the Kanaya-Okayama heat source; the approach is similar to that developed by the authors in the past except they considered an exponential decay of the electron energy along the penetration [26, 38]. The current numerical model is validated by comparing the temperature field in two asymptotic cases, one in the region near the heat source and the other, far away from it. In the following sections, the effect of acceleration voltage at different beam traveling speeds is analyzed. The optimum acceleration voltage required to produce a given size of micro weld is obtained following the guidelines suggested by Gajapathi *et al.* [38]. The differences in the prediction of temperature distribution between the Kanaya-Okayama and the exponential decay heat source models are compared.

4.2 Mechanism of Electron Beam Heating

In an electron beam column, an electrostatic field accelerates the electrons to collide with the target material and transfer their kinetic energy. Not all of the incoming energy is converted into heat in the material during the interactions. Loss of the

incident beam energy is caused due to back scattered electrons, secondary electrons, x-ray generation, and electromagnetic radiation, as shown in Fig. 4.1. All the aforesaid processes can be explained by considering the two major classifications of the electronic collisions with the substrate [46, 49]:

1. Nuclear collisions (elastic scattering) are the collision of the incoming electrons with atomic nuclei of the substrate. The electrons are scattered through a large angle with almost the same energy as a result of momentum transfer. A deflection angle of 90^0 or more due to single or multiple nuclear collisions can cause the incoming electrons to completely inverse their path out of the body and result as backscattered electrons.

2. Electronic collisions (inelastic scattering) are the collisions which results in the energy transfer of the incoming electrons with a comparatively smaller deflection. Inelastic scattering of the electrons inside the material occurs by several mechanisms out of which only those significant in metal type solids are highlighted.

    - Plasmon excitation occurring due to free electron gas typically transfers 15 eV to the solid.
    - Emission of thermionic electrons owing to the temperature rise in the material is typically less than 1 eV, depending on the beam current and material properties.
    - Excitation of the conduction band evolves secondary electrons which usually carry 0-50 eV kinetic energies out of the surface.
    - X-rays produced consists of two components: characteristic radiation as the inner shell electron is replaced by the incoming electron, and Bremsstrahlung resulting from the deceleration of the primary electron in the columbic field of an atomic nucleus. X-radiation depend on the incident energy and atomic number of the material and are on the order of 1% or less.

The amount of energy attributed to each of the physical processes depicted in Fig. 4.1 depends both on the material properties and the electron beam acceleration voltage. Typically, the energy loss occurring due to secondary electrons, x-ray generation, and electromagnetic radiation are less than 0.5% of the incoming energy; back scattered electrons have the highest share, around 10-40% [46]. The remaining electron energy is transferred in to the substrate, gradually being absorbed with the depth. The fraction of electrons, that do not shed all their energy within a given

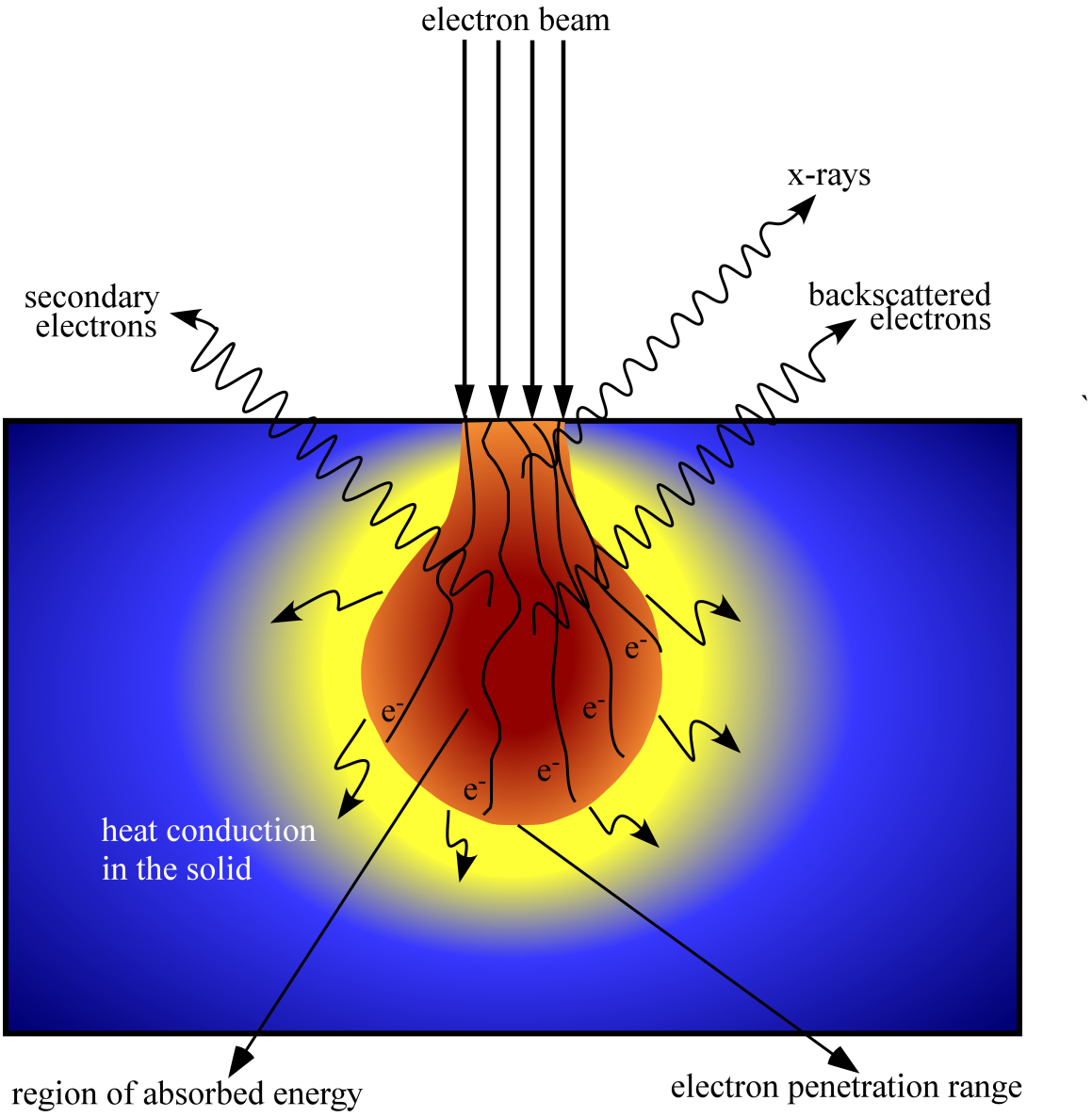

Figure 4.1 – Electron beam interactions with the solid

thickness of material and emerge out are called as transmitted electrons. The maximum electron penetration range (R) can be defined as the depth in the solid through which the electrons completely lose their incoming kinetic energy. It depends both on beam voltage and material properties, and can be expressed in the voltage range of 10 to 1000 keV, as [22]:

$$R = 2.76 \times 10^{-11} \frac{AV^{1.67}}{\rho Z^{0.889}} \tag{4.1}$$

where, R is given in cm; A, the atomic weight in g/mole; V, the beam voltage in V; Z, the atomic number; and ρ, the density in g cm^{-3}.

4.3 Heat Source Modeling

The modeling of the electron beam as a volumetric heat source requires describing the power distribution on the surface and energy decay along the penetration. While a circular Gaussian function is widely accepted to represent the variation of energy across the cross section of the beam, the thermal interactions of the electrons along the depth of the material is more complicated. One can represent the electron beam heating with the volumetric heat generation term, q as:

$$q = q_{max} \exp\left(-\frac{x^2+y^2}{2\sigma^2}\right) F(z) \tag{4.2}$$

where, q_{max} is the coefficient which represents maximum beam power absorbed per unit volume of the substrate, x, y, and z are coordinates along the beam motion, normal to the beam motion, and along the depth pointing from the target surface into the matter, respectively, and σ is the standard deviation of the Gaussian function. The standard deviation is related to the Full Width Half Maximum (FWHM) of the Gaussian function as follows: FWHM=$2\sqrt{2\ln 2}\sigma$=2.35σ.

The unknown function $F(z)$ can be derived by taking into account the physics of electron-solid interactions described in the previous section. It represents the trend of only the absorbed energy along the depth of the solid. An energy balance of the system helps to determine the total amount of energy absorbed within a given material depth by subtracting the transmitted fraction (electrons traveling beyond the depth considered) and back scattered fraction of the electrons from the incident energy. The effect of secondary electron, x-rays, and electromagnetic radiations can be ignored due to their negligible influence in the energy balance. Kanaya and Okayama obtained a theoretical expression for the fraction of absorbed energy as a function of depth, which can be written as [22]:

$$\begin{aligned}
\frac{E_A(z^*)}{E_0} &= 1-(1-z^*)^{3/5}\exp\left(-\frac{\gamma z^*}{1-z^*}\right) \\
&- \frac{E_B}{E_0}\left[\frac{6}{5}\int_0^{z^*}\frac{1.9\gamma}{(1-z^*)^{7/6}}\exp\left(-\frac{1.9\gamma z^*}{1-z^*}\right)dz^* \right. && (4.3)\\
&+ \left.\frac{6}{5\times 2^{5/6}}\left(1-\exp\left(-\frac{1.9\gamma z^*}{1-z^*}\right)\right)\right] && (4.4)
\end{aligned}$$

where, E_A (eV) is the absorbed electron energy within the distance z^*=z/R from the target material surface, E_B (eV) is the mean backscattered energy of the electrons, E_0 is the incident energy, γ is a constant which accounts for the effects of diffusion

loss due to the multiple collisions for returning electrons and energy retardation due to the electronic collisions.

The differentiation of the absorbed energy in Eq. (4.4) with respect to the depth provides the trend of its variation along the depth of the solid. The absorbed energy per unit depth, thus obtained, signifies the rate at which the electron transfers its energy to the material, also known as the stopping power, and can be written as [22]:

$$\begin{aligned}\frac{dE_A}{dz} &= \frac{E_0}{R}\left[\frac{1}{(1-z^*)^{2/5}}\exp\left(-\frac{\gamma z^*}{1-z^*}\right)\left(\frac{\gamma}{1-z^*}+\frac{3}{5}\right)\right. \\ &+ \left.\frac{E_B}{E_0}\frac{6\times 1.9}{5}\frac{\gamma}{(1-z^*)^2}\exp\left(-\frac{1.9\gamma z^*}{1-z^*}\right)\left(\frac{1}{2^{5/6}}-(1-z^*)^{5/6}\right)\right] \quad (4.5)\end{aligned}$$

The normalized energy distribution curve along the depth of the material, represented by the function F(z), is described by dividing the stopping power function in Eq. (4.5) by its maximum value, as:

$$F(z) = \frac{\frac{dE_A}{dz}}{\left(\frac{dE_A}{dz}\right)_{max}} \quad (4.6)$$

where, the peak value of the stopping power curve, $\left(\frac{dE_A}{dz}\right)_{max}$, can be found out with the knowledge of the depth (z_E) at which the maximum energy dissipation occurs. The following expression reported by Kanaya and Okayama can be used to determine z_E [22].

$$z_E = \frac{R\left(1+2\gamma-0.21\gamma^2\right)}{2\left(1+\gamma\right)^2} \quad (4.7)$$

The coefficient q_{max} in Eq. (4.2) can be described as the product of the maximum current flux (J_{max}) and the maximum absorbed electron energy per unit depth, and can be represented using the following expression.

$$q_{max} = J_{max} \times \left(\frac{dE_A}{dz}\right)_{max} \quad (4.8)$$

Also, the variation of the current flux (J) of the electron beam on the surface of the target is represented by a Gaussian distribution as:

$$J = J_{max}\exp(-\frac{x^2+y^2}{2\sigma^2}) \quad (4.9)$$

The total beam current, I, can be obtained by the area integration of the current flux.

$$I = \int_{-\infty}^{\infty}\int_{-\infty}^{\infty} J_{max}\exp(-\frac{x^2+y^2}{2\sigma^2})dxdy \quad (4.10)$$

The maximum beam current flux for a Gaussian distribution is:

$$J_{max} = \frac{I}{2\pi\sigma^2} \tag{4.11}$$

Using Eqs. (4.2), (4.7), and (4.8), the volumetric heat source term can now be written as:

$$q = J_{max} \exp(-\frac{x^2 + y^2}{2\sigma^2}) \times \frac{dE_A}{dz} \tag{4.12}$$

4.4 Heating Efficiency of the Electron Beam

The incoming energy of the electron is not entirely absorbed in the solid, to cause heating. The heating capability of the electron beam is characterized by a heating efficiency factor, η, which can be defined as the relative amount of power absorbed in the material. The absorbed beam power can be obtained by the volume integration of the heat source term in Eq. (4.12), which can be used to describe η as follows:

$$\eta = \frac{\int_{-\infty}^{\infty}\int_{-\infty}^{\infty}\int_{0}^{R} J_{max} \exp(-\frac{x^2+y^2}{2\sigma^2}) \times \frac{dE_A}{dz}\, dzdxdy}{VI} \tag{4.13}$$

On integrating Eq. 4.13, η can be written as:

$$\eta = \left(\frac{E_A}{E_0}\right) \tag{4.14}$$

where, E_A/E_0 represents the fraction of incident energy absorbed in the material. It is important to note here that the thickness of the materials in consideration is greater than the electron penetration range such that there is no loss of energy due to electron transmission. The total amount of absorbed energy can be obtained by integrating the stopping power in Eq. (4.5) through the depth until the electron penetration range. Numerical integration has been performed to solve for the definite integral as the antiderivative of the same is not obvious; a code based on the Simpson's method for numerical integration has been developed using the Fortran 77 programming language.

The two unknowns that are required to determine the heating efficiency values, as shown in Eq. (4.5), are γ and E_B/E_0. The constant γ is a function of atomic number of the material only and can be evaluated using the expression [22]: $\gamma = 0.187Z^{2/3}$. The mean backscattered energy fraction E_B/E_0 depends on both the target material

and incident energy; it can be evaluated using dedicated experiments for a given combination of material and incident energy [50–54]. A rigorous experimental procedure, however, can be avoided if the incident energy dependence of mean backscattered energy can be described as a function of atomic number. Sternglass [52] has observed that the mean backscattered energy obeys a linear trend with the increase in material atomic number irrespective of the incident energies between 0.2 and 32 keV. Kanaya and Okayama [22] compared different experimental findings of mean backscattered energy for materials having atomic number up to 100 and incident energies in the range of 2-70 keV. They have obtained a more generalized relationship describing the dependence of relative mean backscattered energy on the atomic number of the material only; the relationship curve can be approximated by the following second order polynomial best fit:

$$\left(\frac{E_B}{E_0}\right)_{K-O} = 0.613 + 0.003Z - 1.27 \times 10^{-5} Z^2 \tag{4.15}$$

The heating efficiency values are calculated as a continuous function of the material atomic number, as shown in Fig. 4.2, using the approximated relative mean backscattered energy values in Eq. (4.15).

It is desired to compare the present heating efficiencies against the experimental values to comment on the validity of the calculations. There has been lack of literature that presents the electron beam heating efficiency values directly for a given material and incident energy. However, the available data on backscattering phenomenon can be used to estimate the heating efficiency of the process, by re-writing the expression in Eq. (4.14) as follows: η=1-$\frac{I_B E_B}{I E_0}$, where, I_B/I is the relative backscattering current. Such a consideration is valid when the power loss due to other processes as a result of electron-solid interactions, except backscattering, is negligible.

For a normally incident beam, the relative backscattering current, also known as the backscattering coefficient, does not depend on the incident energy of the beam but varies with the properties of the target material [55, 56]. Archard [55] proposed the backscattering coefficient as a function of material atomic number only based on the composite theory of diffusion (valid for high atomic numbers) and elastic collisions (valid for low atomic numbers). A fourth order polynomial is used to best fit the relationship curve between the backscattering coefficient and material atomic number [55], which can be written as:

$$I_B/I = -0.012 + 0.017Z - 2.09 \times 10^{-4} Z^2 + 8.19 \times 10^{-7} Z^3 + 5.43 \times 10^{-10} Z^4 \tag{4.16}$$

Clearly, the backscattering coefficient can be calculated based on the atomic number

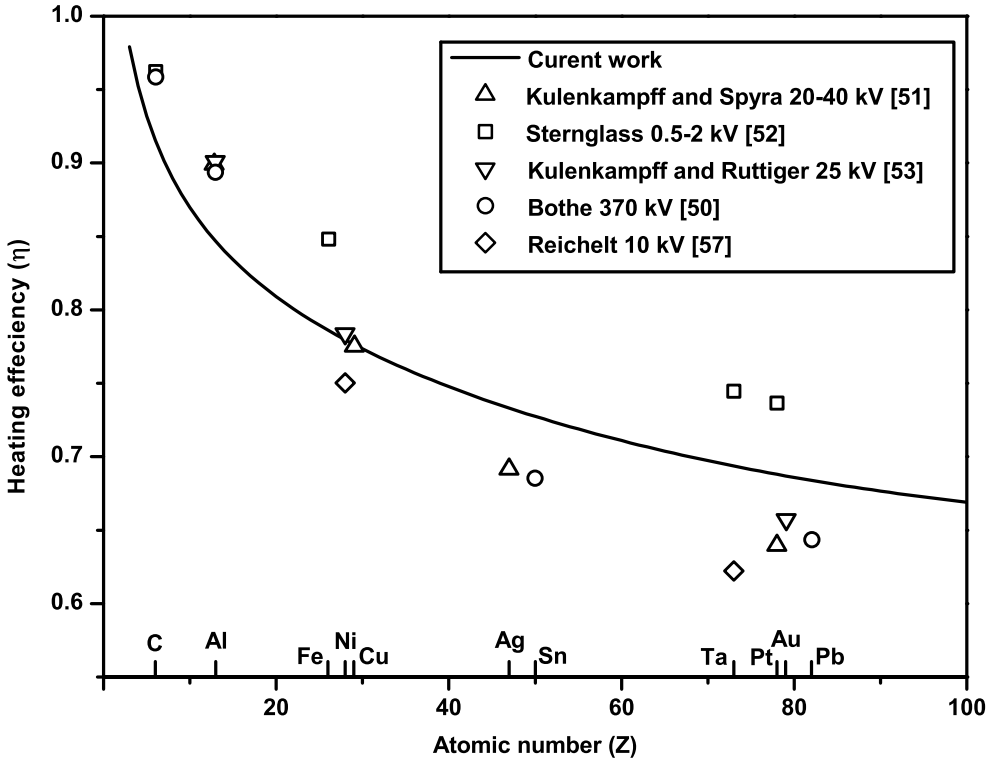

Figure 4.2 – Heating efficiency of the normally incident electron beam as a function of the atomic number of the irradiated material. The curve provides a good approximation independent of the beam incident energy in the range of 10-1000 keV

of target material using Eq. (4.16) irrespective of the beam incident energy.

To calculate the relative backscattering power loss and hence the heating efficiency, the relative backscattered current needs to be multiplied with the mean relative backscattered voltage (backscattered energy). The mean relative backscattered energy values have been obtained from literature [50–54] for different combinations of target material and incident energy. For a given material, the product of the backscattered coefficient and the mean values of relative backscattered energy provides the relative backscattering power loss. Direct experimental measurements of the backscattering power loss have also been reported by Reichelt [57] for nickel and tantalum at 10 keV incident energy. The heating efficiency is then calculated by subtracting the relative backscattering power loss from the whole. The experimental results of heating efficiency for specific materials are compared against the current

findings, in Fig. 4.2. The present calculations of the electron beam heating efficiency conform the experimental findings within the margin of 0-10%, for a wide range of incident energies and materials.

4.4.1 Effect of Voltage on Heating Efficiency

In this study, the heating efficiency is expressed as a function of material atomic number only. It would be reasonable to expect acceleration voltage to also play a role. The validity of the approximations made in the current study is discussed in this section by comparing the present calculation with the experimental values.

Figure 4.3 illustrates the experimental results of mean backscattered energy normalized by the approximate values obtained using Eq. (4.15). The horizontal axis represents the incident energy of the beam. It is observed that there is no clear dependence of the mean backscattered energy on the incident energy of the beam in the range of 10-1000 keV; however, the mean backscattered energy seems to be increasing with the increase in incident energy at lower levels (less than 10 keV). Also, the difference in experimental conditions contribute largely to the mean backscattered energy measurements [58]. For example, there is a considerable amount of difference in the relative mean backscattered energy values reported separately by Kulenkampff and Spyra [51] and Niedrig [54] for copper (Z 29) in the incident energy range of 20-40 keV, as seen in Fig. 4.3.

The dependence of backscattered energy on the incident energy is rather complex. The experimental conditions have seemingly larger impact on the backscattered energy measurements as compared to the incident energy by itself. In such a situation, the heating efficiency values proposed in this study as a function of material atomic number only provide an approximate estimation for many practical applications.

4.5 Application to Modeling of μEBW

In μEBW, an electron beam is used to track the line of joining between the materials. A simplified representation of the process is shown in Fig. 4.4, where the heat source travels at speed U along the centerline. The shape of the heat distribution on the surface and along the penetration of the electron beam heat source is also pointed out in the same figure. The temperature field in the solid during the process can be obtained by solving the heat conduction equation.

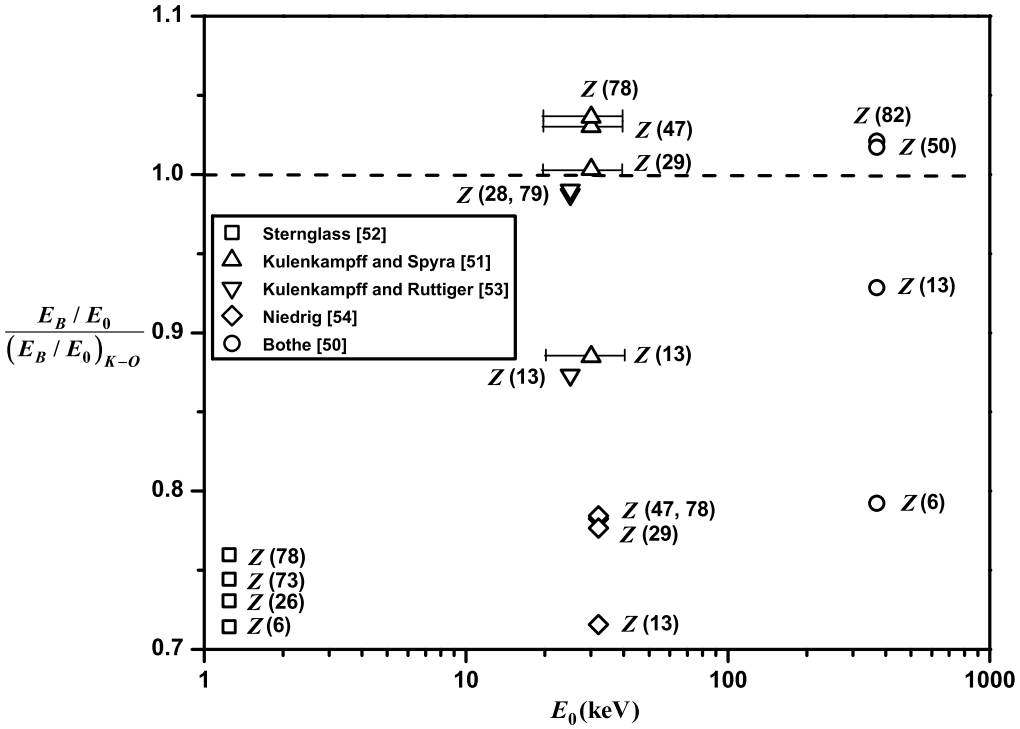

Figure 4.3 – Ratio of experimental relative mean backscattered energy to the values given by Eq. (4.15) is plotted against the beam incident energy for several material atomic numbers. There is no clear pattern observed of the backscattered energy variation with the beam incident energy.

At small scales, special considerations might be necessary to model heat conduction. The hypothesis of continuum is still valid at the micron scale considered in the present study. For scales approaching nanometers, heat transfer occurs quite differently and a different phenomenological understanding of the heat conduction is required to formulate the problem. Heat conduction in solids is described as the transport of energy by electrons and phonons, where the two carry the heat in different manners. Electrons play a major role in conduction in solids where as phonons are the only source of conduction in insulators [59]. In the present problem, the electrons from the beam transfer their momentum and energy to the electrons in the substrate. In summary, the energy from the incoming electrons is used to heat the electrons in the body, which is then distributed (conducted away) by the interactions between

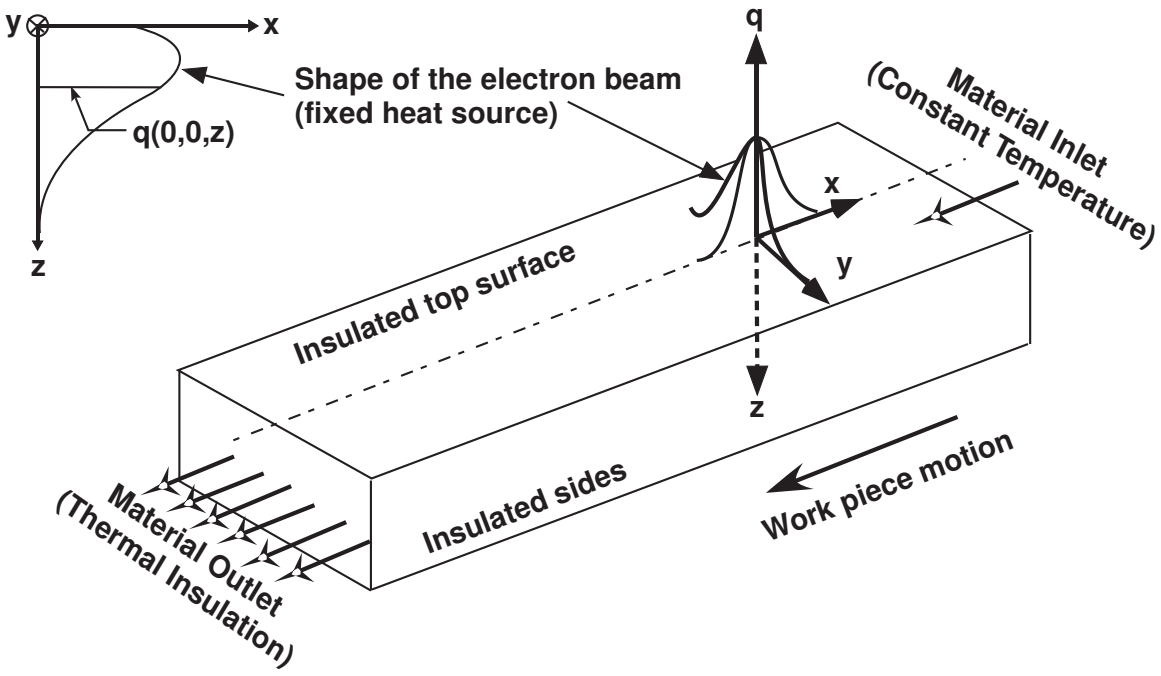

Figure 4.4 – Schematic of the model showing the brick shaped solid, trend of heat distribution of the electron beam that travels over the solid, and the pertinent boundary conditions valid in a moving reference frame

these electrons and the phonons.

The conduction through electrons and phonons are to be dealt with separately if the length scales of the substance and the "residence time" of the heat source are on the order of the mean free path and the mean free time of these energy carriers. The mean free path is defined as the distance between two successive collisions and the mean free time is the time of rest between the two collisions. Electrons have mean free path less than a few nanometers and mean free time on the order of femtoseconds depending on the energies of the electrons. On the other hand, the mean free path of the phonons range from nanometers to micrometers and the mean free time is on the order of picoseconds to nanoseconds depending on the temperature [59]. The length scales involved in the present research are much larger than $100nm$ and the weld speeds are not high enough to cross the residence time limits of nanoseconds; hence, the study of ballisitc behavior of electrons is not important here. Moreover, the high temperatures involved in welding is expected to further decrease the mean free path of electrons and phonons. Hence, the heat conduction can be assumed diffusive and the macroscopic Fourier heat conduction is valid. Nevertheless, the applicability of such a model for nanowelding or joining semiconductor materials, where electrons

and phonons play equal role in energy transport, requires developing of appropriate nano scale heat transport models.

The governing heat conduction equation in a coordinate frame attached to the moving heat source and the boundary conditions representative of semi-infinite solid are described by the authors in their previous work [26, 38]. The FWHM of the Gaussian function, representing the power density distribution on the target surface, is considered as the beam diameter (d). The other important physical processes occurring during welding such as melting, evaporation, and effect of temperature dependent thermophysical properties of the material are outside the focus of the current study.

4.6 Numerical Analysis

The numerical model of μEBW in this analysis is similar to that developed earlier [26, 38], in which the exponential decay heat source model has been replaced by the Kanaya-Okayama heat source model of the present work. Finite element based numerical package, COMSOL Multiphysics^{TM}, is used to solve the Fourier heat equation in moving coordinate system; where, the heat generation term represents the volumetric heating due to the electron beam impingement, as shown in Eq. (4.12). It is important to note here that the heat distribution function along the z coordinate, as shown explicitly in Eq. (4.5), is defined within the electron penetration range R; it has a mathematical singularity at $z = R$ which, in this study, is dealt with using the Heaviside step function. The computational domain here is only one-half of the brick shaped geometry, shown in Fig. 4.4, owing to the symmetry of the practical situation along the centerline. Meshing of the sub-domain is carried out following the guidelines reported previously [26]. Figure 4.5 depicts a typical grid used in the current analysis. The numerical solution is obtained for the choice of constant properties of silicon, shown in Table 4.1, as an example.

4.7 Validation of the Numerical Model

The fact that the volumetric heat source, when concentrated, can be compared to a point heat source, permits the validation of the current numerical model against the well-known point heat source solution developed by Rosenthal [28]. Rosenthal's solution, however, cannot be used to predict the temperature field near the heat source as the temperature rises to infinity at its center. The temperature profile under

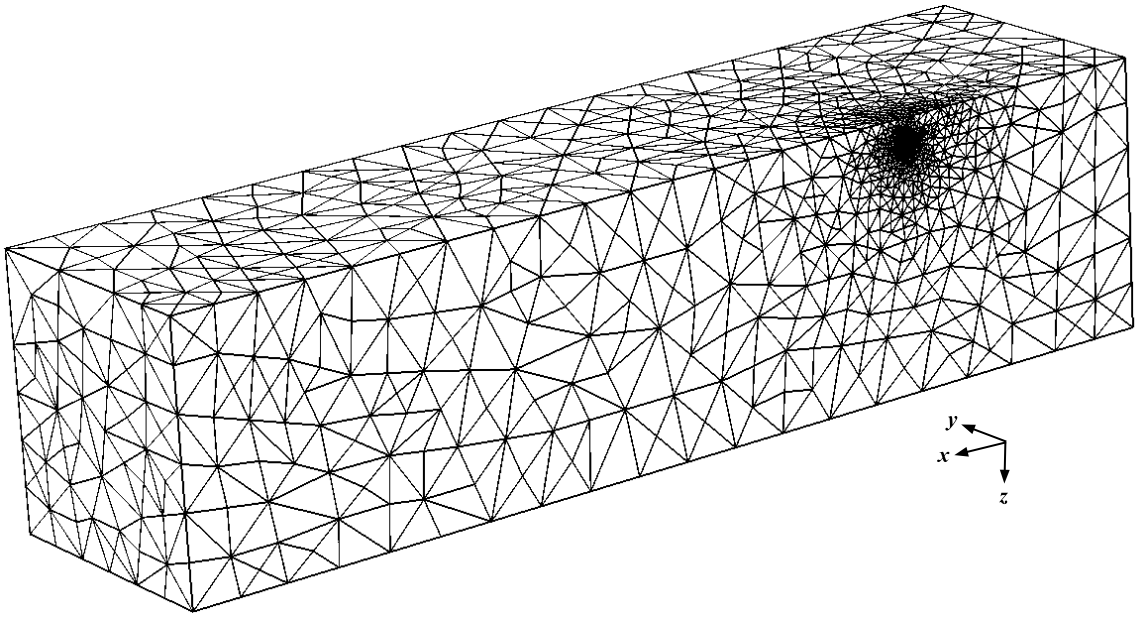

Figure 4.5 – Computational domain meshed with non-uniform tetrahedral elements

Table 4.1 – Properties for silicon at 27^0C [36]

Properties	Symbol	Values	Units
Thermal conductivity	k	148	[W m^{-1} K^{-1}]
Density	ρ	2330	[kg m^{-3}]
Specific heat	c_p	712	[J kg^{-1} K^{-1}]
Thermal diffusivity	α	8.92×10^{-5}	[m^2 s^{-1}]
Melting temperature	T_m	1412	[^{0}C]
Initial temperature	T_0	27	[^{0}C]
Atomic mass	A	28	[g mol^{-1}]
Atomic number	Z	14	

the beam can be analyzed by solving for the heat equation ignoring conduction, as proposed by Gajapathi *et al.* [38].

4.7.1 Far-Field Temperature

The temperature field in a semi-infinite solid of constant properties due to the heat conduction from moving point heat sources is provided by Rosenthal [28], as:

$$T - T_0 = \frac{W}{2\pi kr} \exp\left(\frac{-Ux}{2\alpha}\right) \exp\left(\frac{-Ur}{2\alpha}\right) \tag{4.17}$$

where, T is the temperature at any point in the solid and r represents the distance from the heat source.

To represent the volumetric heat source of the present model as a point heat source, the beam diameter and the maximum electron penetration range are chosen as 0.2 μm and 0.1 μm, respectively in Eq. (4.12). Meshing the sub-domain to solve for point heat sources is a challenging task; the meshing procedure outlined by the authors in their previous μEBW model is followed [38]. For comparing with the analytical solution, the beam power and the beam traveling speed are kept constant at 10 W and 450 m s^{-1} respectively, and the properties of silicon shown in Table 4.1 are used.

The numerical solution obtained using such a modified volumetric heat source is compared to the analytical temperature field in Eq. (4.17); the variation of temperature along the centerline on the surface of the solid is compared in Fig. 4.6. The break in the continuous line at the center of the heat source in Fig. 4.4, shows the infinite rise in temperature of the Rosenthal's solution in Eq. (4.17). The temperature field obtained using the numerical approach, represented as black dots in the same figure, shows good agreement with the analytical solution.

4.7.2 Asymptotic Case of Fast Moving Heat Source

The temperature profile produced in the solid near the three dimensional distributed heat source can be derived analytically for the asymptotic case, where heat conduction is neglected in all the directions. In the absence of any heat diffusion, the temperature distribution obtained at any given point in the solid is its highest possible value, for a given set of welding parameters and material properties. The maximum temperature in the body is obtained under the beam at the depth of maximum electron energy dissipation, z_E and it varies as the beam moves along the surface. The variation of the asymptotic maximum temperature as a function of x coordinate, T_{sc}, can be derived using the guidelines [27, 38], as:

$$T_{sc} = T_0 + \frac{T_{p,max} - T_0}{2}\left[1 + \text{erf}\left(\frac{x^*}{\sqrt{2}}\right)\right] \tag{4.18}$$

where, $T_{p,max}$ is the highest possible temperature attained in the material as a result of a given process, which will be referred as the process peak temperature from hereupon. The process peak temperature for the Kanaya-Okayama heat source model can be

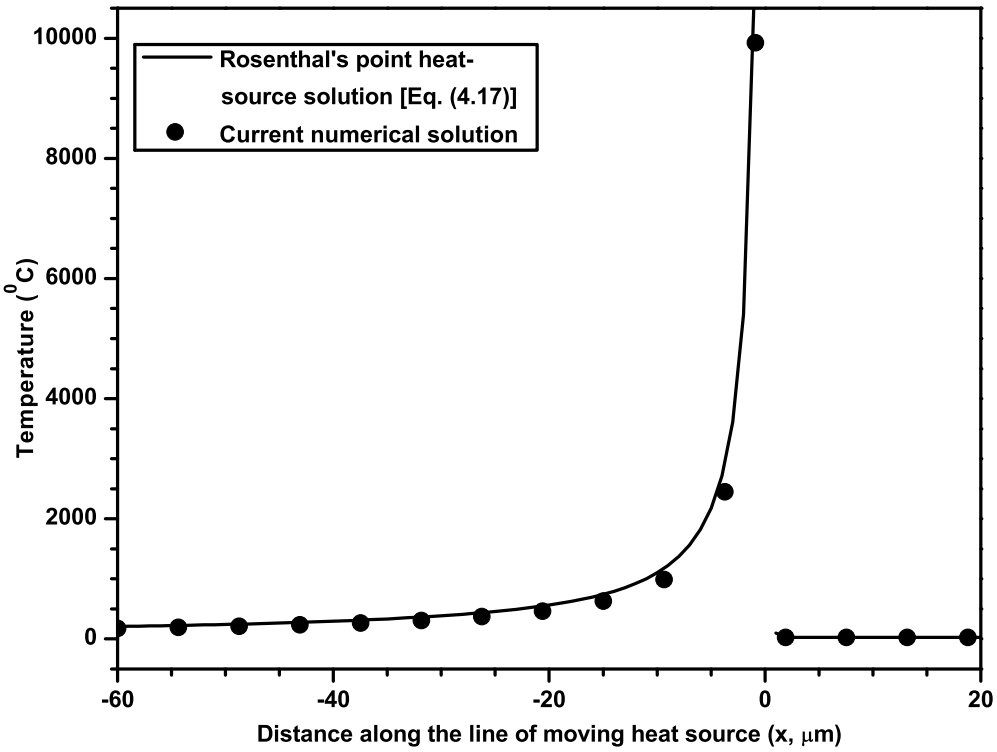

Figure 4.6 – Temperature variation along the centerline of the solid is compared between Rosenthal's point heat source solution and the current numerical model for W=10 W, U=500 m s^{-1}, k=148 W m^{-1} K^{-1}, d=0.2μm, and R=0.1 μm

derived following the approach reported previously [38], as:

$$T_{p,max} = T_0 + \frac{\sqrt{2\pi} J_{max} \left(\frac{dE_A}{dz}\right)_{max} \sigma}{\rho c_p U} \tag{4.19}$$

The temperature field near the heat source can be obtained numerically for the asymptotic case by considering an artificially low thermal conductivity of the material [27, 38]. A value of k=0.01 W m^{-1} K^{-1} is chosen in this study so that the temperature field reaches its asymptotic maximum and does not rise further with any decrease in thermal conductivity. In heat conduction study, the Peclet number (Pe) is used to measure the significance of heat diffusion in a process and can be written as:

$$Pe = \frac{Ud}{\alpha} \tag{4.20}$$

The Pe for the current model with negligible conduction is found to be 1.6×10^4. Typically, Pe of 10 is sufficient to overcome the heat diffusion along the axial direction [34]. However, the very large Pe obtained for the fast moving heat source can be attributed to limiting the heat diffusion along the penetration and lateral directions as well.

The variation of maximum temperature along the centerline at the depth of maximum electron energy dissipation is compared between the analytical solution in Eq. (4.18) and the numerical model with higher Pe value, as shown in Fig. 4.7; a good agreement is found between the two. Due to the absence of heat conduction during the process, the maximum temperature rises until the process peak temperature and does not fall, as the beam moves over the solid.

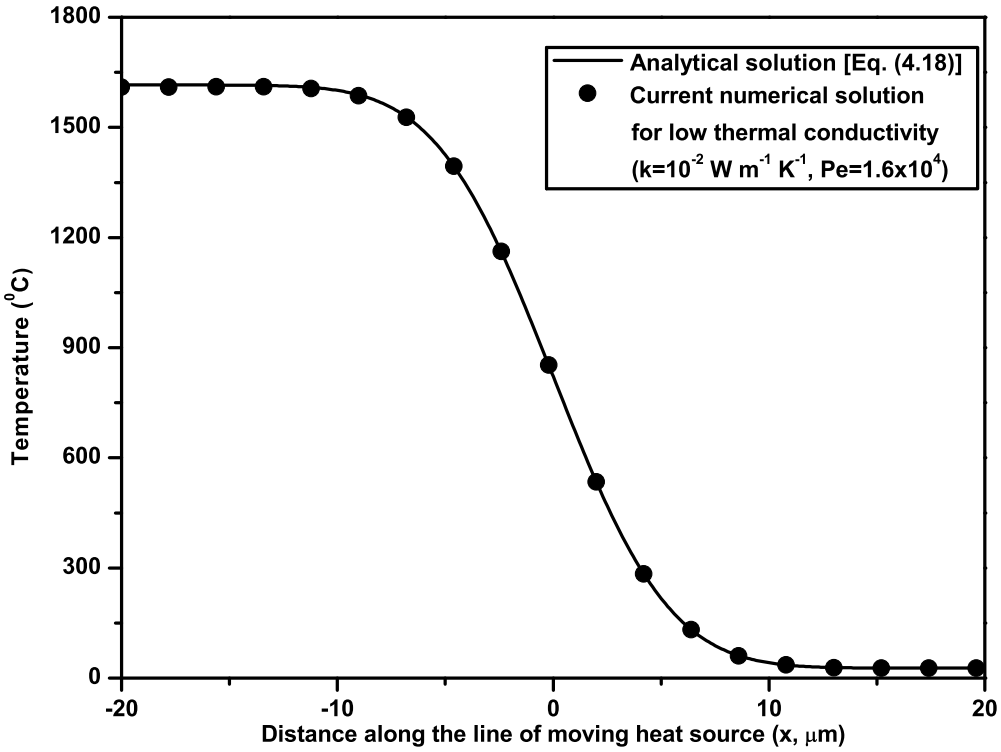

Figure 4.7 – Temperature variation along the centerline of the solid ignoring conduction is compared between the analytical solution in Eq. (4.18) and the current numerical model for W=10 W, k=0.01 W m^{-1} K^{-1}, and Pe=1.6×10^4

4.8 Influence of Welding Parameters on μEBW

An ideal μEBW process means that the welding parameters, such as beam voltage, current, beam diameter, and beam traveling speed, selected for the process are optimal; the criteria to select the aforementioned parameters has been laid down by the authors previously [38]. Of all the parameters, the most significant ones are the beam voltage which governs the beam penetration (R) relative to the maximum melting depth (z_m) and the beam travel speed represented by Pe of the process. The behavior of Kanaya-Okayama heat source model in μEBW is evaluated in this study for different choices of welding parameters.

4.8.1 Effect of Beam Voltage and Beam Traveling Speed on the Temperature Rise

Due to the nature of the electron energy dissipation along the depth, the maximum of the incoming energy can be deposited on the surface or further underneath, depending on the amount of beam penetration. The process peak temperature, however, can be at the same location as the maximum energy dissipation or shift nearer to the surface based on how fast the heat is diffused in the solid. For a heat diffusion dominated process having a low Pe, the behavior of the electrons in the solid is secondary and the process peak temperature exists on the surface. On the other hand, for a high Pe process as the electron-solid interactions play a major role in flow of heat, the process peak temperature shifts below the surface. The effect of beam voltage (beam penetration) and Pe of the process on the surface maximum temperature, represented as $T_{s,max}$, and process peak temperature ($T_{p,max}$) is shown in Fig. 4.8; where, Figs. 4.8(a), 4.8(b), and 4.8(c) show the processes with Pe=100, 10, and 1, respectively. Also, the beam current and the beam diameter are kept unchanged at 1.5 mA and 10 μm, respectively for all the processes.

In Figs. 4.8(a) and 4.8(b), it is observed that both the $T_{s,max}$ and the $T_{p,max}$ decreases with the increase in beam voltage. Although higher voltages results in higher beam power, the decreasing trend in temperatures is due to the larger electron-solid interaction volume within which the input power is distributed. Such a theory of explaining heating of the solid only by the thermal interaction of the electrons, without accounting for heat diffusion, is valid only for the cases of high Pe. At lower Pe of 1 as shown in Fig. 4.8(c), the temperatures increase initially for lower beam voltages (20-40 kV), which can be attributed to both the factors of low beam penetration and

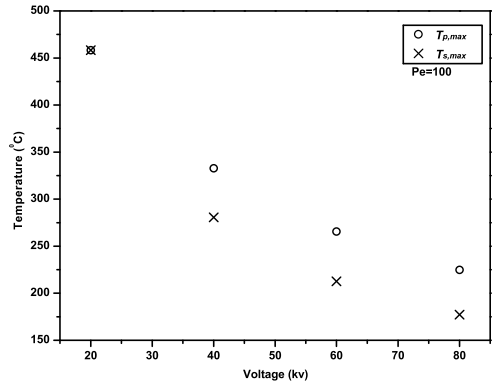

(a)

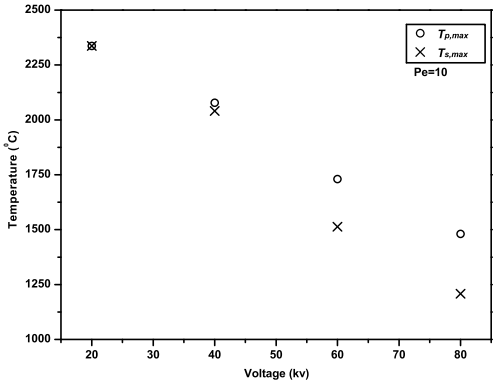

(b)

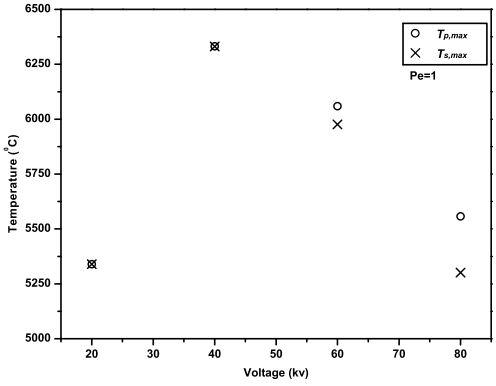

(c)

Figure 4.8 – Effect of voltage on surface maximum temperature ($T_{s,max}$) and process peak temperature ($T_{p,max}$) at (a) Pe=100, (b) Pe=10, and (c) Pe=1

high rate of diffusion. The increase in input power due to the increase in beam voltage causes the rise in temperatures in the range of 20-40 kV. As the beam voltage is further increased, the electron interaction volume increases out of proportion with the beam power. Hence, the decreasing trend in both $T_{s,max}$ and the $T_{p,max}$ is observed in the voltage range of 40kV to 80kV in Fig. 4.8(c).

At lower beam voltages, the electron beam having a very low penetration depth acts as a surface heating source. This is evident as the $T_{s,max}$ and the $T_{p,max}$ values coincide for 20 kV beam voltage for all the three cases of Pe=100, 10 and 1 as shown in Fig. 4.8. As the voltage increases, the beam penetration also increases and the peak of electron energy deposition curve along the depth shifts farther below the surface. The $T_{p,max}$, which is obtained at the depth of maximum energy deposition, is higher than the $T_{s,max}$ on the surface. With the increase in beam voltage, the amount of energy deposited on the target surface decreases comparatively, which leads to a larger difference between $T_{s,max}$ and $T_{p,max}$, as seen in Fig. 4.8. For the low heat diffusion processes (Pe=100) as seen in Fig. 4.8(a), the energy transfer due to the electron interactions play a major role. Therefore, the values of $T_{p,max}$ are distinct than $T_{s,max}$ even at smaller beam voltage of 40 kV. The increase in the significance of heat diffusion as Pe decreases from 100 to 1 is the reason behind the relative decrease in the difference between the $T_{p,max}$ and $T_{s,max}$ at 40 kV voltage in Figs.4.8(a), 4.8(b), and 4.8(c).

A significant variation in the values of both the $T_{p,max}$ and $T_{s,max}$ is noticed between the three different cases of Pe=100, 10 and 1 in Fig. 4.8, although the amount of power supplied is constant at a given beam voltage. At higher Pe, the beam residence time relative to the thermal diffusion time is very small. As a result, the effective amount of energy supplied to the solid by an electron beam of constant power, is smaller for a high Pe process as compared to a lower Pe process. Hence, the higher temperature ranges for low Pe process in Fig. 4.8 can be attributed to the higher energy input.

4.8.2 Determining Optimal Beam Voltage and Beam Traveling Speed

The optimum electron beam voltage and Pe desired to obtain a micro weld of given melting depth is decided by selecting the process with least heat input [38]. The heat input in welding can be defined as the relative amount of energy supplied per unit

length of the weld [37]: HI=VI/U. The beam voltage of the process is varied to obtain different electron penetrations (R) and the beam current is adjusted suitably so that the maximum melting depth (z_m) of all the processes remains constant at 2.5 μm. The heat input of such processes are compared at three different beam traveling speeds corresponding to Pe=10, 100, and 300 in Fig. 4.9. The higher heat input values for the processes having Pe=10 is because large amount of heat is being quickly diffused outside the weld region. The electron interactions and hence the increase in electron range are secondary in such heat diffusion dominated processes due to which the heat input curve is close to being straight. There is a significant drop in the heat input curve as the Pe of the process is increased to 100. Also, it is observed that the heat input is minimum corresponding to the relative electron penetration range of R/z_m=2. The high heat input requirements for smaller electron penetrations (R/z_m <2) can be attributed to the large dependence on heat conduction to propagate the electron energy till the melting depth, where as, at larger electron penetrations (R/z_m >2), high energy electrons travel beyond the melting depth, causing unwanted heating of the additional material volume.

The increase in Pe of the process beyond 100 results in the heat transfer having greater dependence on the electron interactions as compared to the heat conduction. At high Pe of 300, smaller electron penetrations (R/z_m <1.2) are considered disadvantageous as they result in further increase in the heat input, as seen in Fig. 4.9. However, larger electron penetrations at high Pe can produce welds of similar length and depth (but not the width) at a lower heat input. In Fig. 4.9, the cross sections of two welds having the same electron penetration range and maximum melting depth (A corresponds to the process with Pe=100 and B corresponds to that of Pe=300) are shown. The weld width corresponding to the process with Pe=300 is observed to be smaller as compared to that of Pe=100. The larger weld width obtained from a process with Pe=100 and relative electron penetration range of R/z_m=2 can be considered suitable for practical applications, at the marginal expense of the heat input as compared to higher Pe processes.

4.9 Comparison with the Previous μEBW Model

4.9.1 Temperature Distribution in the Material

The temperature field in the material as a result of μEBW depends on the heat penetration characteristics of the electron beam and also on the Pe of the process. The

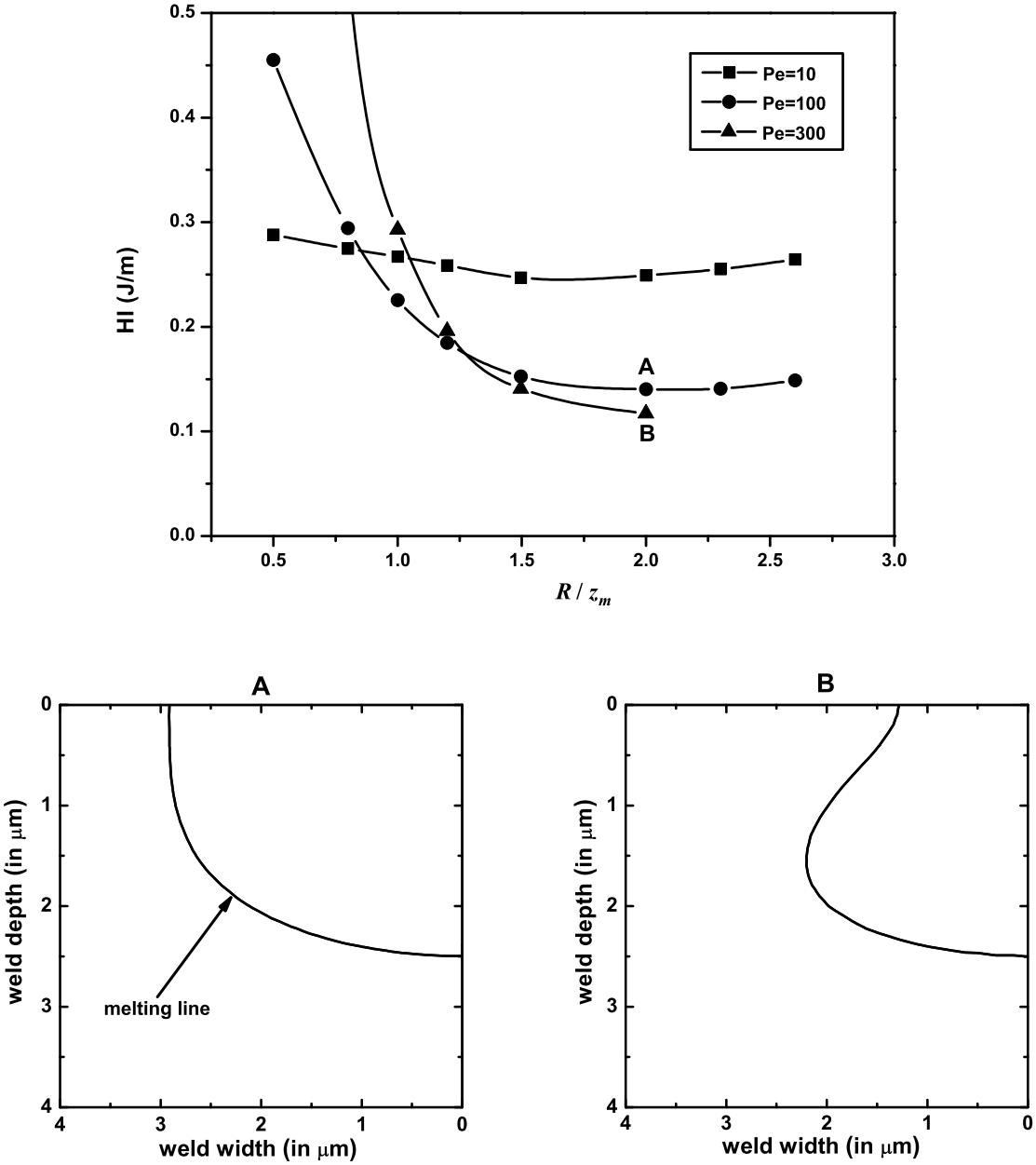

Figure 4.9 – Variation of heat input with the relative electron penetration range for three different Pe processes of 10, 100, and 300. The weld cross sections having the same weld depth of 2.5 μm are shown for the specific processes marked as A and B

exponential decay heat source model and the Kanaya-Okayama heat source model are compared in Figs. 4.10(a) and 4.10(b) for the same electron penetration range and maximum melting depth; where, the variation of the maximum temperature along the depth is shown at three different Pe of 1, 100, and 1000. Along the vertical axis

of the plot, the temperature excess of the initial condition is normalized with respect to the melting temperature gradient and the depth of the solid is represented on the horizontal axis by normalizing it with respect to the maximum electron penetration range. Numerical simulations have been carried out separately for both the heat source models at different Pe; the beam voltage corresponds to electron penetration range R=5 μm and the material properties of silicon in Table 4.1 are used. The maximum melting depth of all the processes is kept constant at 2.5 μm; the beam current needs to be varied to ensure that the processes with different Pe produce the same melting depth. The beam diameter remains unchanged at 10 μm and the choice of beam velocity depends on the Pe of the process.

For a process with constant Pe, it is observed that the Kanaya-Okayama heat source model produces lower temperature along the depth of the material compared to the exponential decay heat source model, as seen in Fig. 4.10. This can be attributed to the difference in electron energy decay behavior of the two models. For the high Pe process of 1000, the Kanaya-Okayama heat source model produces the peak temperature underneath the surface which leads to a more uniform temperature distribution in the weld region. The exponential decay heat source model, due to its inherent characteristics of depositing the maximum of its incoming energy on the surface, results in a very high temperature gradient, at high Pe.

4.9.2 Maximum Temperature On the Surface

The maximum temperature at the weld surface for the processes with different Pe is compared between the Kanaya-Okayama heat source model and the exponential decay heat source model in Fig. 4.11; where, the maximum melting depth is kept constant at 2.5 μm. The beam voltage is chosen such that the electron penetration range is twice the melting depth. The material properties of silicon in Table 4.1 are used for the numerical simulations. It is observed in Fig. 4.11 that the maximum temperature of the process corresponding to the Kanaya-Okayama heat source model is smaller in the entire regime of Pe as compared to the exponential decay heat source model. This is because the maximum energy dissipation in the Kanaya-Okayama heat source model occurs underneath the surface, leading to less heating of the surface. The difference in maximum temperatures between the two heat source models becomes more prominent at higher Pe, as seen in Fig. 4.10, as the significance of heat diffusion decreases.

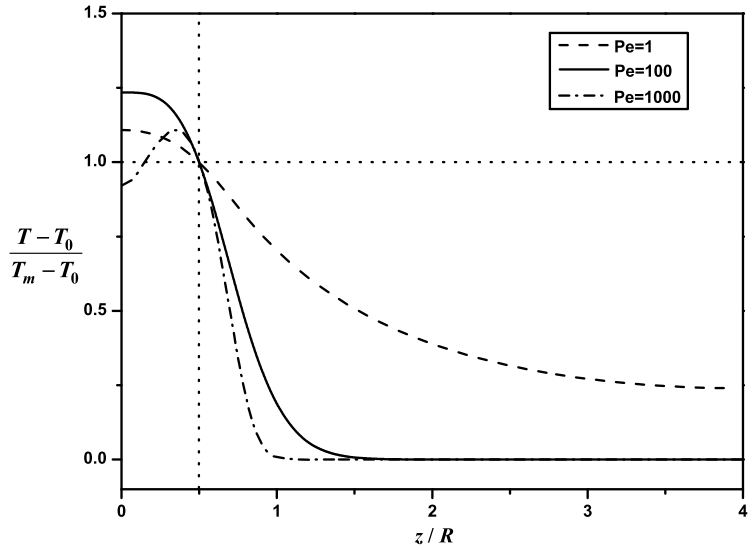

(a)

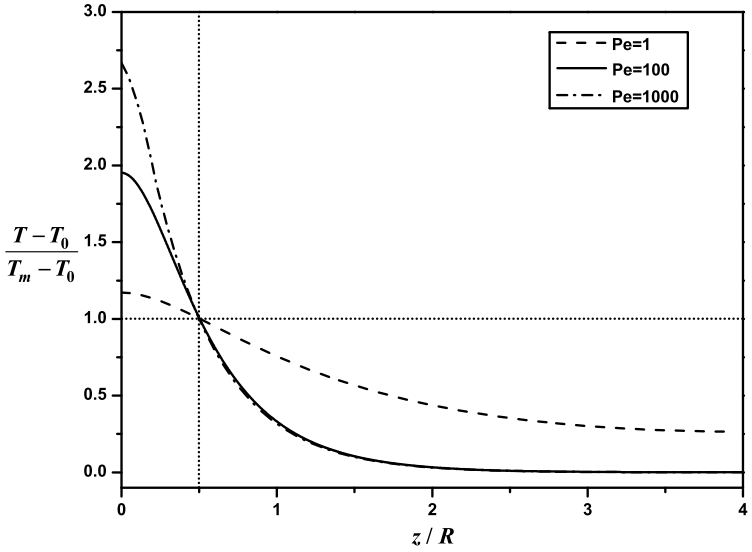

(b)

Figure 4.10 – Variation of normalised maximum temperature along the depth in the non-dimensional form for processes with Pe=1, 100, and 1000 is compared between (a) Kanaya-Okayama heat source model and (b) exponential decay heat source model. The melting depth is kept constant at 2.5 μm and the relative beam penetration is 2.

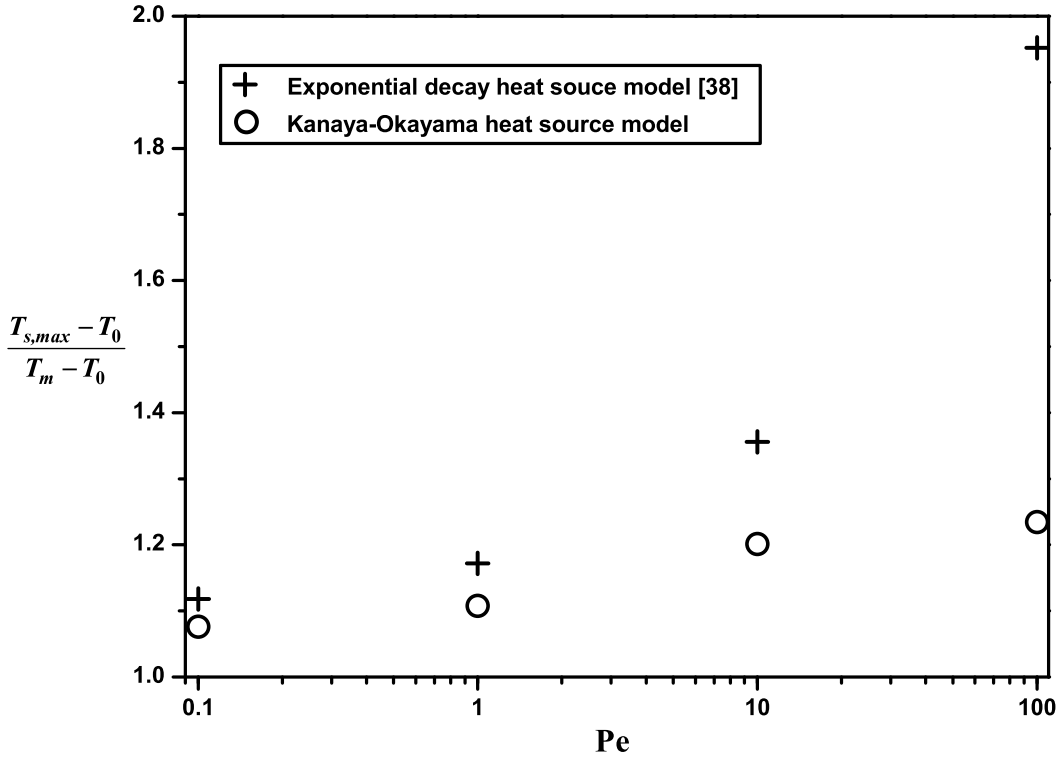

Figure 4.11 – The effect of Pe on the normalised surface maximum temperature is compared between the Kanaya-Okayama heat source model and the exponential decay heat source model. The maximum melting depth is constant at 2.5 μm and the electron penetration range is twice the melting depth for all the processes

4.10 Discussion

The mathematical model of electron-solid interactions in the range of 10-1000 keV incident energy used in this study accounts only for the predominant physics of backscattering, absorption, and transmission of electrons [22]. The other processes occurring simultaneously such as emission of secondary electron and x-rays also influence the energy decay behavior of electrons in the solid and its heating efficiency, although such effects can be neglected in most cases.

The simplified approach in this study of expressing the electron heating efficiency as a function of atomic number only is based on describing the incident energy dependence of heating efficiency as a function of atomic number. Avoiding such approximations would require to assemble large amount of experimental data of mean

backscattered energy for different incident energy beams and target materials. The collected data can then be arranged in a plot of relative mean backscattered energy against the incident energy of the beam (similar to Fig. 4.3). Advanced statistical methods should be used to best fit all the available data for a given material atomic number. Such a practice would allow to obtain the closest relative mean backscattered energy based on the incident energy of the beam and atomic number of the material, which can be used in the proposed analytical approach to improve the heating efficiency estimations.

The optimum welding parameters determined using the current Kanaya-Okayama heat source model match the previous predictions obtained using the exponential decay heat source model in μEBW. A Pe of 100 has been reported as ideal by both the models. Also, the optimal effective electron penetration in the previous model is reported as 0.8-1.2 times the maximum melting depth [38]; for which, the equivalent relative electron penetration range (R/z_m) can be calculated as 1.8-2.8. In this work, the optimal electron penetration range is obtained as twice the maximum melting depth, which falls in the range reported earlier.

Previous study of μEBW using the exponential decay heat source model showed that the volumetric heating source produces lower weld surface temperatures as compared to the surface heating sources [38]. The present study using the Kanaya-Okayama heat source model confirms this finding and further suggests that the surface temperature falls even lower as the peak of the incoming electron energy deposition occurs underneath the surface. Hence, the electron beam can be used at very high heat intensity levels that are necessary to carry out microwelding, as opposed to the surface heating sources such as laser beams which results in excessive ablation.

4.11 Conclusions

In this work, a volumetric heat source model has been developed to represent an electron beam as a heat source using the Kanaya and Okayama electron penetration theory. A theoretical approach has been proposed, for the first time, to calculate the heating efficiency of a normally incident electron beam. The heating efficiency values obtained as a function of only material atomic number provides an average estimate for a wide range of beam incident energies.

The Kanaya-Okayama heat source model, which closely represents the practical

situation, is used in the numerical study of μEBW. The numerical model has allowed to predict the temperature distribution in the solid for different choices of beam traveling speed and acceleration voltage. The peak temperature of the process is found to increasingly shift below the target surface for higher beam penetrations and Pe. As a result, lower weld surface temperatures and smaller temperature gradients across the molten region persist. However, increasing the beam penetration and Pe beyond a limit provides no meaningful advantage, for a required size of the weld. The optimum relative beam penetration and Pe are determined to be 2 and 100, respectively based on the minimum heat input of the process.

The optimum welding parameters of μEBW obtained using the Kanaya-Okayama heat source model are found similar to those predicted previously using the exponential decay heat source model. The temperature distribution in the solid, as predicted by the two models, are compared for the choice of optimum welding parameters and given size of the weld. It has been observed that the temperature gradient in the molten region and maximum temperature obtained at the weld surface using the Kanaya-Okayama heat source model are lower than the exponential decay heat source model at any given Pe.

Calculations confirm that it is possible to carry out μEBW in situations considered impossible for lasers.

Chapter 5

Modeling of Phase Change in μEBW and Proposing Experimental Parameters

This chapter deals with the mathematical modeling of melting and evaporation phenomena and incorporating them into the previously developed numerical model of μEBW. The effect of evaporation on the microwelding is discussed. Further, the numerical model is used to propose proof of concept microwelding experiments based on the hypothesis developed in Chapter 4. The weld shape expected according to the numerical model is shown which needs to be verified by the experimental observations.

5.1 Mathematical Modeling of Phase Transition in μEBW

5.1.1 Melting

The melting phenomenon can be modeled by accounting for the latent heat of melting in the Fourier heat conduction equation. The governing equation in moving coordinate system can be written as:

$$\frac{\partial}{\partial x}\left(k_m \frac{\partial T}{\partial x}\right) + \frac{\partial}{\partial y}\left(k_m \frac{\partial T}{\partial y}\right) + \frac{\partial}{\partial z}\left(k_m \frac{\partial T}{\partial z}\right) + q + \rho_m c_{p_m} U \frac{\partial T}{\partial x} = 0 \tag{5.1}$$

where k_m, ρ_m, and c_{p_m} are the modified thermophysical properties of the material to account for the phase transition from solid to liquid. The thermal conductivity(k_m) and density (ρ_m) of the material are defined such that they behave differently for solid state and liquid state. The knowledge of solid fraction (f_s) and liquid fraction (f_l) at any spatial location in the material can be used to define the properties as:

$$k_m = f_s k_s + f_l k_l; \qquad \rho_m = f_s \rho_s + f_l \rho_l \tag{5.2}$$

where, k_s, ρ_s are thermal conductivity and density of the solid state and k_l, ρ_l are the thermal conductivity and density of the liquid state. The solid and liquid fractions can be modeled using a Heaviside step function (H) imposed at the average melting temperature (T_m), as follows:

$$H(T) = \begin{cases} 0 & \text{if } T < T_m \\ 1 & \text{if } T > T_m \end{cases} \tag{5.3}$$

where, T represents the temperature of the body. The liquid fraction in the material can be represented directly by a Heaviside step function. The remaining volume of solid fraction can be represented by subtracting the liquid fraction from the whole, as:

$$f_l = H; \qquad f_s = 1 - f_l = 1 - H \tag{5.4}$$

The specific heat capacity of the material (c_{pm}) is defined similarly to account for the properties of solid and liquid state. Also, the latent heat of melting (L_m) is addressed by adding L_m/T_m term to the specific heat. Alternately, since melting enthalpy is absorbed in the material without increase in temperature, a Dirac-delta function (D) applied at T_m can be used to fulfill the condition, as:

$$c_{p_m} = f_s c_{p_s} + f_l c_{p_l} + L_m/T_m \quad \textit{or} \quad c_{p_m} = f_s c_{p_s} + f_l c_{p_l} + DL_m \tag{5.5}$$

The Dirac delta function is represented as the derivative of the Heaviside step function ($D = \frac{dH}{dT}$) and its integral over the temperature range is equal to 1, as follows:

$$\int_{\infty}^{-\infty} D dT = 1 \tag{5.6}$$

In many practical situations, melting occurs in an interval between the solidus temperature (T_s) and liquidus temperature (T_l), instead of a fixed melting temperature. Such cases can be modeled using a smooth Heaviside step function that provides an approximate analytical distribution between 0 and 1 in the transition temperature range. Accordingly, the modified Dirac delta function is obtained by differentiating the Heaviside step function to account for the enthalpy increase over the melting range ($T_s - T_m$ or ΔT_m). The latent heat of melting is addressed in that case by adding $L_m/\Delta T_m$ term to the specific heat.

5.1.2 Evaporation

Mass loss occurs in the form of evaporation from the molten surface of the weld. The amount of material evaporated per unit area and unit time can be calculated using the Langmuir's rate of evaporation equation, as [47]:

$$\dot{m}'' = (P_v - P_0)\sqrt{\left(\frac{M_w}{2\pi R T_{lv}}\right)} \tag{5.7}$$

where, $\dot{m}''$ is the rate of mass flux in kg m^{-2} s^{-1}; P_v is vapor pressure of the material in N m^{-2}; P_0 is the surrounding pressure; M_w is the molecular weight of the material in kg mol^{-1}; R is the universal gas constant in J mol^{-1} K^{-1}; T_{lv} is the temperature of the molten material at the liquid-vapor interface. The surrounding pressure is considered negligible especially in electron beam welding operations owing to the high vacuum environment in the beam chamber. The vapor pressure of a given material is a function of temperature and can be calculated using the following empirical relation [60]:

$$\log P_v = 5.006 + A + \frac{B}{T} + C\log T + \frac{E}{T^3} \tag{5.8}$$

The heat flux due to evaporation can also be estimated as the product of evaporative rate of mass flux and the latent heat of vaporization (L_v), as:

$$q'' = \dot{m}'' L_v \tag{5.9}$$

5.2 Numerical Analysis

The numerical model of μEBW developed and validated previously is used here to implement the phase transition conditions. The conditions of melting are imposed through the variable thermophysical properties in solid and liquid phases as shown in Eqs. (5.2) and (5.5). The latent heat of melting is added in the specific heat term in Eq. (5.5). The Heaviside step function, which is used to define the switch from the solid to liquid state, has infinite derivative at the transition and cannot be implemented numerically. Instead, the built-in smooth step function in COMSOL Multiphysics$^{\text{TM}}$ software is used. The function flc2hs$(T - T_m, dT)$ returns 0 for $T < T_m - dT$ and 1 for $T < T_m + dT$. In the interval $T_m - dT < T < T_m + dT$, flc2hs is defined by a sixth-degree polynomial and has continuous second derivative. It is important to note here that the parameter dT does not represent the melting

range (ΔT_m) and is scale factor for the resolution of the interface that depends on the computational mesh. However, the interval of $2dT$ can be adjusted accordingly to represent the transition temperature range, provided the computational capability permits a very fine mesh at the solid-liquid interface.

The evaporation phenomenon is implemented in the current model as the heat flux boundary condition on the top surface. Only the molten portion of the top surface ($T > T_m$) undergoes heat loss due to evaporation; the remaining solid area behaves as insulated surface. The flc2hs($T - T_m, dT$) function that represents the liquid fraction is multiplied with the evaporative heat flux in Eq. (5.9) such that it provides zero flux conditions everywhere except when liquid. The initial and boundary conditions applied in the numerical model can be summarized as:
- Initial condition: T_0=27 ^{0}C

- Boundary conditions:
Material inlet: $T = T_0$
Top surface: flc2hs($T - T_m, dT$) $\times$ ($\dot{m}'' L_v$)
All other sides: Insulated $\left(-k\frac{\partial T}{\partial n} = 0\right)$

It is important to validate the new numerical model as a result of the additional phase transition conditions. Validating only the melting condition implemented through modifying the governing equation is considered sufficient. The evaporation boundary condition on the top surface is ignored during the validation.

5.2.1 Validation of the Melting Condition

The asymptotic case of fast moving heat source (high Pe) where the heat diffusion is negligible, is considered for validating the melting condition. Analytical solution is derived in this study for the limiting case of no conduction; the governing equation (Eq. (5.1)) is written by ignoring the conduction terms as:

$$\rho_m c_{p_m} U \frac{dT}{dx} = q \tag{5.10}$$

The variation of properties in solid and liquid states are ignored. Considering constant properties of the material at room temperature ($\rho_m = \rho$ and $c_{p_m} = c_p$) and including the latent heat of melting in the specific heat term, Eq. (5.10) can be written as:

$$\rho \left(c_p + DL_m\right) U \frac{dT}{dx} = q \tag{5.11}$$

The solution to Eq. (5.11) can be obtained by following the approach described in Chapter 3. The additional melting term can be dealt with using the property in Eq. (5.6). The asymptotic maximum temperature of the μEBW including the melting phenomenon can be related to the maximum temperature of the process without melting, as:

$$(T_{max})_{Lm} - (T_{max})_{Lm=0} = \frac{L_m}{c_p} \tag{5.12}$$

where, T_{max} represents the asymptotic maximum temperature of the process, T_0 is the initial temperature, the subscript L_m represents the process that accounts for melting and $L_m = 0$, without melting. It is important to note here that Eq. (5.12) is valid, independent of the heat source model being used in the study; however, $(T_{max})_{Lm=0}$ is different for the exponential decay heat source models (see Chapter 3) and Kanaya-Okayama heat source model (see Chapter 4).

The difference between the asymptotic maximum temperature with and without accounting for melting is considered as the validation criteria for the numerical model; the properties of commercially pure (CP) titanium are used as an example. The numerical model is solved for a very low thermal conductivity such that the heat conduction is negligible. The maximum temperature thus obtained after incorporating melting is then compared with the previously validated numerical model without melting for both the exponential and Kanaya-Okayama heat source models.

- For the exponential decay heat source model, the maximum temperatures obtained numerically for the asymptotic case of negligible conduction are about 3268 ^{0}C and 4264 ^{0}C for the cases of melting and no melting respectively. The difference between the maximum temperatures is 656 ^{0}C which is comparable against the analytical estimation (Eq. 5.12) of 660 ^{0}C.

- For the Kanaya Okayama heat source model heat source model, the maximum temperatures obtained numerically for the asymptotic case of negligible conduction are about 1887 ^{0}C and 2543 ^{0}C for the cases of melting and no melting respectively. The difference between the maximum temperatures is 656 ^{0}C which is comparable against the analytical estimation (Eq. 5.12) of 660 ^{0}C.

Temperature Distribution

The temperature variation along the beam motion is compared separately for the two heat source models in Figs. 5.1 and 5.2. The peak value attained by the temperature curve represent the maximum temperature of the process, as studied previously in

Chapter 3. It is observed that the difference in the peak values of the temperature curves agrees with the analytical predictions.

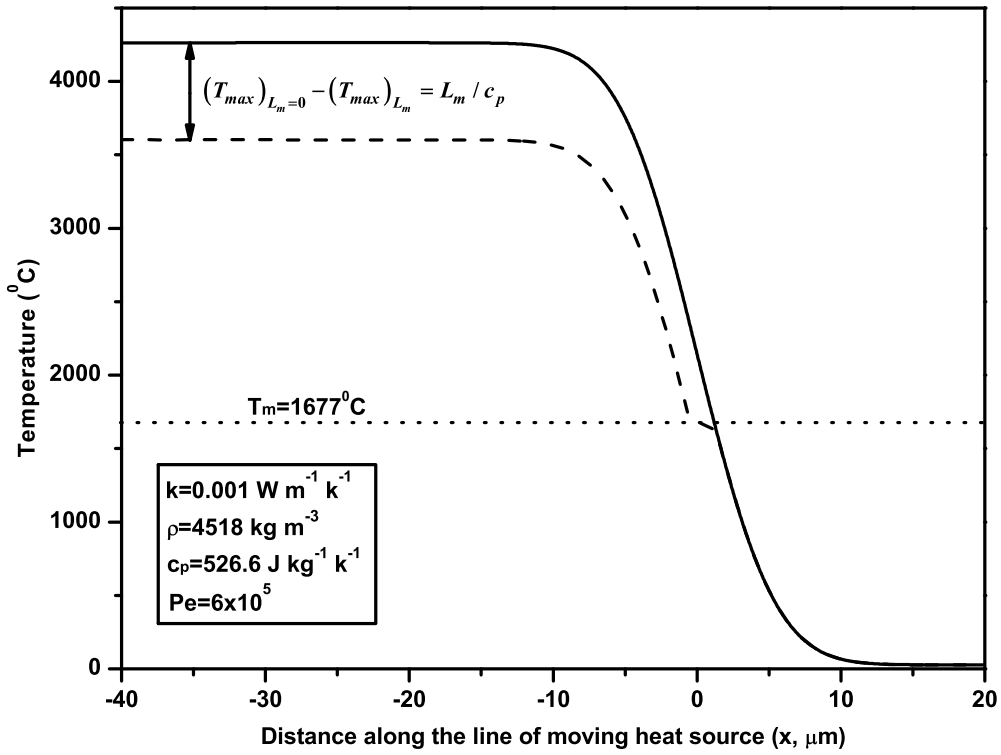

Figure 5.1 – Temperature variation along the centerline of the solid is compared in case of exponential decay heat source model with and without accounting for the melting, for the asymptotic case of negligible heat conduction. The beam parameters and material properties used to obtain the numerical solution are, W=15 W, Pe=6×10^5, k=0.001 W m^{-1} K^{-1}, ρ=4518 kg m^{-3}, and c$_p$=526.6 J kg^{-1} K^{-1}.

5.3 Effect of Evaporation

The amount of material loss occurring due to evaporation is an important consideration during μEBW. The present numerical model incorporating the melting phenomenon and the evaporative heat flux boundary condition is used to estimate the maximum depth of material loss (λ) as a result of evaporation. The material properties of CP titanium, as listed in Table 5.1, are used as an example in the present analysis. The welding parameters considered are as follows: V=28.4 kV, I=700 μA, d=10 μm, U=65.2 m s^{-1}. The welding parameters selected here are in accordance

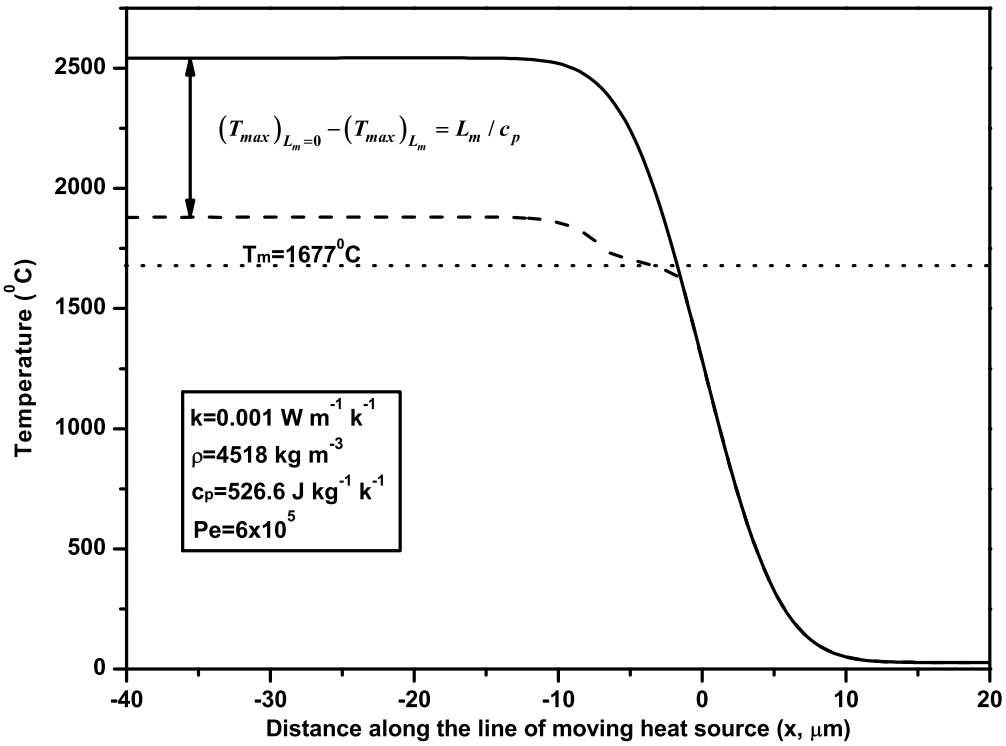

Figure 5.2 – Temperature variation along the centerline of the solid is compared in case of Kanaya-Okayama heat source model with and without accounting for the melting effect, for the asymptotic case of negligible heat conduction. The beam parameters and material properties used to obtain the numerical solution are, W=5.7 W, Pe=6×10^5, k=0.001 W m^{-1} K^{-1}, ρ=4518 kg m^{-3}, and c$_p$=526.6 J kg^{-1} K^{-1}

with the optimized conditions of Peclet number of the process to be 100 and maximum beam penetration to be twice that of the weld depth, as obtained in Chapter 4.

The rate of evaporative mass flux can be obtained on the top surface of the substrate using Eq. (5.7) and (5.8), after the temperature distribution in the body is solved numerically. A 3-D color map showing the rate of mass flux on the top surface of the substrate ($x-y$ plane) is plotted in Fig. 5.3; the negative sign of the mass flux indicates that the material is removed from the substrate. A 2-D contour of the rate of evaporative mass flux on the top surface is also depicted in the same figure. Only half region of the top surface is shown in Fig. 5.3 because of the geometrical symmetry; the $x-$axis represents the centerline along which the beam travels. The maximum rate of evaporative mass flux is observed to be 0.02 kg m^2 s^{-1}, which is

Table 5.1 – Properties of CP titanium (grade-3) used in the study [61]

Properties	Symbol	Values	Units
Thermal conductivity	k_s	15.5	[W m^{-1} K^{-1}]
	k_l	28.5	
Density	ρ_s	4518	[kg m^{-3}]
	ρ_l	4151	
Specific heat	c_{p_s}	526.6	[J kg^{-1} K^{-1}]
	c_{p_l}	967.5	
Solidus temperature	T_s	1668	[^{0}C]
Liquids temperature	T_l	1686	[^{0}C]
Average melting temperature	T_m	1677	[^{0}C]
Latent heat of melting	L_m	3.48×10^5	[J kg^{-1}]
Latent heat of vaporization [62]	L_v	9.19×10^6	[J kg^{-1}]
Initial temperature	T_0	27	[^{0}C]
Atomic mass	A	47.867	[g mol^{-1}]
Atomic number	Z	22	

typical even in macro scale evaporation of titanium alloys [47]. It is important to note here that the location of maximum rate of mass flux on the surface does not coincide with the center of the heat source. In Fig. 5.3, the position of the heat source is at 60 μm along the $x-$axis where as the maximum mass rate of mass flux is obtained at about 10 μm behind it.

Figure 5.3 depicts the distribution of rate of evaporative mass flux in a quasi steady-state system, where the heat source appears to be stationary with respect to the coordinate frame. Hence, the rate of mass flux varies from higher values near the heat source to negligible values in the far away region. In practical situation, the loss of mass flux at a specified location accumulates with time as the heat source moves over it. To obtain the profile of the depth in the material caused due to the evaporated mass, the rate of mass flux distribution is to be integrated over the entire time frame and divided by the density of the material. Only the maximum depth of material loss, which occurs along the centerline of the substrate, is of interest in the current study. Therefore, the rate of mass flux along the line of beam motion ($y = 0$) is integrated as:

$$\int_{-\infty}^{\infty} \frac{\dot{m}''(x,0)}{\rho} dt = \lambda \tag{5.13}$$

In the current quasi steady-state system, time variable can be defined in terms of the distance variable as $t = x/U$. Equation (5.13) can be written in terms of distance

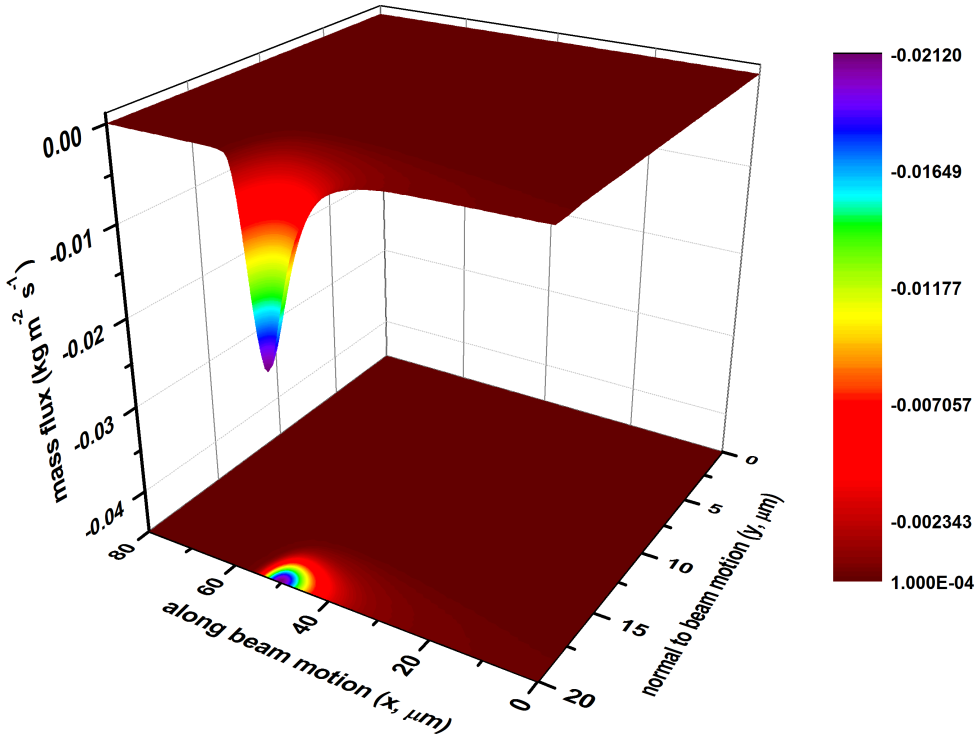

Figure 5.3 – 3-D color map and 2-D contour of the rate of evaporative mass flux on the top surface of the substrate. The negative sign of the mass flux indicates that the material is lost from the substrate.

variable and the maximum depth of material loss can be obtained by integrating the rate of mass flux over the entire length of beam travel, as:

$$\frac{1}{\rho U}\int_{x}\dot{m}''(x,0)dx = \lambda \tag{5.14}$$

The rate of mass flux along the centerline is numerically integrated using COMSOL Multiphysics^{TM}and the maximum depth of material loss is obtained as λ=6.96$\times10^{-13}$ m. It is to be noted here that the maximum depth of material loss is even smaller than a diameter of an atom (about 10^{-10} m), which indicates that the evaporation loss on the surface is negligible. The effect of evaporation in the proposed μEBW is negligible because of the relatively low temperatures obtained on the surface.

Considering the negligible impact of the evaporation phenomenon on μEBW, the evaporation boundary condition is ignored in the numerical model in subsequent sim-

ulations, to save computer time.

The numerical model now accounting for the phase transition conditions, is a closer representation of the practical microwelding conditions. The optimal parameters of microwelding investigated using the numerical model is used to suggest experiments.

5.4 Challenges in Performing Experiments of the Proposed μEBW

The combination of welding parameters (high voltage, high current, small beam diameters, and high weld speeds) proposed as a result of the current numerical analysis of μEBW are uncommon either for a macro electron beam welder or a scanning electron microscope. The following major challenges are faced in adapting an electron beam equipment to the proposed range of welding parameters:

1. The beam diameter in an electron beam is typically reduced by removing the peripheral electrons. This results in the decrease of beam current. Hence, it is difficult to attain higher beam currents in extremely focussed diameters, as required by the current proposal.

2. A high current density beam resulting from pumping large number of electrons in to a small diameter might be difficult to focus. A preliminary analysis of beam defocusing based on the electrostatic repulsion of the electrons in the beam column is shown in Appendix B.

3. The current proposal suggests very high electron beam deflections (weld speeds) that are not considered before.

5.5 Discussion

The properties of the material at room temperature are used in the calculation of Pe and beam penetration through out the study. Both the Pe and beam penetration will vary from the present calculations when the material properties change as a result of melting near the top surface. Also, the optimum conditions of μEBW (Pe of 100 and beam penetration twice that of the melting depth), obtained in Chapter 4, without taking into account the phase change, will vary. However, the marginal change in the material's response to the process parameters is ignored considering the high controllability of the proposed microwelding, as demonstrated in Chapter

3. Moreover, the fast moving heat source considered in the present study results in trailing of the molten pool behind the heat source. The major portion of the area where the electrons penetrate the surface is still in the solid state and thus, using the solid state properties of the material to calculate the beam penetration is justified.

The variation of thermophysical properties of the material with temperature will also change the current predictions of Pe and beam penetration, but the deviation is expected to be minimal considering the low the sensitivity of the process, as discussed in Chapter 3.

Incorporating the melting phenomena numerically is challenging as it requires to resolve the mesh very finely at the liquid-solid interface. The mesh parameter dT, which depends on the mesh density, defines the temperature range over which the transition from solid to liquid occurs. Ideally, $2dT$ should be equal to the difference between the solidus and liquidus temperatures for the numerical model to represent the practical case. However, the immense computational resources required to produce a fine mesh often results in compromising the mesh parameter dT. Typically, dT is chosen 2 to 3 times the transition temperature range, which can be a source of error in the numerical solution. The error is observed to be negligible in the present study where the numerical results compares well with the analytical solutions.

Evaporation is investigated to have negligible impact on the proposed μEBW. This is in contrast to the case of laser microwelding where surface ablation is a major set back.

The liquid phase in the material is treated as rigid body in the present study. Convection of fluid in the molten pool due to the Marangoni effect is ignored. This approximation becomes invalid at high Peclet number of fluid convection inside the molten pool. The following equation can be used to estimate the Peclet number of fluid (Pe_f) due to the Marangoni effect when the fluid flow is dominated by inertial forces (Re>1), the derivation of which is shown in Appendix A:

$$Pe_f = \frac{v_c w}{\alpha} = \frac{1}{\alpha}\sqrt{\frac{2\sigma_T w(T_{max} - T_m)}{\rho}} \tag{5.15}$$

where, v_c can be defined as the characteristic velocity of the fluid in the weld pool, σ_T is the temperature coefficient of surface tension and w is the half weld width. Considering a half weld width of 80 μm in steel (for the case shown in Fig. C.3 in Appendix C), T_{max} of 2165 ^{0}C, and T_m of 1492 ^{0}C, the characteristic velocity of fluid in the weld

pool (v_c) and Pe_f are found to be about 0.6 m $s^{-}1$ and 11.7 respectively for material properties σ_T=1.5×10^{-4}, α=4.1×10^{-6}, and μ=5.75×10^{-3} [63]. Such high values of Pe_f suggests that fluid convection might be significant in the molten pool, the effect of which can be analyzed by incorporating Marangoni flow into the numerical model. However, the Pe_f is expected to further decrease as the weld scale decreases. The low Pe_f suggests that fluid convection can be ignored in the molten pool and the liquid phase can be treated as a rigid body, as considered in the present study.

The Reynolds number of the fluid is calculated, using the formulation in Appendix A, to be 58.6 for the present case. The high Reynolds number justifies the initial consideration that the flow is dominated by inertial forces.

5.6 Conclusion

The phase transition phenomena such as melting and evaporation are incorporated in the numerical model of μEBW. The maximum depth of material loss on the weld surface as a result of evaporation is investigated to be negligible. The challenges faced in adapting an electron microscope to provide the proposed welding parameters are discussed.

Chapter 6

Conclusions and Future Work

For the first time, it is established that welding is possible in the high heat intensity conditions that has been considered impossible before. The key to employ high intensity heat sources for welding is volumetric heating. Such an approach has important implications for welding at micro and nano scales.

A comprehensive numerical model to simulate μEBW is developed for the first time in this research. Three dimensional temperature distribution in the solid near the heat source for a given choice of welding parameters can be predicted using the numerical model. The prior knowledge of temperature distribution in the solid as a result of microwelding can help to produce high quality welds.

A new three dimensional distributed heat source model to represent the volumetric heating of electron beam is formulated. The heat source model is crucial for the analysis of microwelding and can be applied in any other electron heating applications where fast moving heat sources are prevalent. Further, a theoretical approach to estimate the electron beam heating efficiency as a function of material atomic number only is proposed using the present heat source model. No previous literature exists that provides electron beam heating efficiency in general.

The numerical model of μEBW is used to optimize the welding parameters that can be used to obtain a given weld size in any material. The optimal welding parameters are reported in terms of non-dimensional Peclet number, that indicates the beam scan speed based on the beam size and material properties, and relative beam penetration, which guides the choice of the beam voltage (in directly beam current as well) based on the material properties and weld depth required. The following are the important conclusions:

1. The optimum Peclet number of μEBW is found to be 100. For Peclet numbers larger than 100, the process requirements (e.g. beam velocity) increases without meaningful gains in controllability, excess heat, maximum temperature, or weld shape. At Peclet numbers below 100, the maximum temperature of the process lowers; however, the process quickly loses controllability and there is excessive heat lost into the substrate surrounding the weld.

2. The optimum value of maximum electron penetration in the solid is found to be twice that of the required weld depth. At electron penetrations below the optimum, the process starts to resemble a traditional surface heating process such as laser welding consistent with potentially excessive surface ablation. Also, the heat input required by the process is high for a given size of weld. At electron penetrations above the optimum, the process results in excessive direct heating beyond the depth of the weld, possibly damaging the surroundings of the device being welded, and worsening the controllability of the process

The following discussions are relevant for the future considerations of this work:

- The experimental beam conditions proposed in this study is uncommon even for modified SEMs intended to carry out microwelding. A better understanding of the electron beam set up is to be gained to adapt the typical SEMs to the proposed conditions.

  An existing electron microscope at the Lawrence Livermore National Laboratory, US provides the combination of high currents in focussed diameters. However, it has the limitation that the beam diameter cannot be decreased below 0.2 mm in which up to 40 mA current can be obtained. The present numerical model is used to propose proof-of-concept experiments to be carried out in the given electron microscope, which are illustrated in Appendix C.

- The continuum approximation made in this study for carrying out the heat transfer analysis is invalid as the welding scales decrease below 10 nm. The ballistic-diffusive heat transfer models valid at such low scales are to be used to increase the predictability of the process.

- No fluid flow in the molten pool is considered in this study. The fluid convection due to the Marangoni effect becomes significant at higher Peclet number of fluid flow and hence should be incorporated into the numerical model. Typically, the maximum temperature in the molten region is reduced due to the fluid convection which is considered favorable for microwelding.

Bibliography

[1] G.A. Knorovsky, D.O. MacCallum, E.A. Holm, J.R. Michael, V.V. Semak, and B.M. Nowak-Neely. Trends in microwelding. In *Proceedings of the 7th International Conference on Trends in Welding Research, Callaway Gardens Resort, Pine Mountain, Georgia, USA*, 2005.

[2] Norman Y. Zhou, editor. *Microjoining and nanojoining*. Woodhead publishing limited, Cambridge, England, CRC press, 2008.

[3] S. Safarevich and J. Xie. Peculiarities of micro laser welding of medical devices. In *Medical Device Materials - Proceedings of the Materials and Processes for Medical Devices Conference, Anaheim, CA*, pages 31–36, Anaheim, CA, 2003.

[4] G. A. Knorovsky, D. O. MacCallum, and R. A. Roach. The effect of surface tension on microjoining. In *Proceedings from Joining of Advanced and Specialty Materials*, pages 62–66, Columbus, Ohio, October 18-20 2004.

[5] J.F. Lancaster. The physics of welding. *Physics in Technology*, 15(2):73–79, 1984.

[6] T. W. Eagar. Energy sources used for fusion welding. *ASM Handbook-Welding, Brazing, and Soldering*, 6:, 1993.

[7] G. A. Knorovsky, B. M. Nowak-Neely, and E. A. Holm. Microjoining with a scanning electron microscope. *Science and Technology of Welding and Joining*, 11(6):641–649, 2006. ISSN 1362-1718.

[8] K.W. Guo. A review of micro/nano welding and its future developments. *Recent Patents on Nanotechnology*, 3(1):53–60, 2009.

[9] D. MacCallum, G. Knorovsky, and B. Nowak-Neely. Microwelding using a modified sem. In *Proceedings of the 7th International Conference on Trends in Welding Research, Callaway Gardens Resort, Pine Mountain, Georgia, USA*, 2005.

[10] G. A. Knorovsky, D. O. MacCallum, and M. T. Meyers. Selection of parameters for u e-beam welding. *Science and Technology of Welding and Joining*, 11(6): 672–680, Nov 2006. ISSN 1362-1718.

[11] Y. Zhou, A. Hu, Khan M.I., W. Wu, B. Tam, and M. Yavuz. Recent progress in micro and nano-joining. *Journal of Physics: Conference Series*, 165, 2009.

[12] IH Hwang and SJ Na. A study on heat source modeling of scanning electron microscopy modified for material processing. *Metallurgical and Materials Transactions; B-Process Metallurgy and Materials Processing Science*, 36(1):133–139, 2005.

[13] Jan Baertle, Thorsten Lower, and Dietrich Von Dobeneck. Electron beam welding beyond the ordinary scale. In *8-th International Conference on Electron Beam Technologies,Varna, Bulgaria*, Varna, Bulgaria, 5-10. June 2006,.

[14] S. Bohm, T. Welters, G. Tanasie, M. Zah, A. Reiter, J. Baertle, and T. Lower. Entwicklung eines elektronenstrahlbasierten mikroproduktionszentrums. In *Technologien und Werkstoffe der Mikro- und Nanosystemtechnik.Hrsg.:VDI;VDE;GMM, Karlsruhe, Germany*, pages 24–27, 2007.

[15] Gheorghe Tanasie, Stefan Bohm, Jan Bartle, Thorsten Lower, Andrea Reiter, Michael Franzkowiak, and Gunther Reinhart. Electron beam machining of microsystem products. In *2nd European Conference & Exhibition on Integration Issues of Miniaturized Systems - MOMS, MOEMS, ICS and Electronic Components, Barcelona, Spain*, Barcelona, Spain, 2008.

[16] U. Reisgen and T. Dorfmueller. Micro-electron-beam welding with a modified scanning electron microscopy: Findings and prospects. *Journal of Vaccum Science & Technology B*, 27(3):1310–1314, 2009.

[17] Hiroki Ogawa, Ming Yang, Yukiko Matsumoto, , and Wei Guo. Welding of metallic foil with electron beam. *Journal of Solid Mechanics and Materials Engineering*, 3(4):647–655, 2009.

[18] G. Smolka, A. Gillner, L. Bosse, and R. Lultzeler. Micro electron beam welding and laser machining-potentials of beam welding methods in the micro-system technology. *Microsystem Technologies*, 10(3):187–192, 2004.

[19] U Dilthey and T Dorfmuller. Micro electron beam welding. *Microsystem Technologies-Micro and Nanosystems-Information Storage and Processing Systems*, 12(7):626–631, 2006.

[20] U. Reisgen and T. Dorfmueller. Developments in micro-electron beam welding. *Microsystem Technologies-Micro and Nanosystems-Information Storage and Processing Systems*, 14(12):1871–1877, 2008.

[21] D. Drouin, A.R. Couture, D. Joly, X. Tastet, V. Aimez, and R. Gauvin. Casino v2.42 - a fast and easy-to-use modeling tool for scanning electron microscopy and microanalysis users. *Scanning*, 29(3):92–101, 2007.

[22] K Kanaya and S Okayama. Penetration and energy-loss theory of electrons in solid targets. *Journal of Physics, D:Applied Physics*, 5(1):43–58, 1972.

[23] H. Schwarz. Mechanism of high-power-density electron beam penetration in metal. *Journal of Applied Physics*, 35(7):2020–29, 1964.

[24] S. Brown, J. Clevenger, and P. Mendez. Electron beam welding method and apparatus using controlled volumetric heating, US 2006/0102597 A1 2006.

[25] M. Sanders and P. F. Mendez. Electron beam welding at the micron scale. In *Fabtech/AWS Annual Meeting, Atlanta, GA.*, Cincinnati, OH, 2006.

[26] S. S. Gajapathi, S. K. Mitra, and P. F Mendez. Modeling of micro welding process using electron beam under high peclet number. In *Proceedings of the ASME 2010 International Mechanical Engineering Congress & Exposition, Vancouver, Canada*, 2010.

[27] S. S. Gajapathi, P.F. Mendez, and S.K. Mitra. Analytical method to study the temperature distribution of a moving heat source electron beam micro-welding. In *7th International Conference on Heat Transfer, Fluid Mechanics and Thermodynamics, Antalya, Turkey*, 19-21 July 2010.

[28] D. Rosenthal. The theory of moving sources of heat and its application to metal treatments. *Transactions of the American Society of Mechanical Engineers*, 68: 849–866, 1946.

[29] T.W. Eagar and N.S. Tsai. Temperature-fields produced by travelling distributed heat-sources. *Welding Journal*, 62(12):S346–S355, 1983.

[30] G. Araya and G. Gutierrez. Analytical solution for a transient, three-dimensional temperature distribution due to a moving laser beam. *Internationan Journal of Heat and Mass Transfer*, 49(21-22):4124–4131, OCT 2006.

[31] P. Levin. A general solution of 3-d quasi-steady-state problem of a moving heat source on a semi-infinite solid. *Mechanics Research Communications*, 35(3):151–157, 2008.

[32] J. Kidawa-Kukla. Temperature distribution in a rectangular plate heated by a moving heat source. *International Journal of Heat and Mass Transfer*, 51(3-4): 865–872, 2008.

[33] J. Goldak, A. Chakravarti, and M. Bibby. A new finite-element model for welding heat-sources. *Metallurgical Transactions B-Process Metallurgy*, 15(2):299–305, 1984.

[34] M. F. Modest and H. Abakians. Heat conduction in a moving semi-infinite solid subjected to pulsed laser irradiation. *Journal of Heat Transfer*, 108:597–601, 1986.

[35] D.J. Sanders. Temperature distributions produced by scanning gaussian laser-beams. *Applied Optics*, 23(1):30–35, 1984.

[36] F. P. Incropera, D. P. DeWitt, T. L. Bergman, and A. S. Lavine. *Fundamentals of heat and mass transfer*. John Wiley & Sons, Inc., 6th edition, 2007.

[37] S. Kou. *Welding metallurgy*. John Wiley & Sons, Inc., Hoboken, New Jersey, 2003.

[38] S. S. Gajapathi, S. K. Mitra, and P. F Mendez. Controlling heat transfer in microwelding using volumetric heating. *International Journal of Heat and Mass Transfer*, 2011. doi: 10.1016/j.ijheatmasstransfer.2011.07.033.

[39] N.T. Nguyen, A. Ohta, K. Matsuoka, N. Suzuki, and Y. Maeda. Analytical solutions for transient temperature of semi-infinite body subjected to 3-d moving heat sources. *Welding Journal*, 78(8):265S–274S, AUG 1999.

[40] H. Ye, Y. Luo, Z. Yan, and B. Shen. Numerical simulation on temperature field of electron beam welding of magnesium alloy and study on properties and microstructure of joint. *Materials Science Forum*, 575-578 PART 1:660–665, 2008.

[41] Y. Luo, J. Liu, H. Ye, Z. Yan, and B. Shen. Numerical simulation on temperature field of electron beam welding of az61 magnesium alloy. *Hanjie Xuebao/Transactions of the China Welding Institution*, 30(3):73–76, 2009.

[42] C.S. Wu, H.G. Wang, and Y.M. Zhang. A new heat source model for keyhole plasma arc welding in fem analysis of the temperature profile. *Welding Journal (Miami, Fla)*, 85(12):284–s–291–s, 2006.

[43] J.W. Elmer, M.A. Newton, and A.C. Smith. Rapid thermal-processing of steel using high-energy electron-beams. In Bakish, R, editor, *Proceedings of the Conference on the Laser and the Electron Beam in Welding, Cutting and Surface Treatment: State of the Art 1993*, pages 91–104, RENO, NV, Oct 31-Nov 02 1993.

[44] K. Voges, T. Welters, S. Bohm, and K. Dilger. The application of monte-carlo methods to electron-beam interactions with solids for the prediction of micromachining capabilities. In *8-th International Conference on Electron Beam Technologies*, pages S. 46–60, Varna, Bulgaria, 5-10. June 2006,.

[45] S. Tricot, N. Semmar, L. Lebbah, and C. Boulmer-Leborgne. Zno sublimation using a polyenergetic pulsed electron beam source: Numerical simulation and validation. *Journal of Physics D: Applied Physics*, 43(6), 2010.

[46] S. Schiller, U. Heisig, and S. Panzer. *Electron Beam Technology*. John Wiley & Sons, 1982.

[47] A. Powell, J. Van Den Avyle, B. Damkroger, J. Szekely, and U. Pal. Analysis of multicomponent evaporation in electron beam melting and refining of titanium alloys. *Metallurgical and Materials Transactions B: Process Metallurgy and Materials Processing Science*, 28(6):1227–1239, 1997.

[48] Y. Qin, C. Dong, X. Wang, S. Hao, A. Wu, J. Zou, and Y. Liu. Temperature profile and crater formation induced in high-current pulsed electron beam processing. *Journal of Vacuum Science and Technology A: Vacuum, Surfaces and Films*, 21(6):1934–1938, 2003.

[49] A. Nouiri, S. Chaguetmi, and N. Belabed. Monte carlo model of the temperature rise at a gaas surface under an electron beam. *Surface and Interface Analysis*, 38(7):1153–1157, 2006.

[50] W. Bothe. *Zeitschrift fur Naturforschung*, 4a:542, 1949.

[51] H. Kulenkampff and W. Spyra. Energieverteilung ruckdiffundierter elektronen. *Zeitschrift fur Physik*, 137(4):416–425, 1954.

[52] E.J. Sternglass. Backscattering of kilovolt electrons from solids. *Physical Review*, 95(2):345–358, 1954.

[53] H. Kulenkampff and K. Ruttiger. Untersuchung der energieverteilung ruckdiffundierter elektronen an dunnen metallschichten. *Zeitschrift fur Physik*, 152(2): 249–260, 1958.

[54] H. Niedrig. Physical background of electron backscattering. *Scanning*, 1(1): 17–34, 1978.

[55] G.D. Archard. Back scattering of electrons. *Journal of Applied Physics*, 32(8): 1505–1509, 1961.

[56] T. Tabata, R. Ito, and S. Okabe. An empirical equation for the backscattering coefficient of electrons. *Nuclear Instruments and Methods*, 94(3):509–513, 1971.

[57] W. Reichelt. Production and condensation of metal vapors in large quantities. *Angewandte Chemie International Edition in English*, 14(4):218–222, 1975.

[58] D.C. Joy. A database on electron-solid interactions. *Scanning*, 17(5):270–275, 1995.

[59] D. Y. Tzou. *Macro- to microscale heat transfer: the lagging behavior*. Taylor and Francis, Wahington, US, 1997.

[60] David R. Lide, editor. *CRC Handbook of Chemistry and Physics*. CRC Press Inc., Boca Raton, Florida, 90th edition, 2009.

[61] N. Saunders, Z. Guo, X. Li, A. P. Miodownik, and J.P. Schille. Using jmatpro to model materials properties and behavior. *JOM 55/12*, pages 60–65, 2003.

[62] M.W. Chase. *JANAF Thermochemical Tables*. American Institute of Physics, Inc., New York, NY, 3rd ed. edition, 1986.

[63] P. F. Mendez. *Order of magnitude scaling of complex engineering problems, and its application to high productivity arc welding*. PhD thesis, Massachussetts Institute of Technology, June 1999.

[64] Jyrki Miettinen. Calculation of solidification-related thermophysical properties for steels. *Metallurgical and Materials Transactions B*, 28B:281–297, 1997.

Appendix A

Derivation of Peclet Number of Fluid Flow in the Molten Pool

The Marangoni convection occurs in the weld pool as a result of surface tension gradients. The surface tension gradients occurs due to large variation of the temperature on the fluid surface. A schematic of the fluid flow due to Marangoni effect is shown in Fig. A.1.

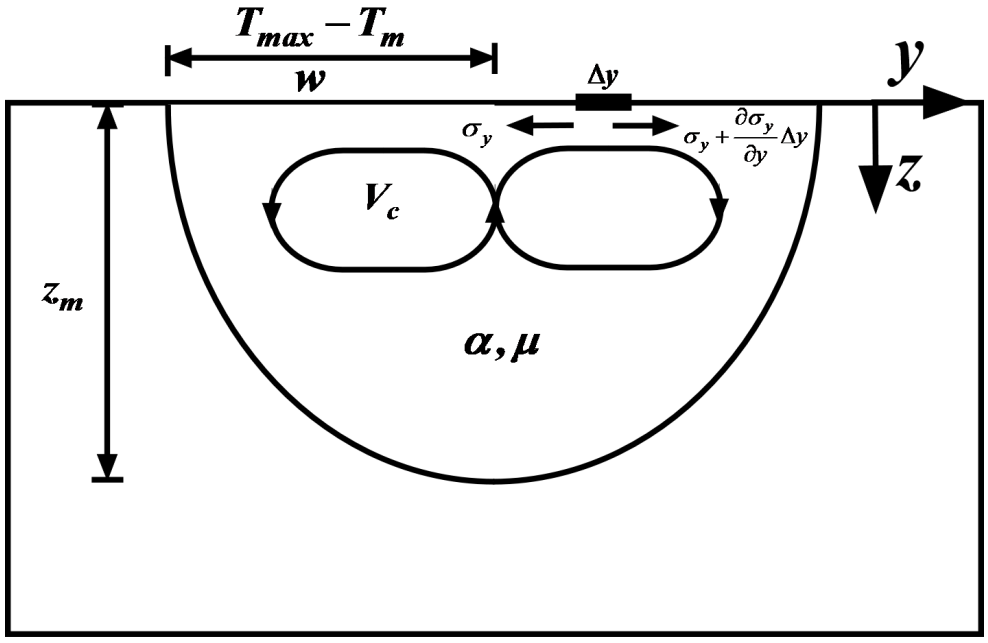

Figure A.1 – Schematic of Marangoni flow occurring in the weld pool.

The variation of surface tension (σ) across a differential element Δy as shown in Fig. A.1 can be derived as:

$$\sigma_y + \frac{\partial \sigma_y}{\partial y}\Delta y - \sigma_y = \frac{\partial \sigma}{\partial y}\Delta y \tag{A.1}$$

The surface tension being a function of the temperature can be expressed using chain rule as:

$$\frac{\partial \sigma}{\partial y} = \frac{\partial \sigma}{\partial T}\frac{\partial T}{\partial y} = \sigma_T \frac{\partial T}{\partial y} \tag{A.2}$$

where, σ_T is the coefficient of surface tension and can be found in the literature [63].

Considering a high Reynolds number flow (Re>1), the driving force of the fluid element due to surface tension gradient is balanced by the inertial forces, which can be written using the principle of scaling as:

$$\frac{1}{2}\rho {v_c}^2 = \sigma_T \frac{\Delta T}{\Delta y} \tag{A.3}$$

where, v_c can be defined as the characteristic velocity of the fluid in the weld pool and ρ is the density of the material. In the weld pool, considering ΔT=$T_{max} - T_m$ and Δy=w, where w is half weld width, Eq. A.3 can be written as:

$$\frac{1}{2}\rho {v_c}^2 = \sigma_T \frac{T_{max} - T_m}{w} \tag{A.4}$$

Thus, the characteristic velocity can be found out as:

$$v_c = \sqrt{\frac{2\sigma_T (T_{max} - T_m)}{w\rho}} \tag{A.5}$$

The Peclet number of the fluid flow in the weld pool can be calculated based on the characteristic velocity found in Eq. A.5 and considering half weld width as length scale, such that:

$$Pe_f = \frac{v_c w}{\alpha} = \frac{1}{\alpha}\sqrt{\frac{2\sigma_T w (T_{max} - T_m)}{\rho}} \tag{A.6}$$

The Reynolds number (Re) of the fluid flow can also be determined based on the characteristic velocity found in Eq. A.5 and considering half weld width as length scale such that:

$$Re = \frac{\rho v_c w}{\mu} \tag{A.7}$$

where, μ is the viscosity of the molten material.

Appendix B

Maximum Defocusing of the Electron Beam

The total number of electrons traveling per second (N) in a beam column for a specified beam current (I) can be calculated as:

$$N = \frac{I}{e} \tag{B.1}$$

where, e is the charge of an electron (1.6×10^{-19} Coulomb).

The electrons accelerate in the beam column as a result of the electrostatic field. The kinetic energy of the electron can be calculate by multiplying the beam voltage (V) times the charge of an electron. It is important to note here that as the relativistic energy equation should be used to calculate the kinetic energy of the electron as its motion approaches the speed of light, as:

$$Ve = m_0c^2 \left[\frac{1}{\sqrt{1 - \frac{{v_e}^2}{c^2}}} - 1 \right] \tag{B.2}$$

where m_0 is the rest mass of an electron (9.11×10^{-31} kg), c is the speed of light (3×10^8 m s^{-1}), v_e is the velocity of the electron in the beam column. For a 50 kV beam, the velocity of the electrons is found to be 8.9×10^7 m s^{-1} (0.3c).

Considering all the electrons in the beam to travel one after another, the average distance (ζ) between two consecutive planes containing electrons can be found by dividing the velocity of an electron with the total number of electrons traveling per second, as:

$$\zeta = \frac{v_e}{N} \tag{B.3}$$

where, ζ is the inter-plane gap. The inter-plane gap calculated by the above formulation provides the minimum value because of the approximation that only one electron crosses a plane at a time. The minimum inter-plane gap for a beam of 50 kV voltage and 200 μA current is calculated to be about 72 nm.

The distance between the two nearest electrons in the beam column is to be known to find the electrostatic repulsive force between them. The knowledge of the inter-plane gap and the width of the plane, that represents the beam diameter, can be used to estimate the minimum distance between the two nearest electrons. For a typical electron beam diameter of 10 μm and inter-plane gap of 72 nm as represented in Fig. B.1, the volumetric density of the electrons in the beam column can be found out to be 0.18 electron per cubic micrometer (such that one electron is present in a cylindrical region of 10 μm diameter and 72 nm thickness). Considering that the electrons in the beam column are arranged along the centers of the cube, the distance between the two nearest electrons would be equal to the side of the cube. The side length of a cube of volume 1/0.18 cubic meter is found as 1.77 μm.

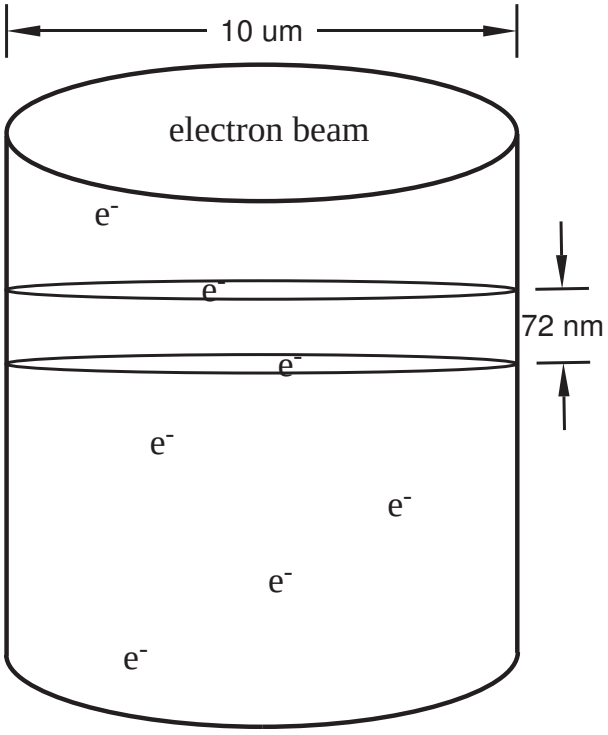

Figure B.1 – Schematic of the electrons traveling inside the cylindrical shaped beam.

An estimation of beam deflection can be found out by obtaining the final displace-

ment of an electron due to the repulsive forces in the beam column. The following Coulomb's law that defines the electrostatic force between two point charges as a function of the distance between them (x)is used:

$$m\frac{d^2x}{dt^2} = k_e\frac{e^2}{x^2} \tag{B.4}$$

where k_e is the Coulomb force constant which is 8.99×10^9 N m^2 C^{-2}. The final displacement between the two electrons depends on the repulsive forces and can be obtained by solving the second order ordinary differential equation (Eq. B.4) using the Van Der Pol solution method for stiff equations using MATLAB^{TM}. The distance between the two nearest electrons is used as an initial condition ($x = 1.77\mu$m at t=0). The other boundary condition used in solving Eq. B.4 is the zero velocity of the electrons in the lateral direction at t=0. The final distance between the two electrons as they are repelled by each other due to the electrostatic force is found at the end of the beam column. The final time that the electrons take to travel across the beam column can be calculated by knowing the height of the beam chamber (h_e) and the velocity of the electron (from Eq. B.2) by using the relation: $t_e = h_e/v_e$.

For a 50 kV/200 μA/10 μm diameter beam and typical electron gun height of 1.8 m, the final displacement of an electron at the target surface is found to be about 333 μm.

The beam defocusing should be an important consideration while using extremely small spot sizes and/or high beam currents.

Appendix C

Proposal of Experiments

The numerical model using the Kanaya-Okayama heat source with realistic boundary conditions is used to propose proof of concept experiments. The weld size aimed to attain here is in sub-millimeter scale rather than micron scale due to the limitations of the experimental capabilities. The electron beam microscope used for the experiments is capable of providing a constant beam diameter of 0.2 mm; also, the voltage and beam speeds have an upper limit of 140 kV and 25 in $\sec^{-2}$. These limitations are taken into account such that the suggested parameters fall in the feasible range of the equipment.

The material samples on which the experiments are to be performed are prepared according to requisites of the sample holder. Each sample is cut into a rectangular block with 36 mm length, 26 mm width, and 2.5mm depth such that it fits into the sample holder. The top surface of the sample on which the welds are to be formed is polished to 5 μin surface roughness. The high quality surface finish is in accordance with the demands of the shallow weld depth being formed. A schematic showing the dimensions of the sample material is shown in Fig. C.1. Only the region in the center of the specimen of 18 cm width is accessible to the electron beam inside the beam chamber. The electron beam scans along the width of the sample to form straight-line welds. Ten welds are planned in the available region in each specimen. The following precautions are taken while deciding the size of the welds and the gap between them:

1. The gap between the two adjacent welds is decided such that the second weld is not affected by the preheat of the earlier weld. The time taken by the electron beam operation to perform two consecutive scans is taken into account. The gap between the two welds is now decided such that the travel time of heat diffusion is larger than the idle time of the beam between two consecutive welds.

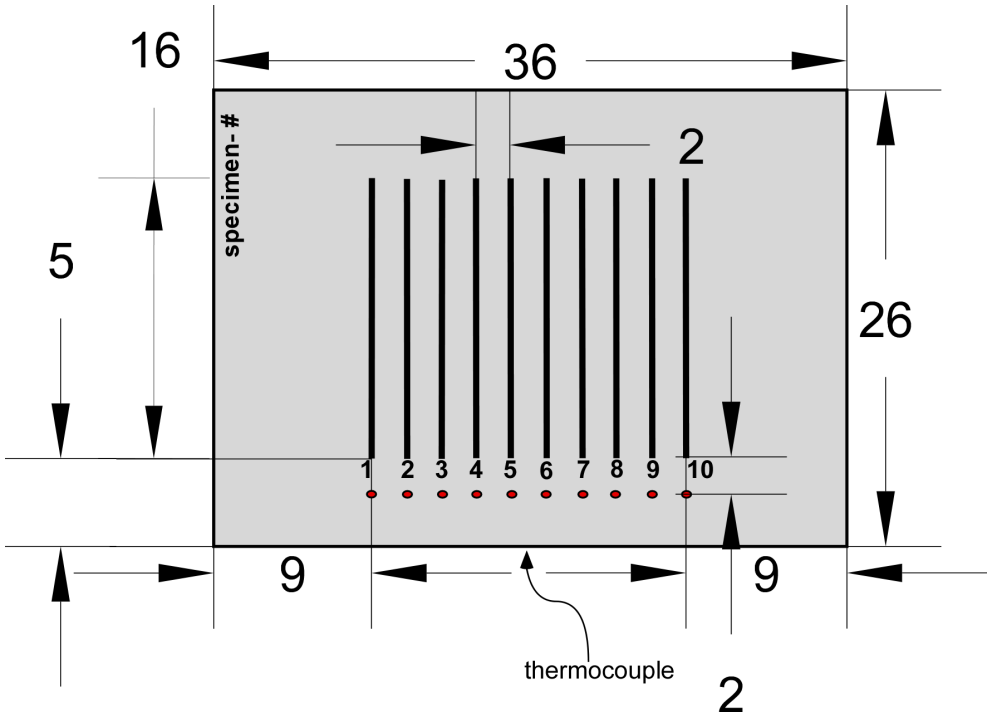

Figure C.1 – Schematic representation of the top-view of sample and the weld lines with all the dimensions specified in millimeters.

2. The overall heating as a result of multiple welds is also taken into account to control the temperature rise of the sample. The maximum temperature change can be approximated by calculating the total energy input and dividing by the heat capacity of the material. Total energy input can be estimated by summing up the power of the beam times the scan time for all the ten welds.

The numerical model is used to suggest the most optimum conditions of microwelding in CP titanium and AISI 1016 steel, the properties of which are shown in Tables C.1 and C.2. The optimum conditions are in accordance with hypothesis developed in Chapter 4 that the Peclet number of the process should be 100 and the beam penetration should be twice the maximum melting depth. The optimum welding conditions suggested for carrying out μEBW in titanium sample are: V=140 kV, I= 2.5 mA, d=0.2 mm, and U=3.4 m s^{-1} and in AISI 1016 steel sample are: V=140 kV, I= 2.9 mA, d=0.2 mm, and U=3.3 m s^{-1}

Acknowledging the several sources of error in a practical situation that cannot be accounted in a numerical model, the minimum and maximum conditions of welding are also obtained through numerical simulations to provide a bracket of acceptable

Table C.1 – Properties of CP titanium (grade-3) used in the study [61]

Properties	Symbol	Values	Units
Thermal conductivity	k_s	15.5	[W m^{-1} K^{-1}]
	k_l	28.5	
Density	ρ_s	4518	[kg m^{-3}]
	ρ_l	4151	
Specific heat	c_{p_s}	526.6	[J kg^{-1} K^{-1}]
	c_{p_l}	967.5	
Solidus temperature	T_s	1668	[^{0}C]
Liquids temperature	T_l	1686	[^{0}C]
Average melting temperature	T_m	1677	[^{0}C]
Latent heat of melting	L_m	3.48×10^5	[J kg^{-1}]
Latent heat of vaporization [62]	L_v	9.19×10^6	[J kg^{-1}]
Initial temperature	T_0	27	[^{0}C]
Atomic mass	A	47.867	[g mol^{-1}]
Atomic number	Z	22	

Table C.2 – Properties of AISI 1016 steel used in the study [64]

Properties	Symbol	Values	Units
Thermal conductivity	k_s	53.72	[W m^{-1} K^{-1}]
	k_l	35	
Density	ρ_s	7846	[kg m^{-3}]
	ρ_l	7016	
Specific heat	c_{p_s}	454	[J kg^{-1} K^{-1}]
	c_{p_l}	813	
Solidus temperature	T_s	1467	[^{0}C]
Liquids temperature	T_l	1517	[^{0}C]
Average melting temperature	T_m	1492	[^{0}C]
Latent heat of melting	L_m	2.96×10^5	[J kg^{-1}]
Initial temperature	T_0	25	[^{0}C]
Atomic mass	A	55.85	[g mol^{-1}]
Atomic number	Z	26	

welding parameters. The minimum condition of welding can be described as the combination of welding parameters which heats the target surface just up to the melting point. Similarly, the maximum condition of welding can be described when the target surface is heated up to the boiling point. The welding parameters within the bracket of minimum and maximum conditions can be considered as the feasible range of microwelding, if not ideal, for a specific case.

The μEBW is governed by beam voltage (V), beam current (I), beam diameter (d), and beam traveling speed (U) which can be controlled independently. Out of the four welding parameters, the beam diameter is kept constant in this study. Thus, the remaining three parameters are available for adjustments during the experiments. Each of these parameters have a minimum and maximum limit for a specific case as obtained through the numerical modeling. In the present study, ten experiments are planned to study the effect of varying each of the independent welding parameters in the given range; the variation of a specific welding parameter between the minimum, optimal, and maximum limit is based on geometric progression. The table of values suggested for the experiments for CP titanium and AISI 1016 steel are listed in Tables C.3, C.4, C.5, C.6, C.7, and C.8.

Table C.3 – Effect of beam traveling speed on μEBW of CP-titanium (Grade-3)

	Voltage (kV)	Current (mA)	Speed (m s^{-1})
weld 1(1)	140	2.5	6
weld 1(2)	140	2.5	4.5
weld 1(3)	140	2.5	4.1
weld 1(4)	140	2.5	3.7
weld 1(5)	140	2.5	3.4
weld 1(6)	140	2.5	2.7
weld 1(7)	140	2.5	2.1
weld 1(8)	140	2.5	1.7
weld 1(9)	140	2.5	1
weld 1(10)	140	2.5	0.6

The shape of the weld produced in the material samples can be predicted by plotting the melting isotherms in the $y - z$ plane perpendicular to the motion of the beam in the numerical model. It is important to note here that the specific $y - z$ plane, which contains the maximum melting depth, represents the weld shape. The weld shape obtained as a result of the proposed parameters in CP titanium and AISI 1016 steel are shown in Figs. C.2 and C.3. The two temperature isotherms shown represents the solidus and liquidus temperature lines.

Table C.4 – Effect of beam current on μEBW of CP-titanium (Grade-3) beam current

	Voltage (kV)	Current (mA)	Speed (m s^{-1})
weld 1(1)	140	1	3.4
weld 1(2)	140	1.6	3.4
weld 1(3)	140	1.9	3.4
weld 1(4)	140	2.2	3.4
weld 1(5)	140	2.5	3.4
weld 1(6)	140	3.1	3.4
weld 1(7)	140	3.9	3.4
weld 1(8)	140	4.8	3.4
weld 1(9)	140	6.9	3.4
weld 1(10)	140	10	3.4

Table C.5 – Effect of beam voltage on μEBW of CP-titanium (Grade-3)

	Voltage (kV)	Current (mA)	Speed (m s^{-1})
weld 3(1)	14	2.5	3.4
weld 3(2)	22	2.5	3.4
weld 3(3)	52	2.5	3.4
weld 3(4)	80	2.5	3.4
weld 3(5)	88	2.5	3.4
weld 3(6)	96	2.5	3.4
weld 3(7)	106	2.5	3.4
weld 3(8)	116	2.5	3.4
weld 3(9)	128	2.5	3.4
weld 3(10)	140	2.5	3.4

Table C.6 – Effect of beam traveling speed on μEBW of AISI 1016 steel

	Voltage (kV)	Current (mA)	Speed (m s^{-1})
weld 4(1)	140	2.9	8
weld 4(2)	140	2.9	6
weld 4(3)	140	2.9	4.9
weld 4(4)	140	2.9	4
weld 4(5)	140	2.9	3.3
weld 4(6)	140	2.9	2.6
weld 4(7)	140	2.9	2
weld 4(8)	140	2.9	1.6
weld 4(9)	140	2.9	3.1
weld 4(10)	140	2.9	0.8

Table C.7 – Effect of beam current on μEBW of AISI 1016 steel

	Voltage (kV)	Current (mA)	Speed (m s^{-1})
weld 5(1)	140	0.9	3.3
weld 5(2)	140	2.0	3.3
weld 5(3)	140	2.3	3.3
weld 5(4)	140	2.6	3.3
weld 5(5)	140	2.9	3.3
weld 5(6)	140	3.4	3.3
weld 5(7)	140	3.9	3.3
weld 5(8)	140	4.5	3.3
weld 5(9)	140	6.4	3.3
weld 5(10)	140	9	3.3

Table C.8 – Effect of beam voltage on μEBW of AISI 1016 steel

	Voltage (kV)	Current (mA)	Speed (m s^{-1})
weld 6(1)	14	2.9	3.3
weld 6(2)	22	2.9	3.3
weld 6(3)	52	2.9	3.3
weld 6(4)	80	2.9	3.3
weld 6(5)	88	2.9	3.3
weld 6(6)	96	2.9	3.3
weld 6(7)	106	2.9	3.3
weld 6(8)	116	2.9	3.3
weld 6(9)	128	2.9	3.3
weld 6(10)	140	2.9	3.3

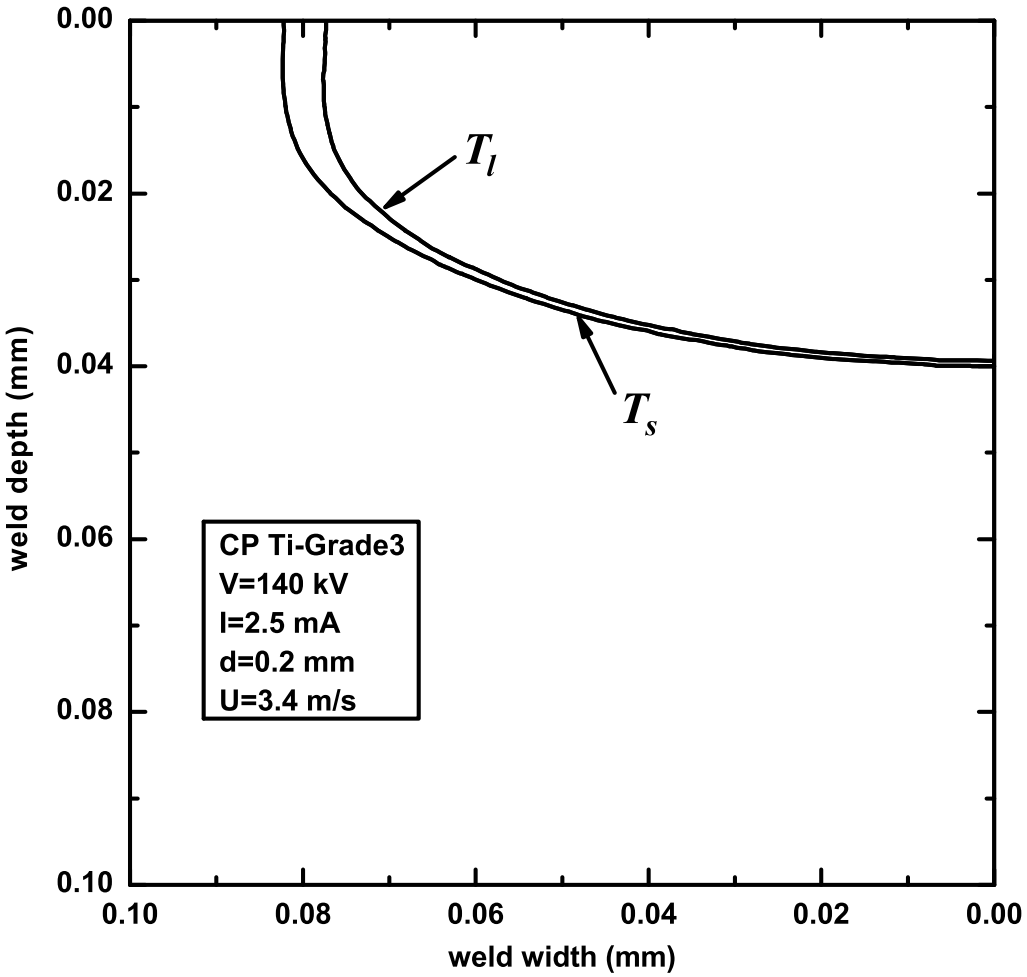

Figure C.2 – Solidus and liquidus isotherms in the CP titanium substrate representing the weld shape

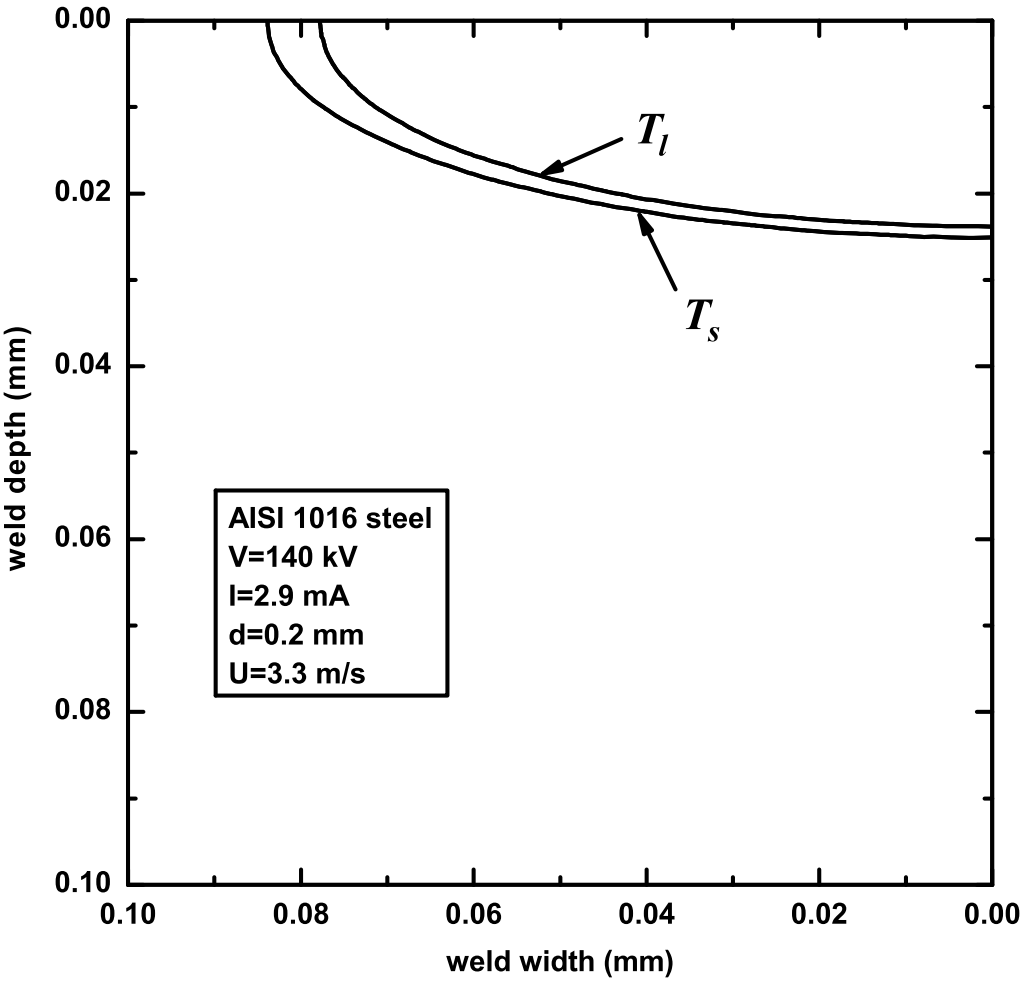

Figure C.3 – Solidus and liquidus isotherms in the AISI 1016 steel substrate representing the weld shape